DEVELOPMENT OF METAL MATRIX COMPOSITE POWDER CORED TUBULAR WIRE FOR ELECTRON BEAM FREEFORM FABRICATION

by

Devon Scott Gonzales

A thesis submitted to the Faculty and the Boards of Trustees of the Colorado School of Mines in partial fulfillment of the requirements for the degree of Masters of Science (Metallurgical and Materials Engineering).

Golden, Colorado

Date: _____

Signed: _____
Devon S. Gonzales

Signed: _____
Dr. Stephen Liu
ABS Endowed Chair Professor
Thesis Advisor

Golden, Colorado

Date: _____

Signed: _____
Dr. Ivar Reimanis
Professor and Interim Head
Department of Metallurgical and
Materials Engineering

ABSTRACT

Electron Beam Freeform Fabrication (EBF^3) is a technique, developed at NASA Langley Research Center (NASA-LaRC), which uses a computerized numerical controlled electron beam welder and a wire feed system to fabricate large scale aerospace parts. Advantages of using EBF^3 as opposed to conventional manufacturing methods include decreased deign-to-product time, decreased wasted material, and the ability to adapt controls to produce geometrically complex parts. The EBF^3 process is compatible with a range of aerospace alloys and material properties of parts produced by this process have been shown to be comparable to wrought products. However, to fully exploit the potential of the EBF^3 process, development of materials tailored for the process is required. This research used alloy theory, as well as powder cored tubular wire technology, to develop aluminum based metal matrix composite feedstock for the EBF^3 system.

Five iterations of powder cored tubular wire were made using silicon carbide particulates with different surface conditions. Uncoated particles, as well as particles with high and low amounts of copper and nickel coatings, were incorporated into the powder core. Single and multiple layer deposits were made using each wire. Beam conditions were varied for each wire to determine the optimal combination of feedstock material and electron beam parameters required to create a uniformly distributed metal matrix composite deposit using EBF^3.

Completely uniform dispersion of the reinforcement particles was not achieved in the matrix, however, it was determined that nickel additions enhanced particle dispersion as well as mitigated solidification cracking and secondary carbide formation. It was also determined that using a lower energy beam also promotes dispersion and mitigates secondary carbide formation. Computational models were created to predict phase transformations and particle dispersion in the matrix for various conditions. The thermodynamic and fluid dynamic models were able to describe trends observed through characterization of EBF^3 depositions. Results collected from characterization of the deposits as well as trends observed in the models can be used to plan future iterations of powder cored tubular wire feedstock, as well as deposition parameters, to create homogeneous metal matrix composite structures by Electron Beam Freeform Fabrication.

TABLE OF CONTENTS

ABSTRACT……..iii

LIST OF FIGURES……...vi

LIST OF TABLES……...xiii

ACKNOWLEDGMENTS…….xv

CHAPTER 1: INTRODUCTION 1

CHAPTER 2: LITERATURE REVIEW 3

2.1 Solid Freeform Fabrication Processes and Applications……...3

2.1.1 Electron Beam Freeform Fabrication (EBF^3)……..7

2.2 Alloy Systems Used in EBF^3…….8

2.2.1 Previous work on EBF^3 by the Colorado School of Mines……....9

2.3 Aluminum Alloys……..9

2.4 Aluminum Based Metal Matrix Composites……...11

2.4.1 SiC Reinforced Aluminum Alloys and Their Properties……..11

2.4.2 Potential Defects in Silicon Carbide Reinforcement of Aluminum……..12

2.5 Welding and Solidification of Aluminum Alloys……....13

2.6 Application of Fluid Mechanics to Predict Particle Dispersion in Metal Matrix Composites……..17

CHAPTER 3: EXPERIMENTAL PROCEDURE 19

3.1 Powder Cored Tubular Wire Manufacturing……...…19

3.2 Silicon Carbide Particles…….....22

3.3 Particle Characterization……..23

3.3.1 Static Laser Light Scattering…….23

3.4 Wire Characterization……..24

3.5 EBF^3 Deposition……..24

3.6 Deposit Characterization……..25

3.6.1 Microstructural Analysis……...…26

3.6.2 Compositional Analysis……26

3.6.3 Reinforcement Analysis……27

3.7 Predicting Particle Dispersion……...…28
3.7.1 Predicting Equilibrium Thermodynamics of the
Metal Matrix Composites……..29
3.7.2 Predicting Particle Dispersion Using Fluid Mechanics……33
CHAPTER 4: RESULTS AND DISCUSSION ……....36
4.1 Consumable Characterization……..36
4.1.1 Powder Characterization……...…36
4.1.2 Wire Characterization……...41
4.2 Effect of Coating Conditions on Deposit Quality……44
4.2.1 Build Characterization and Matrix microstructural Analysis……...45
4.2.2 Particle Dispersion……53
4.3 Effect of Processing Parameters on Deposit Quality……...54
4.3.1 Build Characterization and Matrix microstructural Analysis……...55
4.3.2 Particle Dispersion……57
4.4 Computational Thermodynamic Modeling…….…….60
4.4.1 Thermo-Calc Calculations……..……..61
4.4.2 HSC Calculations……..66
4.4.3 Empirical Heat Diffusivity Criterion……....72
4.5 Computational Fluid Mechanics Modeling……..72
CHAPTER 5: CONCLUSIONS……78
CHAPTER 6: RECOMMENDATIONS FOR FUTURE WORK……....…80
CHAPTER 7: REFERENCES……...…82
APPENDICES……...86

LIST OF FIGURES

Figure 1.1 Metallic airframe structural concepts; (a) conventional built-up, (b) unitized, and (c) functionally graded, curvilinear stiffened [1].....2

Figure 2.1 Schematic of the EBF^3 process in the vacuum chamber, showing the layer-additive concept as the wire is deposited[2]……..5

Figure 2.2 The constant EBF^3 coordinate system. The longitudinal direction (L) is parallel to the direction of travel; the short transverse direction (S), or direction across the width of the deposit; the long transverse direction (T) is the direction normal to the surface of the baseplate [6]……5

Figure 2.3 Examples of aluminum and titanium parts created using the EBF^3 system [2], [6]…….6

Figure 2.4 Tensile properties of EBF^3 deposited 2219, with and without pot heat treatment, as compared to typical handbook values for 2219 Al plate [7].....6

Figure 2.5 Tensile properties of EBF^3 deposited Ti-6Al-4V as compared to standard grade Ti-6Al-4V [7]……...7

Figure 2.6 Light optical photographs of the microstructure at 50X; (a) Al-10%SiC, (b) Al-20% SiC [13].....11

Figure 2.7 From top to bottom: experimental results of Al-Li [22], Al-Si [23], Al-Cu [24], Al-Mg [25], and Al-Mg_2Si [26].....14

Figure 2.8 The crack sensitivity of (Al-Cu-Mg) system [27], and (Al-Si-Mg-Cu) system [28]……....15

Figure 3.1 Photograph of the tubular mill showing the forming rolls and powder feed system..... 18

Figure 3.2 Tubular wire mill forming schematic showing the formation of the tubular wire and powder filling [5]……..….……19

Figure 3.3 Conveyor belt powder feed system for homogenous powder distribution in the wire. Uniform powder fill ratio is maintained using this method.....20

Figure 3.4 Illustration of a powder cored tubular wire showing the lap joint method for sealing the powder in [2]...……..... 20

Figure 3.5 Wire drawing schematic showing the die and lubrication station as well

as the motorized and transfer spools [5]……..21

Figure 3.6 An illustration of monochromatic light rays interacting with a particle [39]. …….23

Figure 3.7 Photograph of the EBF^3 system showing the various controlled components [2]…….24

Figure 3.8 Schematic showing the ICP-OES analysis technique, the method by which photons are emitted, and the linear relationship between photon intensity and concentration [40]……...26

Figure 3.9 Screenshot showing the method for determining volume fraction of the silicon carbide in the matrix……..27

Figure 3.10 Macrograph demonstrating the method for determining the area of each cluster and the amount of clusters in each multilayer deposit for calculating the mean free path….……..……28

Figure 3.11 Image showing the process for creating a plot using the data previously calculated……...30

Figure 3.12 The reaction equation module showing the values and units that can be varied form computing fundamental thermodynamic values of the system……...31

Figure 3.13 Image of a generated table showing the results of the equilibrium reaction at various temperatures……...31

Figure 3.14 Still images showing the calibration method for calibrating distance to pixel ratio in on the high speed video. Increments given in 0.40 mm……..33

Figure 3.15 Still image time lapse showing the position tracking of the tracer particles indicated by dots……..…34

Figure 4.1 Light optical images of A) aluminum, B) silicon, C) copper, and D) chromium powders showing morphology and relative size distribution.….36

Figure 4.2 Light optical image of uncoated silicon carbide powder, showing the morphology and relative size……37

Figure 4.3 SEM images of A) high copper content (HCC), B) low copper content (LCC), C) high nickel content (HNC), and D) low nickel content (LNC) coated silicon carbide powders. Relative size distribution and coating quality can be compared……..37

Figure 4.4 Particle size distribution histograms of A) aluminum, B) silicon, C) copper, and D) chromium powders analyzed by static laser light

scattering…….....38

Figure 4.5 Particle size distribution histogram of uncoated silicon carbide powder analyzed by static laser light scattering……..……..39

Figure 4.6 Particle size distribution histograms for A) high copper content (HCC), B) low copper content (LCC), C) high nickel content (HNC), and D) low nickel content (LNC) coated silicon carbide particles analyzed by static laser light scattering……..……....39

Figure 4.7 Logitudinal cross-sections of A) uncoated, B) high copper coated, C) low copper coated, D) high nickel coated, E) low nickel coated silicon carbide particle containing wires.……42

Figure 4.8 A) Macroscopic cross-section of uncoated SiC containing deposit using a focused rastered electron beam. B) High magnification of a silicon carbide cluster showing particle separation and aluminum carbide formation.…….….46

Figure 4.9 A) Macroscopic image of a deposit with high copper content made using a matrix showing the high amounts of intermetallic compounds as well as the presence of aluminum carbide. ……..47

Figure 4.10 A) Macroscopic image of a deposit with low copper content made using a focused rastered beam. B) High magnification image of clusters in the matrix showing the low amounts of intermetallic compounds as well as the presence of aluminum carbide……48

Figure 4.11 A) Macroscopic image of a deposit with high nickel content made using a focused rastered beam. B) High magnification image of clusters in the matrix showing the high amounts of intermetallic compounds with no presence aluminum carbide..……49

Figure 4.12 A) Macroscopic image of a deposit with low nickel content made using a focused rastered beam. B) High magnification image of clusters in the matrix showing the low amounts of intermetallic compounds with no presence aluminum carbide……..49

Figure 4.13 Comparison of coatings and the effect they have on mitigating aluminum carbide formation……...……...……..50

Figure 4.14 Comparison of average volume percent of silicon carbide retained in the matrix between different coating conditions……51

Figure 4.15 Plot comparing normalized mean free path and cluster size values for the five coating conditions. Highest favorability of dispersion in the direction of the arrow……...52

Figure 4.16 Comparison of aluminum carbide formation as a function of beam conditions for each of the deposits……...54

Figure 4.17 A comparison of average volume fraction of silicon carbide in the matrix as a function of beam conditions……...55

Figure 4.18 The effect of beam conditions on single layer deposit morphology…….57

Figure 4.19 Plot comparing normalized mean free path and cluster size values for the four beam conditions. Highest favorability of dispersion in the direction of the arrow……...58

Figure 4.20 Pseudo-binary phase diagram of the Al 6061 alloy. Composition set at Al–0.6 wt. % Si – 0.25 pct. wt. Cu with varying amounts of magnesium....60

Figure 4.21 Scheil solidification model predicting which phases form in the Al 6061/ SiC system under equilibrium cooling conditions……..61

Figure 4.22 Cu-Si-C isothermal ternary phase diagram at 2700 K.…….62

Figure 4.23 Cu-Si-C isothermal ternary phase diagram at 1350 K.…….62

Figure 4.24 Cu-Si-C isothermal ternary phase diagram at 675 K.……...63

Figure 4.25 Ni-Si-C isothermal ternary phase diagram at 2700 K.……..64

Figure 4.26 Ni-Si-C isothermal ternary phase diagram at 1350 K.……...64

Figure 4.27 Ni-Si-C isothermal ternary phase diagram at 675 K.……65

Figure 4.28 Time and temperature data of the melt pool in the GTAF^3 system measured using an infrared pyrometer.…….70

Figure 4.29 Al-Cu binary phase diagram used to predict what phases may form in localized regions as a result of using copper coated silicon carbide particles. [48], [49]……71

Figure 4.30 Al-Ni binary phase diagram used to predict what phases may form in localized regions as a result of using nickel coated silicon carbide particles. [48], [50]……71

Figure 4.31 The required velocity to promote dispersion as a function of particle radius for various liquids that may be present in the matrix in localized regions.……..72

Figure 4.32 The required velocity to promote dispersion as a function of temperature (viscosity) for various liquids that may be present in the matrix in localized regions. Vertical lines indicate the melting temperature for each liquid…...……73

Figure A.1 Axial cross-sectional backscattered electron image of a wire containing uncoated silicon carbide. The integrity of the lap joint is maintained and particles are fully packed in a uniform distribution……..86

Figure A.2 A longitudinal cross sectional backscattered electron image of a wire containing uncoated silicon carbide. EDS and contrast measurements determine the difference between silicon (light) and silicon carbide (dark) particles in the wire. Relatively uniform distribution of silicon carbide particles in the wire is shown. Voids are not present in the core of the wire…….87

Figure A.3 A longitudinal cross sectional backscattered electron image of a wire containing silicon carbide with a high copper content. High copper content particles agglomerate towards the center of the wire in a straight line. The copper coating was determined to maintain uniform coverage on the silicon carbide particle……...88

Figure A.4 Axial cross-sectional backscattered electron image of a wire containing silicon carbide with a low copper content. The integrity of the lap joint is compromised to due powder entrapment. This leads to unravelling of the sheath during deposition, which creates less desirable deposits. Uniform distribution of silicon carbide in the core was observed……....89

Figure A.5 A longitudinal cross sectional backscattered electron image of a wire containing silicon carbide with a copper content. There is incomplete coverage of copper coating on the silicon carbide. The particles show a much more uniform distribution high copper content particles……90

Figure A.6 A longitudinal cross sectional backscattered electron image of a wire containing silicon carbide with a high nickel content. Complete coverage of the coating was observed. Insufficient volume fraction can be observed compared to that of other wires……91

Figure A.7 Axial cross-sectional backscattered electron image of a wire containing silicon carbide with a high nickel content. The lap joint is completely sealed near the powder, protecting it from loss or contamination, however it maintains a gap which could lead to unravelling during deposition……..92

Figure A.8 A longitudinal cross sectional backscattered electron image of a wire containing silicon carbide with a low nickel content. Incomplete coverage of the coating was observed. Uniform distribution of the powder was maintained in the longitudinal direction……...93

Figure A.9 Axial cross-sectional backscattered electron image of a wire containing silicon carbide with a low nickel content. The lap joint is not completely

sealed which could lead to unravelling during deposition. The particles are evenly distributed in the powder core…….94

Figure B.1 A) Macroscopic cross-section of a multiple layer deposit containing uncoated silicon carbide using a focused rastered electron beam with a (0.25f) frequency pulse. B) High magnification of a silicon carbide cluster showing particle separation and aluminum carbide formation…..…95

Figure B.2 A) Macroscopic image of a deposit with high copper content made using a focused rastered beam with a (0.25f) frequency pulse. B) High magnification image of a cluster in the matrix showing the high amounts of intermetallic as well as the presence of aluminum carbide……..…95

Figure B.3 A) Macroscopic image of a deposit with low copper content made using a focused rastered beam with a (0.25f) frequency pulse. B) High magnification image of clusters in the matrix showing the low amounts of intermetallic as well as the presence of aluminum carbide…….….96

Figure B.4 A) Macroscopic image of a deposit with high nickel content made using a focused rastered beam with a (0.25f) frequency pulse. B) High magnification image of clusters in the matrix showing the high amounts of intermetallic with no presence aluminum carbide……96

Figure B.5 A) Macroscopic image of a deposit with low nickel content made using a focused rastered beam with a (0.25f) frequency pulse. B) High magnification image of clusters in the matrix showing the low amounts of intermetallic with no presence aluminum carbide……97

Figure B.6 A) Macroscopic cross-section of a multiple layer deposit containing uncoated silicon carbide using a focused rastered electron beam with a (f) frequency pulse. B) High magnification of a silicon carbide cluster showing particle separation and aluminum carbide formation…….97

Figure B.7 A) Macroscopic image of a deposit with high copper content made using a focused rastered beam with a (f) frequency pulse. B) High magnification image of a cluster in the matrix showing the high amounts of intermetallic as well as the presence of aluminum carbide……...98

Figure B.8 A) Macroscopic image of a deposit with low copper content made using a focused rastered beam with a (f) frequency pulse. B) High magnification image of clusters in the matrix showing the low amounts of intermetallic as well as the presence of aluminum carbide……...98

Figure B.9 A) Macroscopic image of a deposit with high nickel content made using a focused rastered beam with a (f) frequency pulse. B) High

magnification image of clusters in the matrix showing the high amounts of intermetallic with no presence aluminum carbide……...99

Figure B.10 A) Macroscopic image of a deposit with low nickel content made using a focused rastered beam with a (f) frequency pulse. B) High magnification image of clusters in the matrix showing the low amounts of intermetallic with no presence aluminum carbide…….99

Figure B.11 A) Macroscopic cross-section of a multiple layer deposit containing uncoated silicon carbide using a defocused electron beam. B) High magnification of a silicon carbide cluster showing particle separation and aluminum carbide formation…….….100

Figure B.12 A) Macroscopic image of a deposit with high copper content made using a defocused beam. B) High magnification image of a cluster in the matrix showing the high amounts of intermetallic as well as the presence of aluminum carbide……100

Figure B.13 A) Macroscopic image of a deposit with low copper content made using a defocused beam. B) High magnification image of clusters in the matrix showing the low amounts of intermetallic as well as the presence of aluminum carbide……..…..101

Figure B.14 A) Macroscopic image of a deposit with high nickel content made using a defocused beam. B) High magnification image of clusters in the matrix showing the high amounts of intermetallic with no presence aluminum carbide…….101

Figure B.15 A) Macroscopic image of a deposit with low nickel content made using a defocused beam. B) High magnification image of clusters in the matrix showing the low amounts of intermetallic with no presence aluminum carbide…….102

Figure D.1: Pseudo-binary phase diagram of the Al 6061 alloy. Composition set at Al – 1.0 wt. pct. Mg – 0.25 pct. wt. Cu with varying amounts of silicon...105

Figure D.2 Al-Cu-Si isothermal ternary phase diagram at 675 K…….106

Figure D.3 Al-Ni-C isothermal ternary phase diagram at 1350 K……....107
.
Figure D.4 Al-Ni-C isothermal ternary phase diagram at 675 K…….108

LIST OF TABLES

Table 2.1 Designation of aluminum alloys [5] 9

Table 2.2 Composition (ranges) of 2219 and 6061 aluminum alloy alloys [8]……. 9

Table 4.1 Comparison of analytical methods to material specifications. 40

Table 4.2 Comparison of composition for each of five iterations of metal matrix composite powder cored tubular wires. 40

Table 4.3 Comparison of volume fraction measurements in the five iterations of wire. 42

Table 4.4 Compositional analysis of metal matrix composite depositions……...44

Table 4.5 Comparison of macroscopic images for each of the various material and beam conditions. 45

Table 4.6 Comparison of single layer deposit cross-sections. 56

Table 4.7 Equilibrium reaction between aluminum and silicon carbide over 100°C increments. 66

Table 4.8 Equilibrium reaction between aluminum and silicon carbide over 100°C increments in the presence of a copper coating. 67

Table 4.9 Equilibrium reaction between aluminum and dissolved silicon carbide over 100°C increments in the presence of a copper coating.....68

Table 4.10 Empirical heat diffusivity criterion values calculated for various possible particle/liquid interactions. 69

Table B.1 Multiple layer build comparison of different measurements taken for each coating and beam condition. Defocused pulsed beam condition trials included……..103

Table C.1 Single layer build comparison of different measurements taken for each coating and beam condition. Defocused pulsed beam condition trials included……...…104

Table E.1 Equilibrium reaction data for the Al-Mg-SiC system predicting the favorability of maintaining silicon carbide stability in the presence of magnesium……..109

Table E.2 Equilibrium reaction data for the Al-Mg-SiC system predicting the favorability of stabilizing aluminum carbide formation in the presence of magnesium. It is more favorable than maintaining silicon carbide……110

Table E.3 Equilibrium reaction data for the Al-Mg-Cu-SiC system predicting the favorability of maintaining silicon carbide stability……....111

Table F.1 Temperatures of the melt pool measured by the infrared pyrometer…..…112
.
Table F.2 Viscosity and steady state velocity data for various compositions and temperatures seen in the melt pool……..113

ACKNOWLEDGEMENTS

I would like to thank Marcia Domack and Robert Hafley from NASA Langley Research Center for their continuous support and funding of this research. Their advice and direction during the work were important in helping me grow as a researcher and a student. I would also like to thank them for allowing me to visit NASA-LaRC and work directly with the EBF^3 group. The visits were invaluable experiences in helping me complete my work as well as solidifying my dream of one day working with NASA. The many people in the Advanced Materials and Processing Branch at NASA- LaRC were great to work with and learn from. Next, I would like to thank Dr. Liu, my advisor and mentor, for believing in me and allowing me the opportunities I needed to succeed. He has helped to build me into the researcher and engineer I am today, without him I would not have made it to this point in my career. I would like to thank my committee members, Dr. Gerald Bourne and Dr. Zhenzhen Yu, for their advice given and for participating in my thesis defense. I would also like to acknowledge my friends, officemates, and colleagues in the department who helped me with my experiments. Namely, I would like to thank Stephen Tate and Erik Pfeif for their mentoring as senior graduate students and assistance in developing experimental setups. Lastly, I would like to thank all of my friends, family, and girlfriend for their belief and support. Without them I wouldn’t be who I am today.

CHAPTER 1: INTRODUCTION

Solid freeform fabrication is becoming a highly favorable technology in the additive manufacturing industry. The ability to incorporate material as required allows for the production of highly intricate parts with little excess material, making it particularly efficient when manufacturing complex, expensive parts. In addition to manufacturing, solid freeform fabrication processes can be used to extend the service life of damaged parts by repairing locally rather than replacing entire parts. Many solid freeform fabrication techniques have been developed to create large scale parts for use in aeronautics and aerospace applications. NASA's Electron Beam Freeform Fabrication (EBF^3) system uses a computerized numerical controlled (CNC) electron beam welder with a manipulating stage and a multiple wire feed system to create large scale parts. The ability to use multiple wire feedstocks of different compositions is a major advantage of the EBF^3 system enabling the ability to introduce different materials to achieve the best performance in critical sections of a large part.

Currently, there is a push in the commercial aircraft industry to reduce fuel consumption with new aircraft designs. One way to reduce fuel consumption is to reduce the overall weight of the aircraft which can be accomplished through the use of improved materials and more efficient designs. Typical aircraft fuselage structure is multi-piece construction with spars and ribs riveted to thin sheet (Figure 1.1a). Typically, fuselage skins are 2XXX series aluminum alloys for high toughness and spars and ribs are 7xxx series aluminum for high strength. Unitized structural concepts (Figure 1.1b) eliminate fasteners which reduce manufacturing costs and time. However, machined unitized structures are fabricated from a single material, making it impossible to fulfill the toughness and strength requirements of conventional airframe fuselage structure. Advanced manufacturing methods such as EBF^3 are being implemented to enable single-piece fabrication by depositing stiffeners directly onto the fuselage skin, eliminating the fasters and reducing manufacturing costs. EBF^3 enables advanced design concepts, illustrated in Figure 1.1, that combine novel stiffeners following the load paths with graded material composition to locally tailor properties. These concepts offer the potential for improved structural performance which translates to reduced structural weight. The alloys used in conventional airframe structures are generally not amenable to joining by fusion methods, consequently alternative materials are needed to realize the potential of advanced concepts

produced by EBF^3. Powder core wire technology has been investigated as a method to produce custom chemical composition feedstock for the EBF^3 process and has demonstrated success with aluminum and titanium alloys [1], [2]. Powder cored tubular wire technology, can be used to adjust alloy composition and produce specialty materials which, combined with process parameter adjustments, produces deposited material with properties tailored for specific service requirements.

The major objective of this research was to develop and manufacture metal matrix composite powder cored tubular wires to have a target as-solidified composition of 6061/SiC/10p when deposited using EBF^3. Kinetic and thermodynamic models were created to predict the behavior during solidification. Custom alloyed wires were manufactured with coated reinforcement particles in the powder core to create a composite structure using EBF^3.

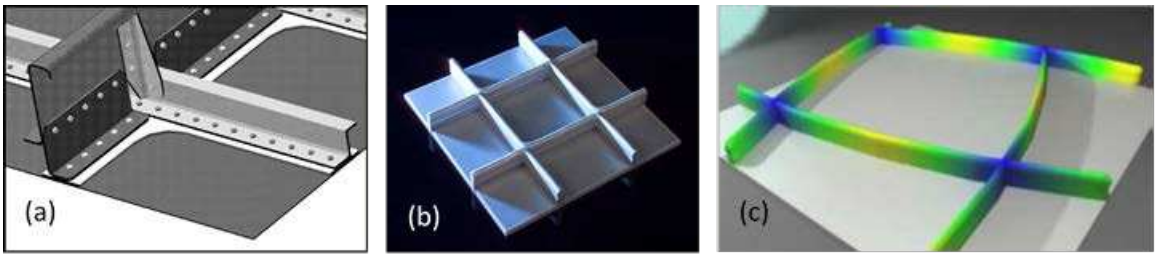

Figure 1.1 Metallic airframe structural concepts; (a) conventional built-up, (b) unitized, and (c) functionally graded, curvilinear stiffened [1].

CHAPTER 2: LITERATURE REVIEW

This chapter gives a comprehensive literature review which was used to develop the research and experimental procedures of the project.

2.1 Solid Freeform Fabrication Processes and Applications

Additive manufacturing is a process of producing solid objects, or parts, through a buildup of material to create a product rather than machining or multi-piece assembly. This technique uses joining process, such as sintering, melting, or welding to deposit material onto a base until the desired three-dimensional shape is achieved. Solid Freeform Fabrication (SFF) is a layer-additive manufacturing process that produces near-net shape parts by depositing feedstock such as wire, powder, or sheet, on a substrate in layers of finite thicknesses, as per a computer aided design (CAD) model [2], [3].

Solid Freeform Fabrication was originally developed for nonmetallic materials, specifically polymer-based feedstocks to fabricate models and patterns for molds used in casting. These are typically made by stereolithography or selective laser sintering (SLS) processes, commonly known as 3-D printing. SFF technology has since been expanded to incorporate metallic systems. Processes such as Electron Beam Freeform Fabrication (EBF^3), Direct Metal Deposition (DMD), and Laser Engineered Net Shaping ($LENS^{TM}$) have all been developed to incorporate metal systems. These processes can be utilized to create near-net shaped parts, or for repair or detailing of previously manufactured parts [2], [4].

The potential advantages gained by SFF technologies are desired in many emerging technologies. Many SFF processes require less energy, optimize material usage and design-to-production time, while often enhancing material properties. The benefits can equate to a difference in costs for industries such as aerospace or medical instrumentation, where specialty and often expensive materials are used. Casting requires fixtures and molds to form a final part. Often, the surface finishes and tolerances are not to specification so subsequent machining is required. Forgings require dies and heavy machinery to form the desired shape; excess machining is often required to finish the part. The amount of energy to melt large amounts of metal for casting, or to heat and forge a part is significantly higher than SFF processes. Conventional machining of parts requires fixturing and tooling to cut away unwanted material. These operations also require high tolerances in many applications. SFF technologies generally

requires less machining to create the final product than conventional manufacturing processes, which results in less wasted material and shortened lead time. The buy-to-fly ratio (ratio of purchased raw materials to the amount of material in the final part) for traditional manufacturing methods can be as high as 14:1 to 20:1, where as little as five percent of the initial material is used in the final part. SFF technologies can have a buy-to-fly ratio of 2:1 where up to half of the original material is retained in the final part. SFF technologies also offer improved microstructural and mechanical properties as compared to those of large parts produced by traditional methods. Localized heating and cooling of layers in SFF leads to refined microstructures and mitigates compositional segregation observed in many large cast parts where cooling rates differ between the middle of the part to the surface [2], [5].

2.1.1 Electron Beam Freeform Fabrication (EBF^3)

Electron Beam Freeform Fabrication (EBF^3) is an emerging SFF technology under development at the NASA Langley Research Center. The EBF^3 process uses a focused electron beam in a high vacuum environment to create a localized molten pool on a base plate. Wire feedstock is introduced into the pool and deposited in a layer by layer fashion as shown in Figure 2.1. The relationship between the wire, beam and travel direction can be varied to support deposition of complex shapes. A typical wall-shaped build is shown in Figure 2.2. The electron beam system is approximately 100% efficient in wire consumption and 95% efficient in power usage. EBF^3 is capable of a wide range of deposition rates (up to 14 kg/hr.) and part details depending on the process parameters and size of wire used [2]. The EBF^3 system has a six axis positioning system to make a wide range of near-net shaped parts, such as an aerodynamic model (a), an airfoil (c), or an rocket nozzle vent (f), shown in Figure 2.3 [6]. Dual wire feed capability enables grading material composition throughout the parts.

2.2 Alloy Systems Used in EBF^3

The EBF^3 technology was developed primarily for aerospace applications as a way to make parts and repairs in both terrestrial and space environments. The materials compatible with the EBF^3 process for these applications include aluminum alloys, titanium alloys, nickel based super alloys, and stainless steels. Other aluminum alloys being explored include aluminum matrix composites. Tensile properties of commercial Al 2219 and Ti-6Al-4V alloys to those of deposits made using the EBF^3 system that have been gathered to confirm that the EBF^3 process is

comparable to commercial production methods. Figures 2.4 and 2.5 show that the EBF^3 deposits exhibit comparable tensile properties to those of wrought and cast products of the same material [7].

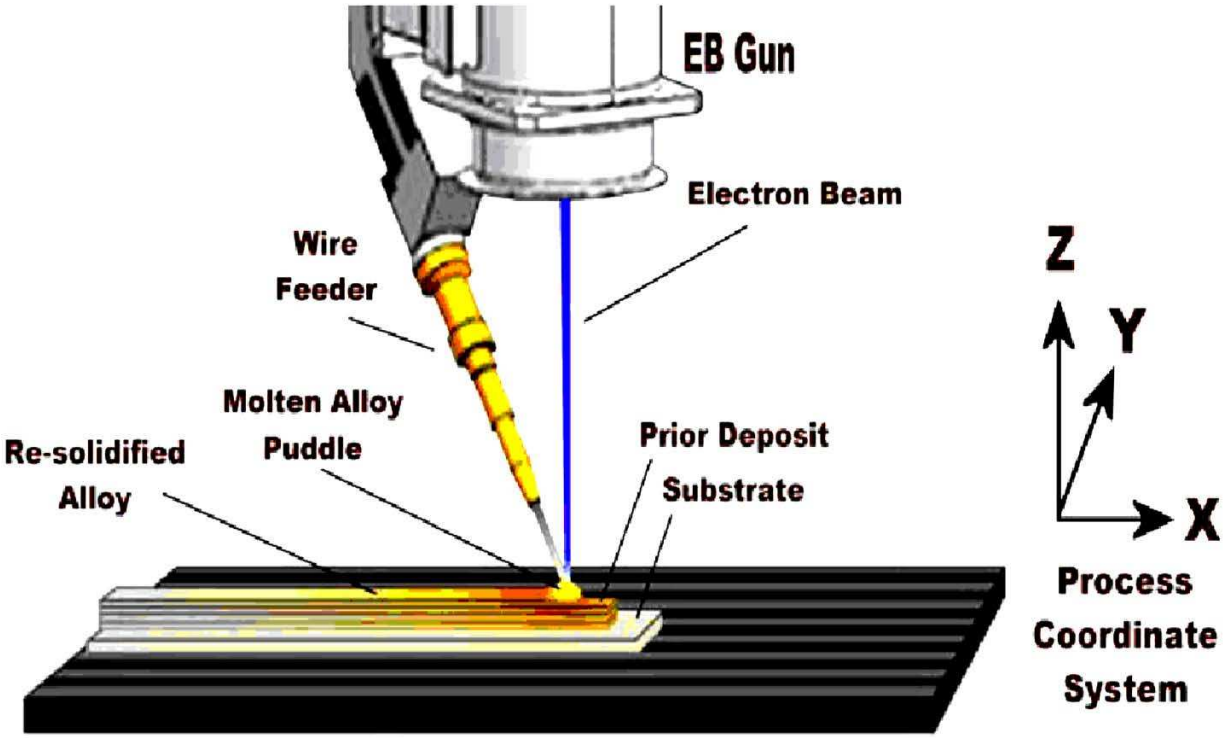

Figure 2.1 Schematic of the EBF^3 process in the vacuum chamber, showing the layer-additive concept as the wire is deposited [2].

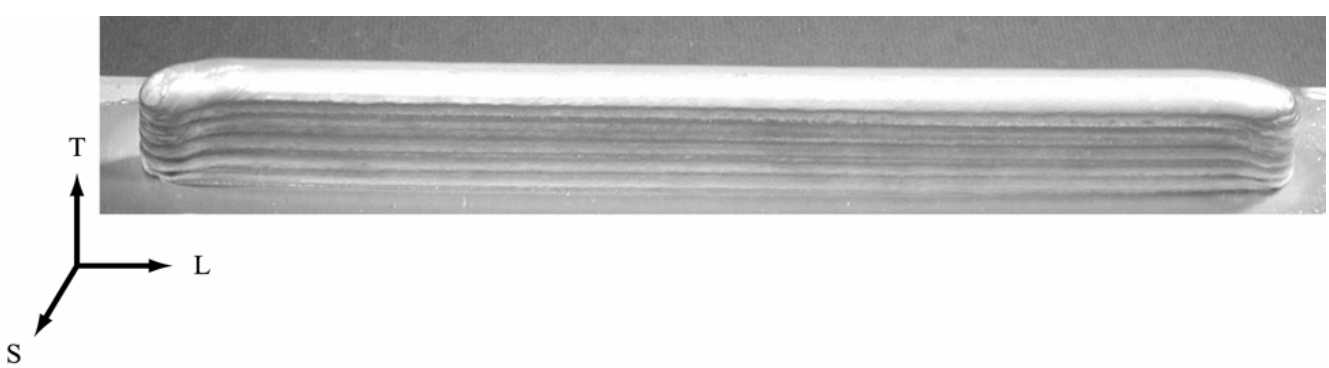

Figure 2.2 The constant EBF^3 coordinate system. The longitudinal direction (L) is parallel to the direction of travel; the short transverse direction (S), or direction across the width of the deposit; the long transverse direction (T) is the direction normal to the surface of the baseplate [6].

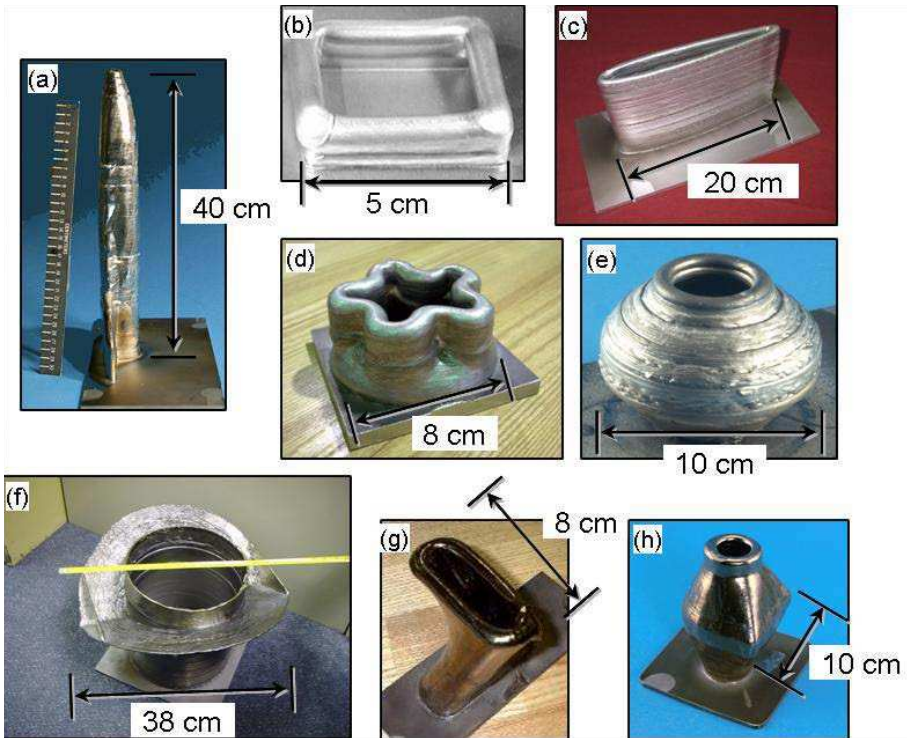

Figure 2.3 Examples of aluminum and titanium parts created using the EBF^3 system [2], [6].

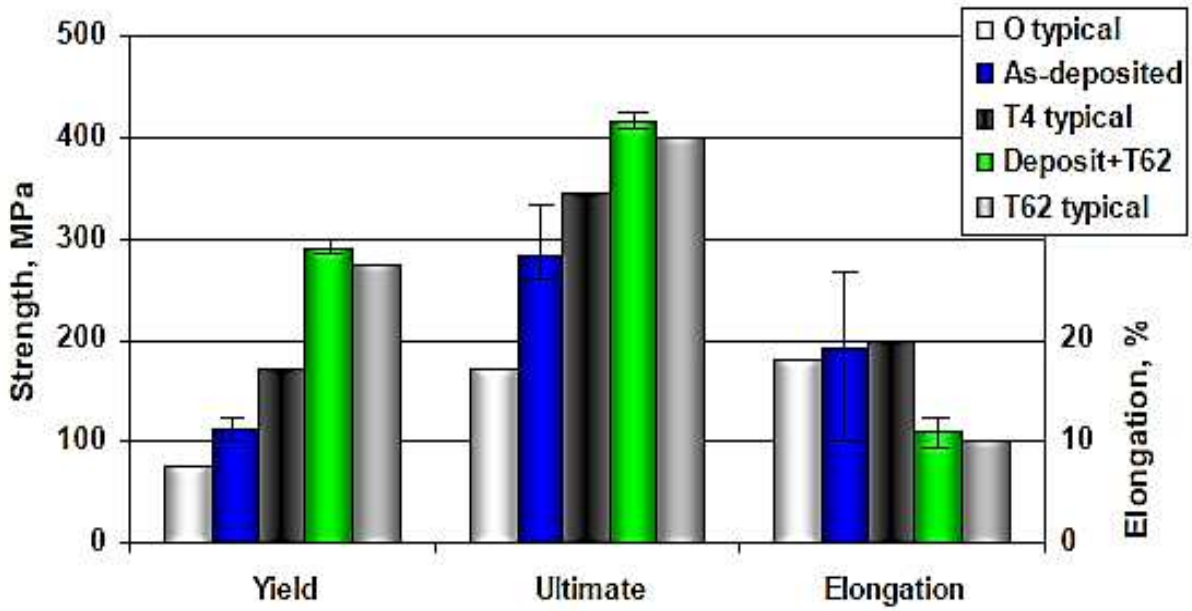

Figure 2.4 Tensile properties of EBF^3 deposited 2219, with and without heat treatment, as compared to typical handbook values for 2219 Al plate [7].

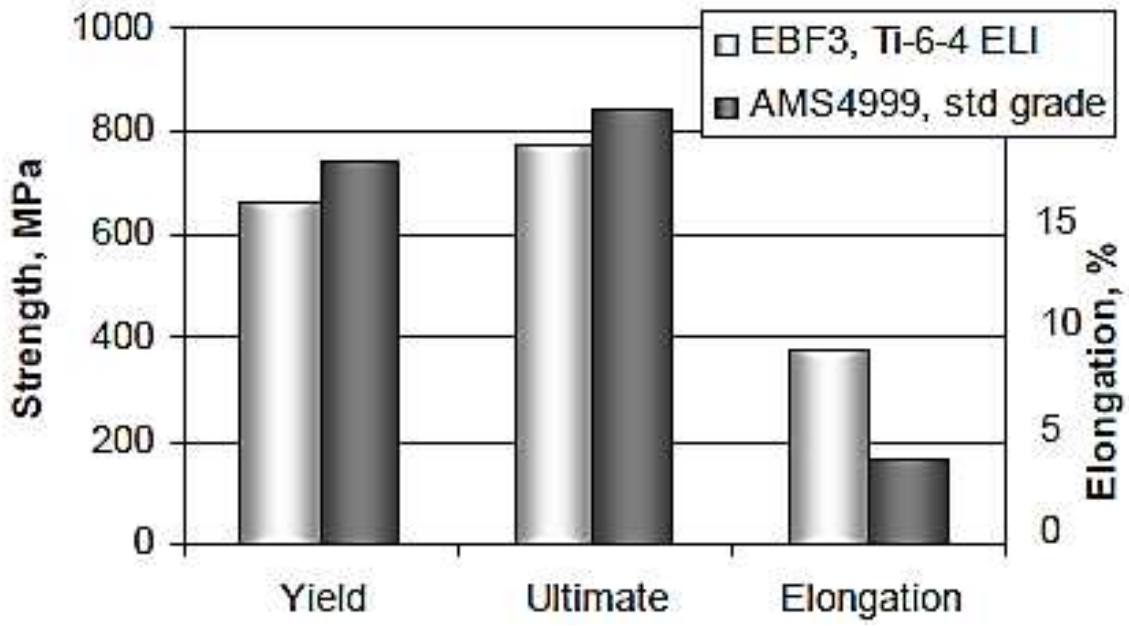

Figure 2.5 Tensile properties of EBF^3 deposited Ti-6Al-4V as compared to standard grade Ti-6Al-4V [7].

2.2.1 Previous work on EBF^3 by the Colorado School of Mines

Typically, monolithic wires of the final as-deposited composition are used in the EBF^3 system. Due to the high energy density of the electron beam and the vacuum environment in which the deposition is conducted, vaporization of alloying elements from the molten pool is common for the EBF^3 process. As such, the final component is often depleted in alloy additions with high vapor pressure, making the final part out of compositional specification. Custom alloyed powder cored wires have been developed with alloy enhancements to mitigate alloy losses during deposition, however, the production of these wires can result in higher cost. [2]. C. Hillier developed powder cored tubular wires consisting of a pre-alloyed metallic sheath filled with powder additions for mitigating vaporization losses as an economical alternative. Titanium-based powder cored tubular wires were developed to mitigate aluminum vaporization loss during the deposition of Ti-6Al–4V. Aluminum-based powder cored tubular wires were developed to mitigate magnesium vaporization loss during Al 6061 alloy deposition. EBF^3 deposits of both wires resulted in comparable composition and deposit characteristics to deposits made with solid wires with the exception of porosity. The high amounts of porosity in the deposits made using powder cored wires was attributed to entrapment of lubricant (hydrogen contamination) during

wire processing. With modifications to processing conditions the powder cored tubular wires were shown to be a viable alternative to solid wires [2].

Parts made using EBF^3 can meet specifications originally written for conventional processing techniques. However, some alloys are prone to coarse-grained microstructures and anisotropy due to epitaxial growth in the deposition direction. In the Ti-6Al-4V alloy, β grains grow epitaxially, creating crystallographic textures in the structure. Beam modulation was used in the EBF^3 system to dynamically control the weld pool and decrease the overall β grain size in the deposit [5]. A modified Ti-6Al-4V powder cored wire feedstock was developed as an alternative method for β grain refinement and epitaxial growth interruption. The powder core consisted of iron and boron additions. The resulting microstructures resulted in β grain refinement and an increase in β phase due the iron additions. The addition of boron resulted in boride precipitation in the β matrix which acted as pinning points for further grain refinement and epitaxy interruption. Both methods proved to be effective in controlling the microstructure during deposition and in improving mechanical properties of EBF^3 deposits [5].

2.3 Aluminum Alloys

Aluminum alloys are highly sought after in the aerospace field due to their high strength-to-weight ratio and cost effectiveness. Through the addition of alloying elements, different properties can be achieved and tailored to fit specific applications. Properties desired for aluminum alloys include strength, toughness, ductility, stiffness, corrosion and wear resistance. Aluminum alloys are divided into two categories: wrought alloys and cast alloys. These categories are designated by an XXXX or XXX.X number sequence, respectively. The first number designates the main alloying element(s) present in the aluminum as shown in Table 2.1 [8]. The aerospace industry mainly uses heat treatable wrought alloys, 2XXX, 6XXX, 7XXX, and 8XXX, and primarily A357.0 and A201.0 for cast alloys. Heat treatable wrought alloys are used for their ability to refine grain structure and control properties such as strength and toughness. Cast alloys A201.0 and A357.0 are used because they produce ingots with tensile properties of up to 350 MPa and 420 MPa, respectively [9].

The EBF^3 process has used 2XXX series aluminum alloys for deposition, specifically 2219. Al 2219 alloy is a 6 wt. % copper alloy commonly used in the aerospace industry for its excellent weldability and good strength and toughness over a broad range of temperatures; ultimate tensile strength values for Al 2219-T6 alloy is on the order of 400 MPa [9]. Al 7XXX

Table 2.1: Designation of aluminum alloys [8].

Wrought		Cast	
Alloying element(s)	Aluminum Association Number Designation	Alloying element(s)	Aluminum Association Number Designation
Aluminum, ≥ 99.00%	1XXX	Aluminum, ≥ 99.00%	1XX.X
Copper	2XXX	Copper	2XX.X
Manganese	3XXX	Silicon- (Cu and/or Mg)	3XX.X
Silicon	4XXX	Silicon	4XX.X
Magnesium	5XXX	Magnesium	5XX.X
Magnesium-Silicon	6XXX	Zinc	7XX.X
Zinc	7XXX	Tin	8XX.X
Other (Li, B, Zr)	8XXX	Other	9XX.X

series alloys are used in areas where even higher strength is required; for example, Al 7075 alloy has an ultimate tensile strength of approximately 570 MPa. Al 6061 alloy, the most commonly used alloy across multiple industries, including the aerospace field, has a tensile strength of approximately 300 MPa. The aluminum alloys of interest for use in the EBF^3 system are the 2219 and 6061 alloys. Al 2219 alloy is considered a highly weldable alloy whereas Al 6061 alloy requires filler material to reduce crack susceptibility which is attributed to the differences in compositions of the alloys, shown in Table 2.2 [8].

2.4 Aluminum Based Metal Matrix Composites

Metal matrix composites (MMC) were developed using lightweight materials such as, aluminum and titanium, with a wide variety of continuous and discontinuous reinforcements to increase such properties as strength, stiffness, impact resistance, and wear resistance while maintaining a low density [10]. The composite reinforcements are generally divided into three categories: continuous fibers, discontinuous fibers (whiskers), and particulates. Particle-reinforced MMCs have become the most commonly used due to the competitive costs of

Table 2.2: Composition (ranges) of Al 2219 and Al 6061 alloys [8].

AA Alloy Designation	Composition (% wt.)										
Element	Si	Fe	Cu	Mn	Mg	Cr	Zn	V	Ti	Other	Al
2219	0.20	0.30	5.8-6.8	0.20-0.40	0.02	-	0.10	0.05-0.15	0.02-0.10	0.25-0.40	Bal.
6061	0.40-0.80	0.70	0.15-0.40	0.15	0.80-1.2	0.04-0.35	0.25	-	0.15	0.15	Bal.

processing, the relative ease to manufacture these composites, and the improvement of isotropic distribution compared to that of fibers and whiskers. The properties of particle (dispersion) reinforced MMCs depend on the diameter of the particles, the inter-particle spacing, the volume fraction of the reinforcement, and the matrix-reinforcement interface. The work hardening coefficient and other matrix properties can also contribute to the properties of the MMC [10].

Aluminum-based metal matrix composites are generally composed of an aluminum alloy matrix with either a fiber or particulate reinforcement. The nomenclature for aluminum metal matrix composites is given by ANSI 35.5-1992 standard [11]. For example, 6061/SiC/10p-T6 consists of Al 6061 alloy matrix, with 10 vol. pct. of silicon carbide reinforcement in particulate form, and heat treated to a T6 condition [11]. The 2xxx and 6xxx series aluminum alloys are the most commonly used base alloys in Al-MMCs. Examples of particulate reinforcements used in aluminum-based composites are oxides (Al_2O_3), carbides (SiC), silicides (VSi_2), borides (TiB_2) and refractory metals (Cr, W) [12].

Particulate reinforced aluminum metal matrix composites are currently produced commercially for industrial use. One method of production is by powder metallurgy. The aluminum alloy used as the matrix is produced and processed to powder form. The composite particulates are then blended with the aluminum alloy powder to a uniform distribution. The blended powder is sintered then pressed into the final geometry. Alternatively, casting methods

are used to produce aluminum MMCs on a large scale. The aluminum alloy is melted and is held at a super-heated temperature to achieve a high viscosity. The reinforcement particulates are then introduced while the melt is stirred to stimulate uniform dispersion in the melt. Some composites require a metal or oxide coating on the reinforcement particles to further promote dispersion and increase the interfacial bond strength between the particles and matrix.

2.4.1 SiC Reinforced Aluminum Alloys and Their Properties

Silicon carbide reinforced aluminum is becoming more widely explored as an alternative material where properties such as low density, high strength and good wear resistance are required. Typically, Al/SiC MMCs have been created using 2XXX and 6XXX series wrought alloys or 3XX.X series cast alloys as the matrix. Researchers generally work with volume fractions of particulate SiC reinforcement between 10-20% [13]. Average particulate sizes range from approximately 7 - 100 μm as reported in the literature [13]. The effects of 50 μm SiC were studied on the properties of pure aluminum. Samples containing 5, 10, 15 and 20 vol. % SiC exhibited increasing ultimate tensile strength from approximately 80 MPa to 180 MPa with increasing volume fraction of the silicon carbide particulates [13]. Hardness also increased while impact toughness decreased. It was also found that failure occurred as de-cohesion of the reinforcement followed by ductile failure of the matrix. Increased volume fraction of the particulates reduced grain size of the matrix. Examples of uniformly dispersed aluminum based MMCs are shown in Figure 2.6.

Using the powder sintering process, aluminum powder was pressed and sintered with 0 to 30 wt. % SiC particles in 5 wt. % increments. The materials were sintered at temperatures ranging from 650ºC to 900ºC in 50ºC increments. The parts were tested under compression. It was found that strength increased from 300 MPa for the 5 wt. % SiC samples to 350 MPa for the 15 wt. % SiC samples, then decreased (with increasing volume fraction) to 200 MPa for the 30 wt. % SiC samples. This drop in strength is caused by clustering of the silicon carbide particles which creates voids and crack initiation points. Samples containing more than 15 wt. % SiC particles exhibited brittle failure during testing and incomplete bonding was observed in the microstructure [14]. The effects of reinforcement size and coating were studied on samples of pressed and sintered Al 6061 alloy with 10 wt. % silicon carbide particles. Samples contained

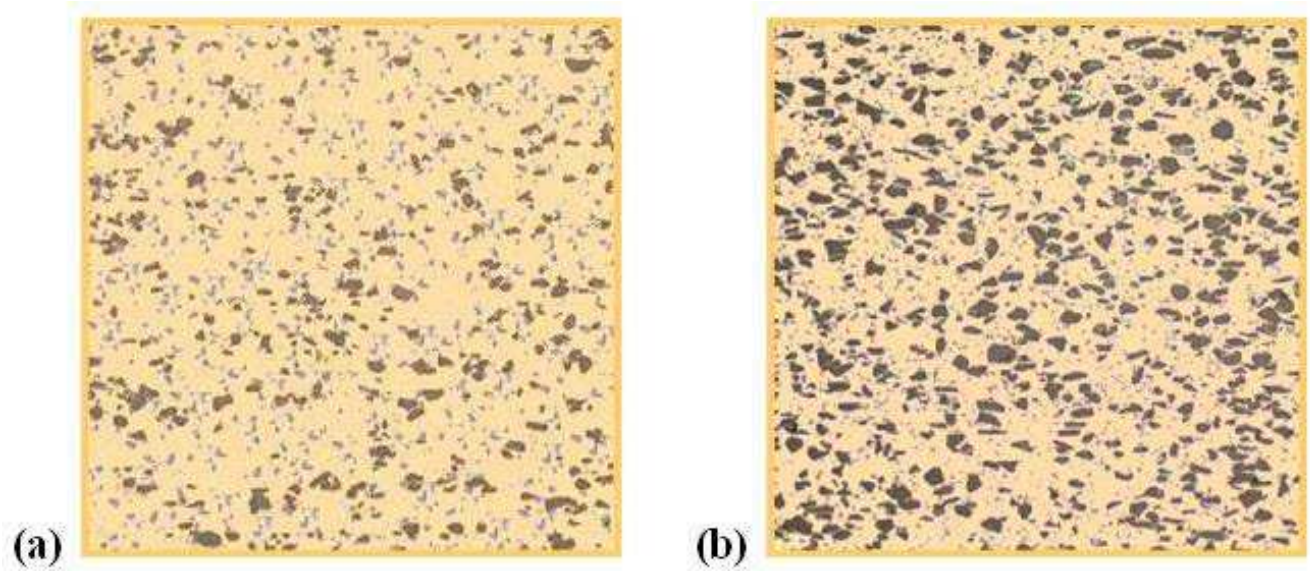

Figure 2.6 Light optical photographs of the microstructure at 50X; (a) Al-10%SiC, (b) Al-20% SiC [13].

uncoated and copper coated silicon carbide with a particle size of 7 or 23 µm. Results of the tensile tested samples showed that the copper coating increased the strain to failure and slightly increased the tensile strength. However, it was shown that the smaller particle size increased the strength by 60 MPa [15].

2.4.2 Potential Defects in Silicon Carbide Reinforcement of Aluminum

Aluminum based MMCs can contain between 1 and 60% volume fraction of reinforcement although most research on the subject has been conducted on Al/SiC MMCs with a volume fraction between 10 and 30% [12]. A major problem of processing Al/SiC MMCs is, as with most other composites, the poor wettability of the composite to the matrix. This poor wetting enhances the tendency for the SiC particles to agglomerate [13]. Increased volume fraction also adversely affects the wettability of SiC to the aluminum matrix [16]. Due to the reactivity between the reinforcement particle and the matrix, SiC or graphite based reinforcements can form aluminum carbide (Al_4C_3) by one of the two possible reactions:

$$3SiC(S) + 4Al(L) = Al_4C_3(S) + 3Si \quad (2.1)$$

$$3C(S) + 4Al(L) = Al_4C_3(S) \quad (2.2)$$

near the interface of the reinforcement and the matrix [17], [18]. These reactions tend to occur at temperatures above 650ºC [19]. Aluminum carbide at the Al-SiC interface is susceptible to

corrosion in aqueous environments, resulting in porosity and crack nucleation sites that will cause a decrease in mechanical properties [17]. The presence of aluminum oxide forms a boundary layer which leads to non-wetting of carbides by the aluminum. The particle size of the reinforcement can also affect the wettability by the matrix. Smaller particles exhibit larger surface areas requiring higher surface energy for the matrix to conform to the particles. Smaller particles also agglomerate readily due to their high surface area [20].

Copper, magnesium, silicon, titanium and nickel have been known to enhance the wettability of the SiC in the matrix. Copper and magnesium can form spinels in the presence of aluminum oxide by the reaction:

$$3Mg(Cu) + 4Al_2O_3 = \square 3Mg(Cu)Al_2O_4 + 2Al \quad (2.3)$$

The formation of these spinels can enhance the wettability of the reinforcement, mitigating the amount of agglomeration of the particles [17]. Copper can also form a fluid Al-Cu eutectic liquid that can fill pores and voids. An infiltration kinetics study was conducted to determine the effect of nickel coating on the wettability of silicon carbide in the matrix. Initial results showed that nickel coating prevented the formation of aluminum carbide in the aluminum matrix and enhanced interfacial bonding between the reinforcement and the matrix [21]

Methods such as coating the SiC particles, or the incorporation of a filler material with higher amounts of coating elements have been explored to increase the wettability and coherency of the SiC in the matrix [17]. Filler aluminum alloys used in welding of Al 6061 alloy can be implemented in the melting or joining of Al 6061 alloy-based MMCs. The high magnesium content of Al 5356 alloy increases the wetting of the reinforcement, particularly with Al_2O_3, whereas the higher silicon content in Al 4043 alloy will suppress the formation of Al_4C_3 by stabilizing the silicon carbide. Problems may arise if the silicon content becomes too large due to coarsening of the silicon phase during solution heat treatments [17].

2.5 Welding and Solidification of Aluminum Alloys

Traditional methods for welding aluminum are gas tungsten arc welding (GTAW) and gas metal arc welding (GMAW), with gas tungsten arc welding in alternate current (AC) mode the preferred process. High energy density welding processes such as electron beam welding and laser welding are also prominent for welding aluminum alloys. This section will focus on gas

tungsten arc and electron beam welding. Aluminum rapidly forms an oxide layer in the presence of any amount of oxygen. This oxide is insoluble in the aluminum metal and inhibits wetting and penetration by deposits of filler metal, therefore, the oxide layer must be broken to allow for substantial fusion and wetting. High heat inputs are required for melting or welding of aluminum due to its high thermal and electrical conductivities. Because aluminum is non-magnetic, the welding arc or electron beam is not interfered as in welding of ferrous alloys [22].

Heat-treatable aluminum alloys are most commonly used in the aerospace industry (2XXX, 6XXX, 7XXX). This section will focus on the 2XXX and 6XXX series alloys and their weldability. Crack sensitivity is a major factor when welding or melting aluminum alloys. Since aluminum has a high coefficient of thermal expansion, which leads to a large volume change during solidification, a wide solidification temperature range leads to crack sensitivity. This sensitivity is increased in heat-treatable aluminum alloys due to the high amounts of alloying additions in the melt. This cracking can be divided into two categories: solidification cracking that is observed in the center of the melt or terminal craters and liquation cracking that occurs along the fusion line and in the heat affected zone adjacent to the melt [17]. Solidification cracking is mainly attributed to thermal stresses along with composition of the alloy. High heat inputs are also believed to contribute to solidification cracking. Electron beam welding, which has a minimal heat input, should reduce crack sensitivity [23]. The primary method for controlling crack sensitivity is, however, by controlling melt composition through alloy additions. Figure 2.7 shows the crack sensitivity as a function of weld composition for various binary alloys [17]. More complex alloy systems may be more sensitive to minor alloying editions by widening the solidification temperature range. Figure 2.8 shows the effect of alloying elements on crack sensitivity in a ternary (Al-Cu-Mg) system and a quaternary (Al-Mg-Si-Cu) system. These experimental results can be applied to the 2219 and 6061 aluminum alloys.

Liquation cracking occurs in the heat affected zone when constituents with low melting points liquate at the grain boundaries [31]. Heat-treatable alloys have high amounts of alloying additions which can form low melting eutectic phases, making liquation cracking a concern during welding.

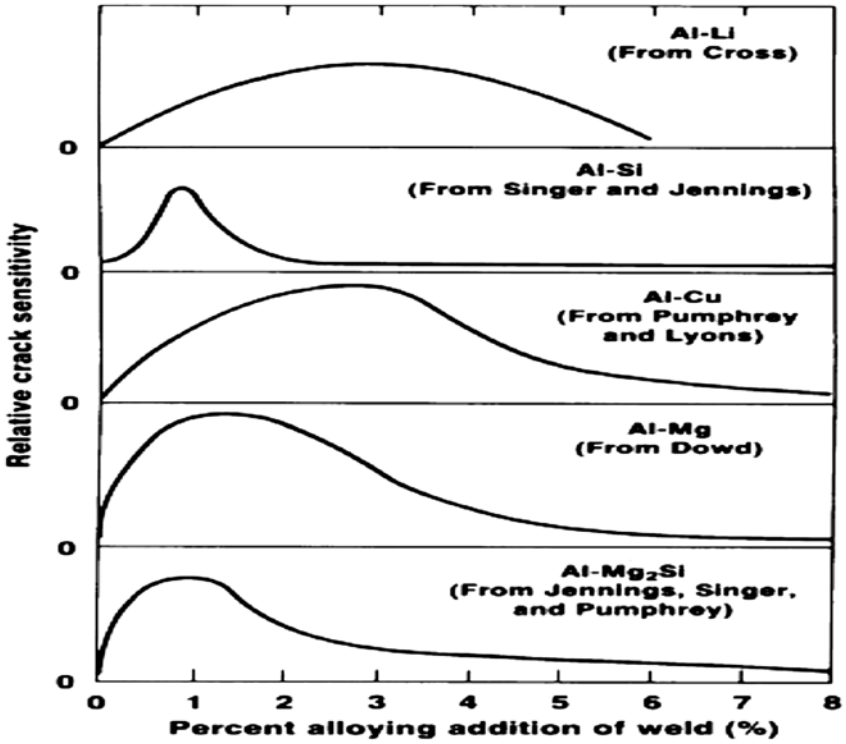

Figure 2.7 From top to bottom: experimental results crack sensitivity of 8XXX [24], 4XXX [25], 2XXX [26], 5XXX [27], and 6XXX [28] series alloys.

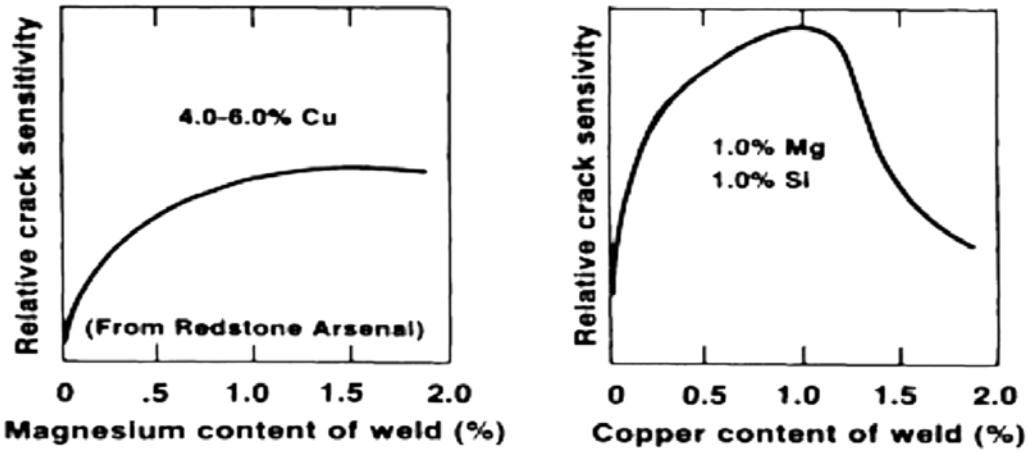

Figure 2.8 The crack sensitivity of (Al-Cu-Mg) system [29], and (Al-Si-Mg-Cu) system [30].

Al 2219 alloy can be welded with or without a filler metal; Al 2319 is a common filler used when required. Al 2319 has a similar composition to Al 2219 alloy but with some additions of silicon and iron to accommodate vapor loss and increase fluidity during welding and titanium for grain size control. Al 4043 alloy with 5 wt. % Si addition can also be used but may result in

low ductility. Al 5XXX series filler alloys are not recommended due to the increase of crack susceptibility with increasing magnesium content as seen in Figure 2.8. Al 6061 alloy has relatively high crack susceptibility, shown in Figure 2.8, therefore, welding this alloys requires some filler material to decrease crack susceptibility. Generally, either Al 5356 alloy with 5 wt. % Mg additions or Al 4043 alloy is used as a filler metal for welding Al 6061 alloy. Both filler alloys replenish magnesium and silicon that vaporize during welding and stabilize the composition to reduce cracking susceptibility.

As with all aluminum alloys, MMCs must be cleaned and maintained in a shielded environment during joining. The reinforcement particles can affect several variables during welding. Since the reinforcement does not melt, or fully melt, the weld pool remains more viscous than monolithic aluminum, thus, the weld pool does not wet as readily with the base material [32]. Heat flow is also affected due to the differences in thermal conductivity and thermal expansion coefficients between the matrix and the reinforcement and can affect resulting microstructures and stress distributions in the weld. Chemical reactions can also occur during melting. Aluminum carbide can form at the interface at high temperatures as described by Eq. 1 and 2. The increase of silicon activity because of its addition to the aluminum melt may inhibit the formation of aluminum carbide. Filler material with high silicon content (4XXX series) is recommended for joining aluminum based MMCs. Solidification can also be affected by the reinforcement. Below a critical solidification rate, the particles are pushed ahead of the solidification front causing them to agglomerate in the last regions to solidify. This partitioning can locally hinder heat flow and cause a decrease in microsegregation which decreases the amount of secondary phases to form [33].

Gas tungsten arc welding and electron beam welding are both suitable processes for joining most SiC reinforced aluminum composites. For the GTAW process, a filler wire is recommended to suppress aluminum carbide formation. Alloys 4043, 4045, and 4047 are recommended for this purpose. Al 4045 and Al 4047 would be more effective in suppressing aluminum carbide formation but may not be suitable for heat treatment due to coarsening of the silicon phase [34]. For the GTAW process parameters, a balanced or penetrating arc allows for the particles to penetrate into the weld and result in an improved bead profile. Electron beam welding of Al-MMCs resulted in a decrease in aluminum carbide formation, fine grain size and even distribution of reinforcement particles compared to laser beam welding. Higher travel

speeds and sharper beam focus were observed to create less aluminum carbide [35]. Laser beam welding is not recommended for silicon carbide reinforced aluminum composites due to the optical properties of the material. Aluminum reflects the light of the laser beam, whereas silicon carbide absorbs the light. The energy from the laser becomes concentrated near the silicon carbide particles, decomposing them and increasing the formation of aluminum carbide in the matrix [35].

2.6 Application of Fluid Mechanics to Predict Particle Dispersion in Metal Matrix Composites

Solidification of metal matrix composites can be modeled using fluid mechanics of insoluble particles suspended in a liquid [36]. A thermodynamic model was created to predict the critical interface velocity (v_{cr}) for dispersion in the matrix. Insoluble particles are pushed ahead of the solidification front to the final freezing regions when the velocity is below the critical velocity. When the velocity is higher, the particles will become engulfed [37]. This behavior can also be affected by other interaction variables such as viscosity of the liquid metal, interfacial energies of wetting, density of the liquid, degree of convection in the liquid, particle shape and density, and the volume fraction of particles [38]. Force balances from fluid mechanics can be used to determine the buoyancy of a particle in the liquid metal, given by Equation 4 [39].

$$\boldsymbol{F_S} + \boldsymbol{F_k} = \boldsymbol{F_w} \qquad (2.4)$$

where F_s is the buoyancy force, F_k is the friction force and F_w is the force due to gravity. This equation can be expanded to:

$$\frac{4}{3}\pi r_p^3 \rho_1 g + 6\pi\eta r_p v_1 = \frac{4}{3}\pi r_p^3 \rho_p g \qquad \textbf{(2.5)}$$

where r_p is the particle radius, ρ_1 is the liquid density, η is the viscosity of the liquid, v_1 is the liquid velocity, ρ_p is the particle density and g is the acceleration due to gravity. In this equation the reinforcement particles are assumed to be spherical. In this system the liquid velocity of the melt required to suspend a particle (if the particle density is greater than that of the fluid) is given by Lajoye and Suery [40]:

$$v_s = \frac{2(\rho_p - \rho_1) g * r_p^2}{9\eta} \qquad (2.6)$$

If the density of the liquid is greater than the particle the density values are switched and the

steady state velocity will be given by:

$$\boldsymbol{v_{ss}} = \frac{\mathbf{2}(\boldsymbol{\rho_1} - \boldsymbol{\rho_p})\boldsymbol{g} * \boldsymbol{r_p^2}}{\mathbf{9}\boldsymbol{\eta}} \qquad (2.7)$$

If the velocity of the particles moving in the melt pool is greater than the steady-state velocity of particles suspended in the same liquid under equilibrium, the particles should disperse. If the melt pool velocity is less than that of the steady-state velocity, the particles will be pushed ahead of the solidification front and agglomerate. Woods and Milner proposed that fluid motion is caused by the Lorentz force and the molten pool velocity is directly proportional to the square of the arc current, as shown below:

$$v_{mp} \propto I^2 \qquad (2.8)$$

If the molten pool velocity is greater than the steady-state liquid velocity, dispersion is to be expected. If the opposite is true the particles will sink or float, depending on density, and agglomeration is more probable [40].

CHAPTER 3: EXPERIMENTAL PROCEDURE

This chapter introduces the experiments conducted for this research. The procedures for these experiments are discussed below.

3.1 Powder Cored Tubular Wire Manufacturing

The EBF^3 wall builds were made using a set of experimental powder cored tubular wire feedstock developed and manufactured at the Colorado School of Mines. The powder cored tubular wires (PCTW) are manufactured using 0.406 mm thick x 12.7 mm wide, Al 5052 alloy sheath material and filled with a powder mixture of silicon carbide particulates and elemental alloying additions to achieve the desired 6061/SiC/10p final composition. The wire forming process begins by feeding the aluminum sheath into a rolling mill, shown in Figure 3.1, which forms the sheath to accept the powder, fills the tube with the powder and seals the tube using a lap-joint method. A motorized capstan is used to continuously pull the sheath through the forming rolls until the powder is completely used. Figure 3.2 illustrates the forming steps used to create and seal the PCTW.

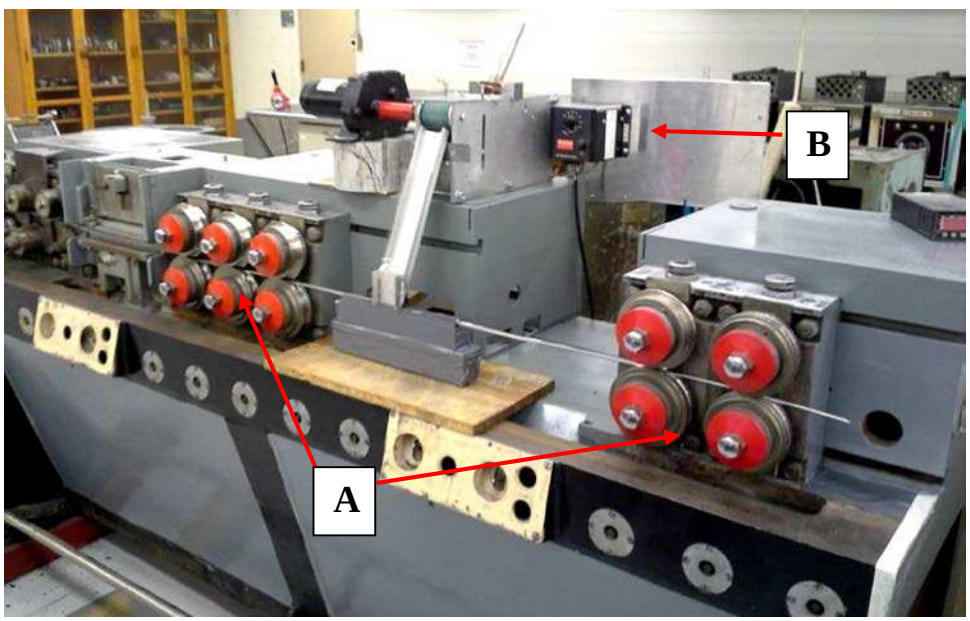

Figure 3.1 Photograph of the tubular wire mill showing the A) forming rolls and B) powder feed system.

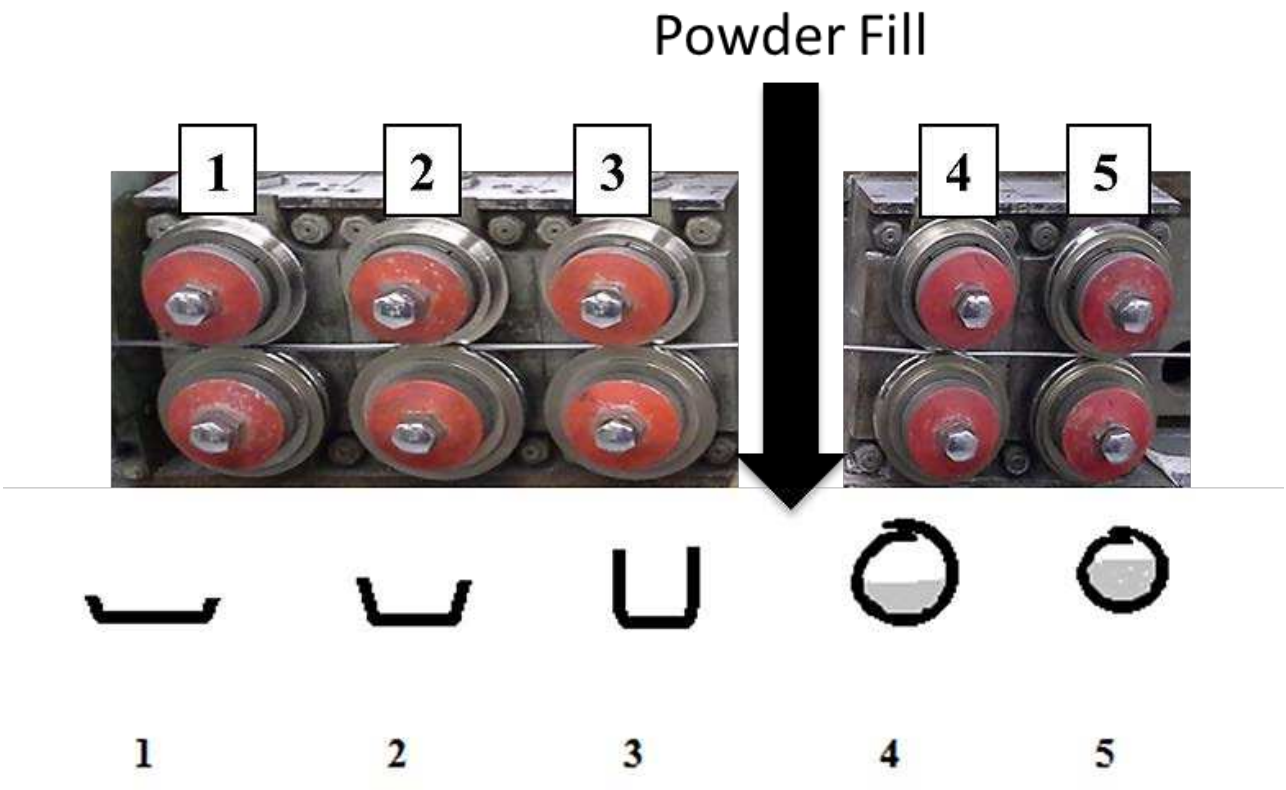

Figure 3.2 Tubular wire mill forming schematic showing the formation of the tubular wire and powder filling.

The powder is fed into the wire as the sheath passes between the third and fourth rolling dies by a belt fed conveyor system, shown in Figure 3.3. The conveyor belt is calibrated to fill the sheath with a 16 pct. fill ratio to achieve optimized compaction upon completion of the wire manufacturing process [2]. Incorrect fill ratios may lead to under-filling or over-filling of the wire. Under-filling would result in powder shifting and segregation. Over-filling would lead to localized stress risers and abrasion, which can result in wire breakage during further processing. After powder filling, the final rolling dies close the sheath by creating a lap-joint and the seal is closed off. The final diameter of the wire after it leaves the closing dies is 4.32 mm illustrated in Figure 3.4. The powder is still loose inside the wire at this diameter; to eliminate powder shifting, a preliminary wire reduction to 2.54 mm is applied.

The wire must be further reduced to a final diameter of 1.6 mm to meet the requirements of the EBF^3 system. This reduction is carried out by drawing the wires through a series of

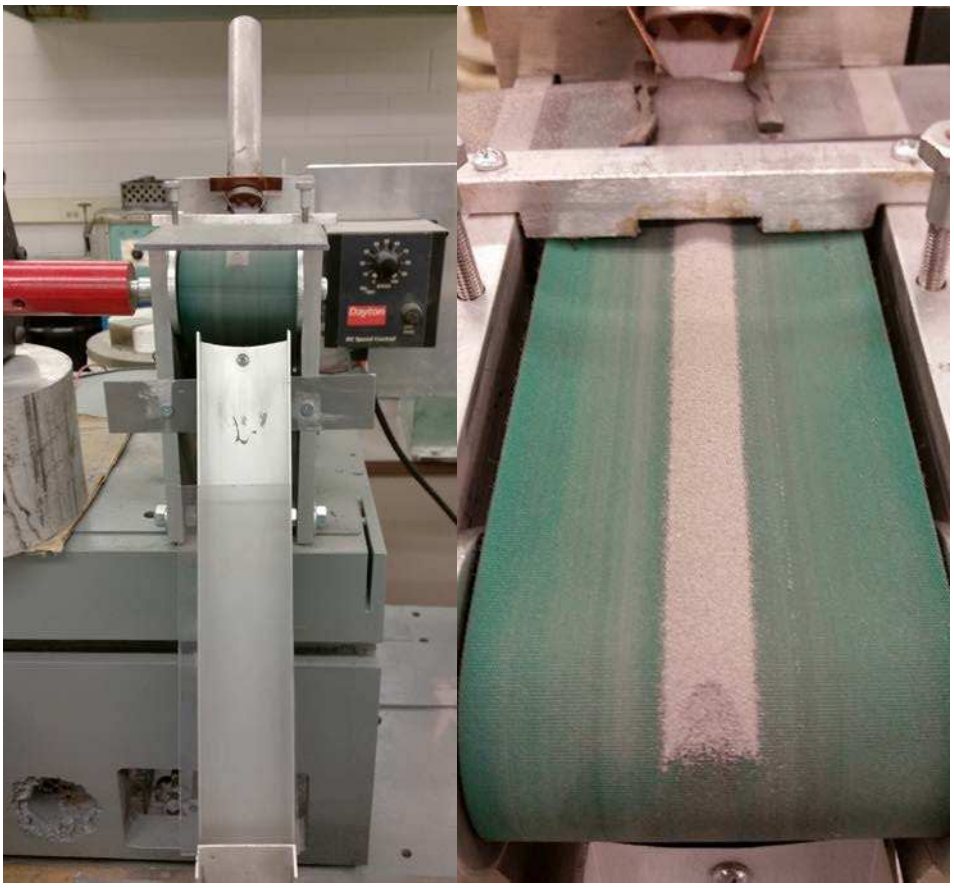

Figure 3.3 Conveyor belt powder feed system for homogenous powder distribution in the wire. Uniform powder fill ratio is maintained using this method.

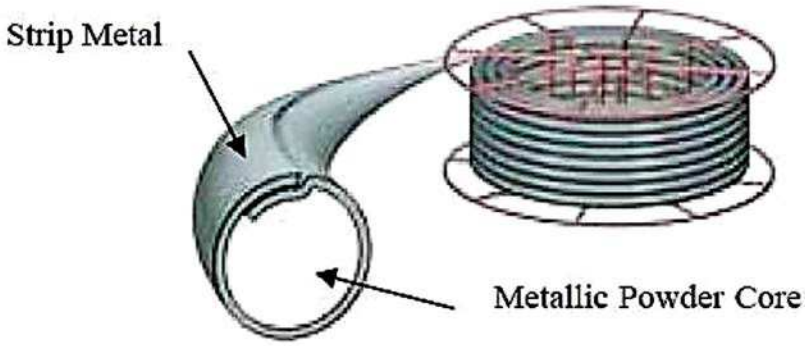

Figure 3.4 Illustration of a fully sealed powder cored tubular wire showing the lap joint method for sealing the powder in [2].

reducing dies to achieve the desired diameter. The wire is spooled on a free-spinning capstan. The tip of the wire is swaged and fed through the die to start the reduction. A motorized capstan is attached to the swaged end and used to pull the wire through first a granular lubricant, then through a number of reducing dies in sequential order until the final diameter is reached. The wire drawing process is shown in a schematic in Figure 3.5. Upon completion, the wire is spooled and annealed in a vacuum furnace. Annealing will reduce any residual stress which will lead to better wire feeding during deposition and no un-spooling during storage. The vacuum annealing step will also evaporate any organic contaminates on or inside the wire from handling and lubrication during drawing, reducing the possibility of porosity during deposition.

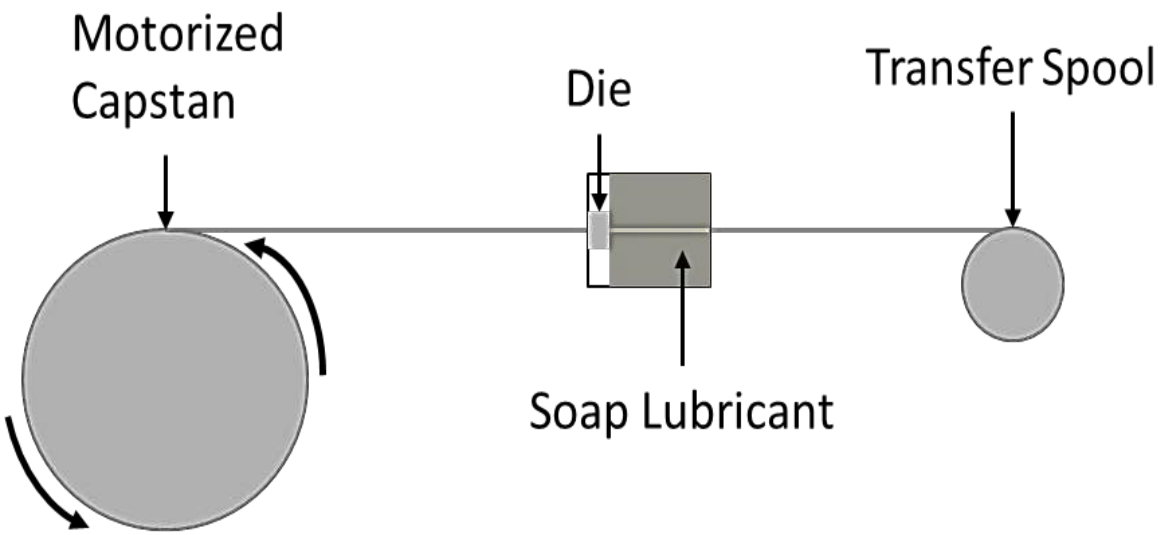

Figure 3.5 Wire drawing schematic showing the die and lubrication station as well as the motorized and transfer spools [5].

3.2 Silicon Carbide Particles

Five variations of silicon carbide particles were used in the powder cored tubular wires. Uncoated (UC) silicon carbide particles were used as a baseline for comparison with the coated particles. Copper and nickel coated particles were chosen for the research based on conclusions in literature that copper and nickel enhance wettability and mitigate aluminum carbide formation. Coated silicon carbide particles were purchased from Federal Technology Group. Two batches of copper-coated particles were created using a patent-protected electroless coating followed by an electrolytic plating process in an aqueous solution. One batch was created to have a high weight percentage of copper coating content designated as (HCC). Another batch of powders

was made with a low copper content (LCC). Two batches of nickel-coated particles were made using an electroless plating process to create particles coated with high nickel content (HNC) and low nickel content (LNC) [41]. Each of these coated particles were produced with the objective of increasing wettability, promoting dispersion and mitigating aluminum carbide formation in the aluminum melt. As control, uncoated silicon carbide powder was used in a fifth wire to provide baseline comparison regarding the effectiveness of coating on suppressing the reactions above mentioned.

3.3 Particle Characterization

Silicon carbide particles as well as elemental alloying powders were added to the wire as a well-dispersed powder blend. Aluminum, silicon, copper, and chromium were added as elemental powders to achieve the desired as-deposited composition in the matrix of the deposit. Silicon carbide, whether uncoated or coated with copper or nickel, was added to the powder blend to serve as the reinforcement. Before each powder blend was made, each of the powders were examined by light optical microscopy and scanning electron microscopy (SEM) to determine the powder morphology, size and cleanliness. The particles were then tested using static laser light scattering to determine the particle size distribution.

3.3.1 Static Laser Light Scattering

Static laser light scattering uses the interaction between light and particles to determine the size of the particles. Particle size is determined by intensity characteristics of the scattering pattern at various angles illustrated in Figure 3.6. The laser light scattering process is conducted by introducing a small volume of particles into an aqueous medium contained in a cylinder. The particles suspended in the liquid slowly sink at the rate of gravity. As the particles sink, they pass though the path a monochromatic light source. The particles scatter the light at different angles depending on size and the scattered light waves are collected by a detector. Accurate measurements of particle size are dependent on the condition that the particles have sufficient space so that scatter patterns from different particles do not interfere with each other. Liquid dispersants may also be used if particles have a tendency to agglomerate. Powders must be of the same material and may not be mixtures of different powders. Accurate measurements require isotropic particles with the same optical properties [42].

3.4 Wire Characterization

Wire samples were taken from the intermittently from the spool as the wire was consumed during deposition. The sections were mounted in epoxy both axially and longitudinally. The samples were ground to expose the powder core and were examined using

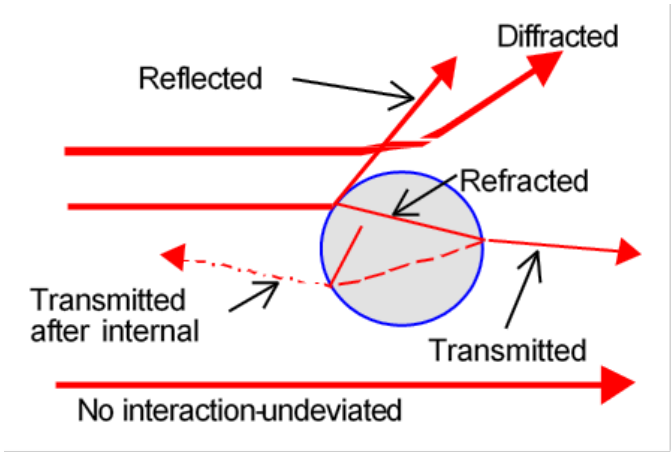

Figure 3.6 An illustration of monochromatic light rays interacting with a particle [42].

scanning electron microscopy to determine the distribution of each of the powders along the length of the wire as well as the presence of any large voids in the wire which could indicate powder shifting and lead to porosity. The sections were also examined to determine the volume fraction of silicon carbide in the powder cored wire to verify the target volume fraction of reinforcement was being reached.

3.5 EBF3 Deposition

Deposits were made using the Electron Beam Freeform Fabrication System (EBF^3) at NASA Langley Research Center. The EBF^3 process is conducted using a 42 kW electron beam welder with a six-axis, computerized numerical controlled deposition stage and optional dual wire feed capabilities. A build volume of up to 182 cm x 60 cm x 60 cm can be deposited in a high vacuum (10^{-7} Torr) environment [2]. A photograph of the complete EBF^3 system is pictured in Figure 3.8. Five wires containing different types of coated and uncoated silicon carbide particles were used as feedstock to make single and multiple layer deposits 152 mm long x 6 mm wide. Four sets of beam conditions were used to deposit builds of each wire. Novel sets of beam conditions were used on specific wires to determine the acceptable range of the parameters.

Voltage, wire feed rate, traverse speed, and build height were held constant while beam focus, beam motion, pulse frequency and beam current were varied for each one of the wires. Specific deposition parameters are proprietary, consequently these values have been normalized to convey the deposition variations while protecting ownership rights. Four conditions were created for the experimental matrix. Three focused rastered beam conditions were studied. The pulsing conditions were set at zero (F_0), low frequency ($F_{0.25f}$) and high frequency (F_f). The fourth condition studied was a defocused beam with no beam motion or pulsing (D_0).

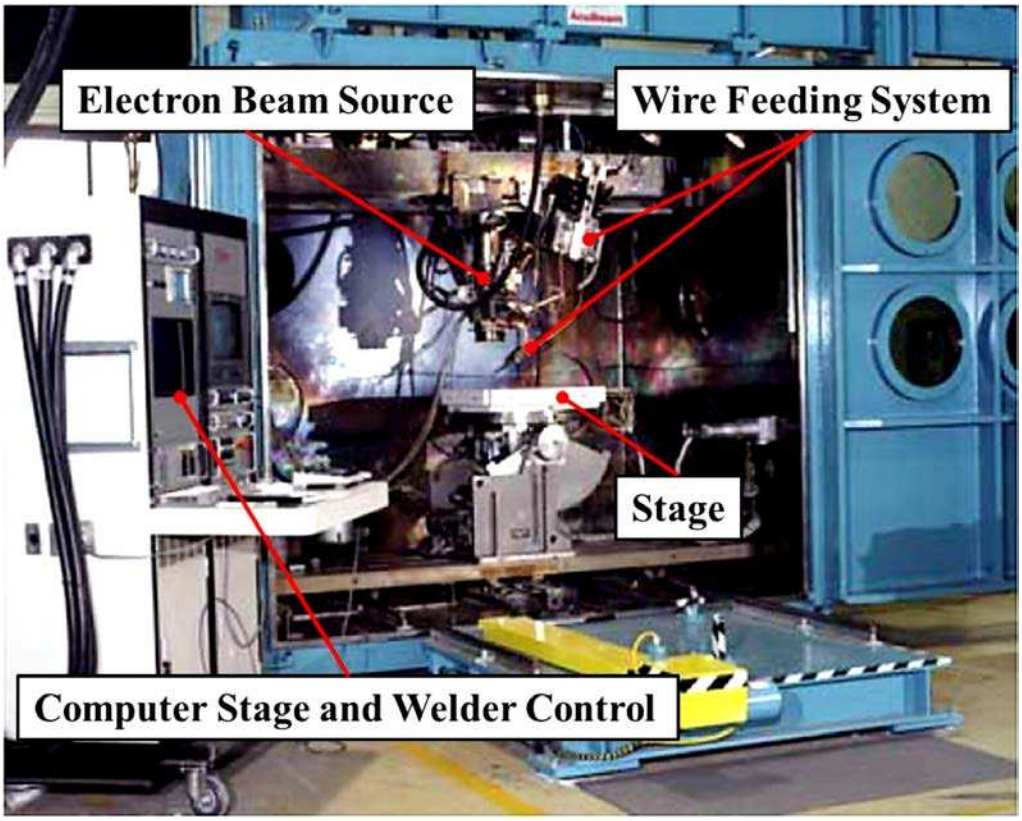

Figure 3.7 Photograph of the EBF^3 system showing the various controlled components [2].

3.6 Deposition Characterization

Deposits were characterized to determine the effect that beam conditions and coating variations have on metal matrix composite deposits. Cross-sections of single layer deposits were examined to determine changes in deposit morphology, composition and the tendency for clusters to form during the melting. Multi-layer deposits were examined to determine the volume fraction of silicon carbide particles in the overall build compared to the volume fraction in the

wire. Microstructural analysis was performed to determine solidification structures, secondary phases and defects in the matrix. The amount of aluminum carbide formed was qualitatively measured for each deposit. Compositional analysis was performed on samples of wire and deposits to verify that specifications are met after the deposition process is completed.

3.6.1 Microstructural Analysis

Cross-sectioned samples were extracted from the steady-state regions of single layer and multiple layer deposits for all beam conditions and feedstock material variations. The samples were rough ground to a flat surface and fine ground on 1200 grit silicon carbide paper. The samples were then polished using 9 micron, 3 micron and 1 micron diamond solutions, respectively, on low nap LECO imperial cloth. Final polish was conducted to mirror finish using 0.05 micron colloidal silica solution on Buehler Nylon polishing cloth.

The polished, cross-sectioned samples were examined using environmental scanning electron microscopy (ESEM). Low magnification composite images were taken to show the deposit morphology. High magnification images were taken to reveal microstructure and defects of the deposits. Detection and qualitative analysis of aluminum carbide was conducted to determine if coatings or beam conditions could have any effect on mitigating its formation. Interdendritic phases were identified as well as the susceptibility of the deposit to solidification cracking.

3.6.2 Compositional Analysis

Two samples of 100 mg were cut from deposits containing each of the five coating conditions. Each pair of samples was extracted from deposits of the same beam conditions for all five sets. Five 100 mg samples were cut from wires corresponding to their respective deposits of the five different coating conditions. One 100 mg sample was cut from a certified composition Al 6061 alloy plate to serve as a standard for the fifteen samples. All sixteen samples were digested in nitric acid on a hot plate, diluted with deionized water and analyzed using inductively coupled plasma – optical emission spectrometry (ICP-OES). ICP-OES is conducted by nebulizing a solution containing the dissolved analyte elements into a mist which is forced into a plasma. The plasma generates enough energy to excite the electrons of the analyte elements to higher energy states. As the electrons return to their lowest energy states, photons are emitted with wavelengths corresponding to differences in energy states. The photons are then resolved by a monochromator and detected by a photomultiplier as illustrated in Figure 3.9. Emission

intensities from the solution are compared to calibration curves of each of the elements being analyzed to determine concentration of said elements. Calibrated emission intensities show a linear relationship to elemental concentrations over five orders of magnitude so concentrations as low as 0.0001 pct. can be determined. All accurate analyses must be conducted in aqueous state, so solid samples must be completely dissolved [43].

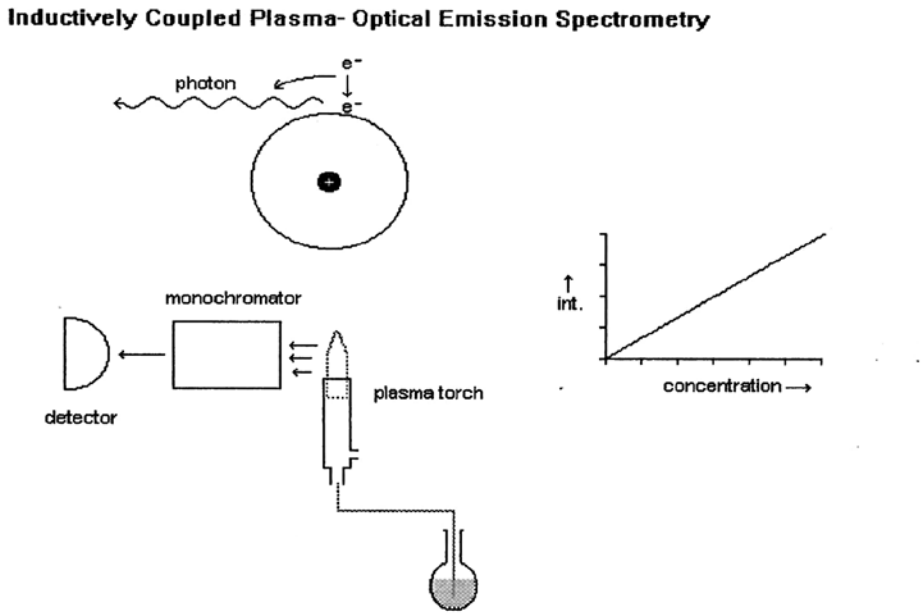

Figure 3.8 Schematic showing the ICP-OES analysis technique, the method by which photons are emitted, and the linear relationship between photon intensity and concentration [43].

3.6.3 Reinforcement Analysis

Silicon carbide reinforcement particles were identified in the matrix using scanning electron microscopy. Macroscopic cross-sections were taken to analyze the particle retention and dispersion in the matrix. Contrast differences in backscattered images showed silicon carbide particles to be darker than the matrix. Fiji Imaging Software was used to characterize the particles in the matrix. Image adjustment functions of the software were used to enhance the grayscale contrast between the silicon carbide particles and the matrix. Background and non-melted base metal were cropped from the picture to acquire a more accurate measurement of the overall area of the cross-section. The thresholding function of the software allows for certain shades of grayscale to be highlighted and analyzed. The particles were highlighted, colored and

analyzed to measure the volume fraction of particles in the cross-section. Figure 3.10 shows how the image analysis was conducted.

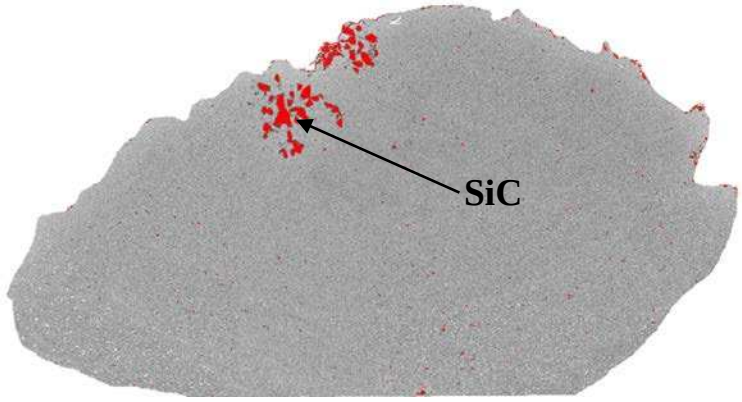

Figure 3.9 Screenshot showing the method for identifying SiC particulates and determining volume fraction of the silicon carbide in the matrix.

Silicon carbide was found in clusters in the matrix. Fiji was used to measure the size of each cluster in the matrix. Clusters were highlighted as a single particle and measured for cross-sectional area as demonstrated in Figure 3.11. From this measurement, the mean free path between clusters of particles was calculated to determine the effect of beam conditions and material properties on particle dispersion in the matrix. Mean free path of the clusters of particles is given by [44]:

$$\frac{4}{A * n_v} \qquad (3.1)$$

where A is the cross sectional area of the cluster and n_v is the number of clusters per unit volume. Area and mean free path calculations were normalized by the volume fraction of the silicon carbide in the matrix to achieve comparable values. The values were compared to determine the effectiveness of implementing different coatings to the particles and adjusting beam conditions.

3.7 Predicting Particle Dispersion and Mitigating Aluminum Carbide Formation

Interactions between the silicon carbide particles and the aluminum matrix were modeled thermodynamically and kinetically to understand the particle-matrix interface. These models can be used to determine the ability for silicon carbide to disperse in aluminum. The matrix and

reinforcement can then be modified to enhance dispersion in the matrix as well as potentially mitigate aluminum carbide formation. Equilibrium phase diagrams and Gibbs free energy values were calculated using thermodynamic calculation software for various scenarios of particle-matrix interactions to predict the susceptibility of aluminum carbide formation. A basic empirical

3.10 Thresholding demonstrating the method for determining the area of each cluster and the amount of clusters in each multilayer deposit for calculating the mean free path.

heat diffusivity formula was applied to predict the affinity for silicon carbide to be rejected or captured by the matrix. A kinetic model was developed using fluid mechanics to determine conditions to enhance particle dispersion in the matrix.

3.7.1 Predicting Equilibrium Thermodynamics of the Metal Matrix Composite

Two software packages were used to predict reactions and phase transformations likely to occur during deposition. Thermo-Calc computational modelling software is used for creating equilibrium phase diagrams and performing Scheil calculations on the simulated composition for solidification under equilibrium cooling conditions. The software package has capabilities for

calculating other thermodynamics related data, but these modules were not used for this project. Pseudo-binary phase diagrams were generated for the target composition of Al 6061 alloy with the addition of 10 vol. pct. silicon carbide. Magnesium and silicon were varied respectively to simulate the loss of these alloying elements due to ejection or vaporization during deposition. Isothermal ternary diagrams were generated to examine the interaction of the coatings, or surrounding matrix, with the silicon carbide. Scheil solidification diagrams were also constructed to predict what phases would be present during solidification under equilibrium conditions. This software uses equilibrium thermodynamics for the calculations so interpretations must be made to predict which reactions will occur during non-equilibrium thermal cycles.

The software calculates values based on large thermodynamic databases for different material systems which are taken from literature and standards. Creating a diagram requires the operator to choose a database for the material system being examined. The chosen database will allow for certain elements to be selected for analysis. After the elements are selected all of the possible phases and constituents that can be formed with said elements is shown and can be manipulated to calculate, or not, which phases will be examined by the software.

The data is processed and passed to a subsequent screen which allows for the desired composition, temperature (range), and atmospheric pressure to be set. The parameters are again processed and stored. After all iterations are calculated, a screen is shown where the desired data to be calculated is set. The software can then compile all of the data and generate a plot in the form of a phase diagram, solidification curve or other thermodynamic plots shown in Figure 3.11. The process for setting the data is the same for any plot being generated. Changes to settings of the x-axis and y-axis determine what type of plot will be generated. Ternary plots will be created by clicking the triangular plot function on the toolbar during the final step.

Equilibrium reaction equations were calculated using HSC Chemistry thermodynamic software. This computational modeling software has multiple calculation modules for computing thermodynamic values and creating fundamental diagrams.

The calculations used for this project were made using the Reaction Equations module of the software. A predetermined balanced reaction equation is input into the software. The temperature range and step size for the calculations can be set for a desired set of data. Figure 3.17 illustrates the input values and units that can be manipulated. The data is then calculated in the software and generates a table of values. Change in enthalpy, entropy, and Gibb’s free energy

are calculated as well as the equilibrium constant for temperatures determined by the step size, as demonstrated by Figure 3.18.

Equilibrium data calculated from both software packages was used to predict potential reactions that may occur in the melt. The reactions predicted represent local regions in the melt, near the particle-matrix interface, where equilibrium states may be present. This data was used as an approximation to explain the reactions occurring in the melt.

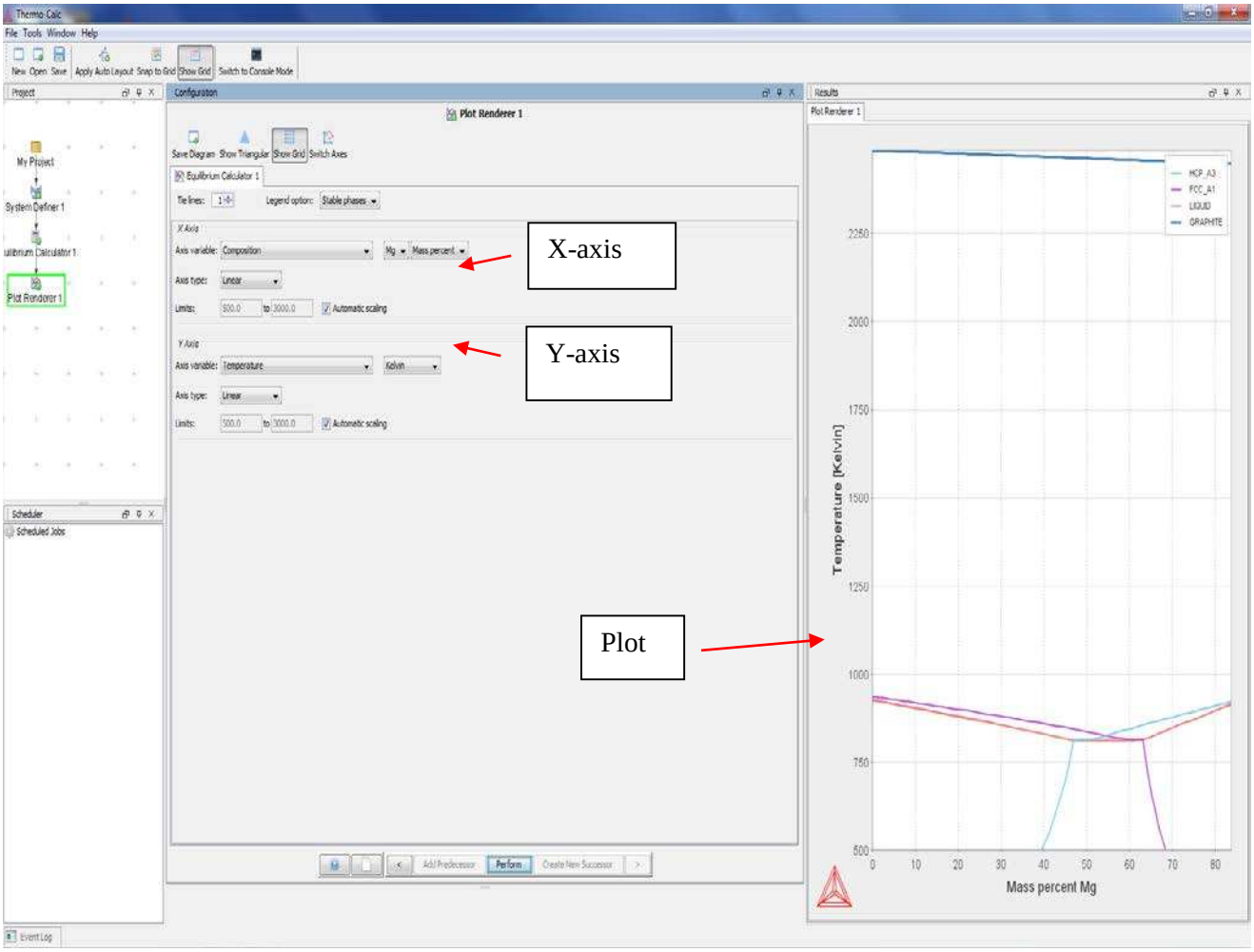

Figure 3.11 Image showing the process for creating a plot using the data previously calculated.

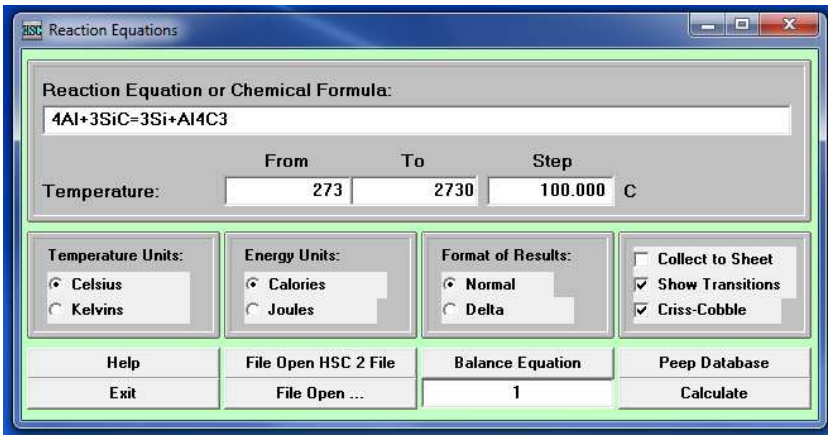

Figure 3.12 The reaction equation module showing the values and units that can be varied form computing fundamental thermodynamic values of the system.

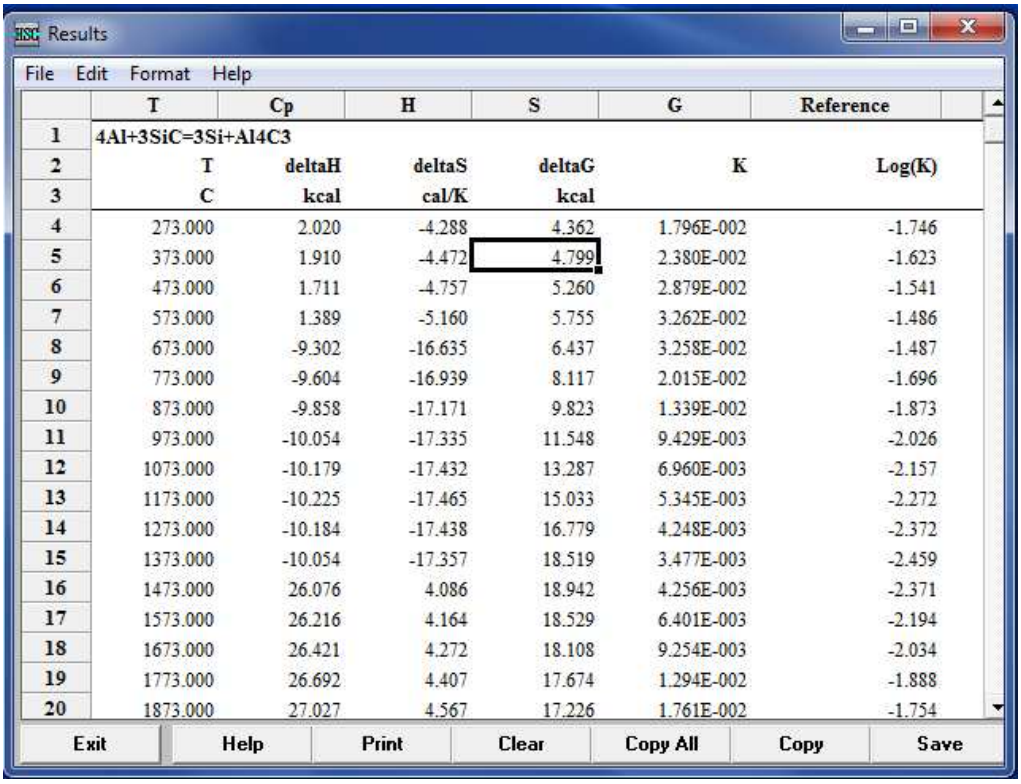

Results

File Edit Format Help

	T	Cp	H	S	G	Reference
1	4Al+3SiC=3Si+Al4C3					
2	T	deltaH	deltaS	deltaG	K	Log(K)
3	C	kcal	cal/K	kcal		
4	273.000	2.020	-4.288	4.362	1.796E-002	-1.746
5	373.000	1.910	-4.472	4.799	2.380E-002	-1.623
6	473.000	1.711	-4.757	5.260	2.879E-002	-1.541
7	573.000	1.389	-5.160	5.755	3.262E-002	-1.486
8	673.000	-9.302	-16.635	6.437	3.258E-002	-1.487
9	773.000	-9.604	-16.939	8.117	2.015E-002	-1.696
10	873.000	-9.858	-17.171	9.823	1.339E-002	-1.873
11	973.000	-10.054	-17.335	11.548	9.429E-003	-2.026
12	1073.000	-10.179	-17.432	13.287	6.960E-003	-2.157
13	1173.000	-10.225	-17.465	15.033	5.345E-003	-2.272
14	1273.000	-10.184	-17.438	16.779	4.248E-003	-2.372
15	1373.000	-10.054	-17.357	18.519	3.477E-003	-2.459
16	1473.000	26.076	4.086	18.942	4.256E-003	-2.371
17	1573.000	26.216	4.164	18.529	6.401E-003	-2.194
18	1673.000	26.421	4.272	18.108	9.254E-003	-2.034
19	1773.000	26.692	4.407	17.674	1.294E-002	-1.888
20	1873.000	27.027	4.567	17.226	1.761E-002	-1.754

Exit Help Print Clear Copy All Copy Save

Figure 3.13 Image of a generated table showing the results of the equilibrium reaction at various temperatures.

3.7.2 Predicting Particle Dispersion Using Fluid Mechanics

A simplified computational fluid mechanics model was used to predict how particles will disperse in a molten metal pool under non-equilibrium conditions. This model was used to determine if the kinetics in the molten pool are sufficient to homogenously disperse silicon carbide particles in the aluminum matrix with and without nickel and copper coatings. A comparison is made between the velocities of a particle moving in a liquid matrix under steady-state and non-equilibrium conditions. If the melt pool, or non-equilibrium velocity is greater than that of the same liquid under equilibrium melting and cooling conditions, dispersion will occur. The steady-state velocity is calculated using EQ 2.6 or EQ 2.7 depending on the density of the particle relative to the liquid. The particles used for this calculation are assumed to be silicon carbide particles with no coating. The density of the silicon carbide particles was taken from material constants determined by literature. The particle radius used for the steady state was determined through laser light scattering of the particles used in the experiment. Calculations varying viscosity and temperature used a constant particle radius equivalent to the mean particle radius determined by laser light scattering. The radius is the main effect by the particle on the system.

Viscosity, η, is the variable contribution by the liquid. Viscosity is given by the equation [45]:

$$\boldsymbol{\eta = \eta_0\, exp(\frac{E}{RT})} \qquad (3.2)$$

where $\eta_0$is the material constant for viscosity, E is the activation energy for the material, R is the Boltzmann constant and T is the temperature. It is known that viscosity varies with temperature, so steady-state velocity calculated using viscosity in EQ 2.6 and EQ 2.7 will also vary by temperature. To calculate the viscosity, temperature of the melt pool must be measured to gain a comparable temperature range for analysis. To measure the temperature, a deposit was made using a modified gas tungsten arc freeform fabrication ($GTAF^3$) chamber. The chamber was built to simulate conditions experienced in the EBF^3 deposition chamber. As the deposit was made, a high temperature infrared pyrometer was positioned to monitor the temperature of the melt pool. Data collected from this was used to estimate a temperature range the melt pool will experience during EBF^3 deposition. From this, a range of melt pool viscosities was also determined. It was assumed that the coating would be completely liquid during deposition, so it would mix and become part of the matrix. According to literature, several intermetallic compounds

preferentially form in Al-Ni and Al-Cu system. Liquid metal compositions equivalent to Al_3Ni, AlNi, and $AlNi_3$ were chosen to simulate local liquid regions of nickel-coated particles. Liquid compositions equivalent to Al_2Cu and $Al_{0.1}Cu_{0.9}$ were chosen to simulate local liquid regions surrounding copper-coated particles [46]. The rule of mixtures was applied to calculate viscosity values for these compositions at the range of melt pool temperatures. Measurements of particle radius, temperature were used to calculate steady-state velocity values for engulfing coated and uncoated silicon carbide particles in an aluminum matrix.

Melt pool velocity was determined using high speed video analysis of the pool during deposition. The $GTAF^3$ system was used to make deposits of wire containing coated and uncoated silicon carbide particles. A high speed video camera was positioned to view the trailing end of the deposit. It was calibrated for measuring distances by placing a scale bar in both the x-direction and y-direction of the frame. Still images were processed and used to calibrate pixel to distance ratios in the frame shown in Figure 3.19. Once calibrated, deposits containing silicon carbide were made while recorded by the high speed video camera. Silicon carbide particles and clusters floating on the surface of the melt act as tracers for determining motion in the melt pool. Videos taken by the high speed camera were converted into images with associated time stamps. The tracer particles' motion was tracked by digitizing the still frames and collecting x-y coordinates illustrated in Figure 3.20. Velocity of these particles were calculated by taking the difference in position over the time difference of each frame. Values were given in mm/s. The measured melt pool velocities were then compared to calculated steady-state velocities to determine if dispersion is likely to occur. The data was compared with image analysis of deposits to validate the model.

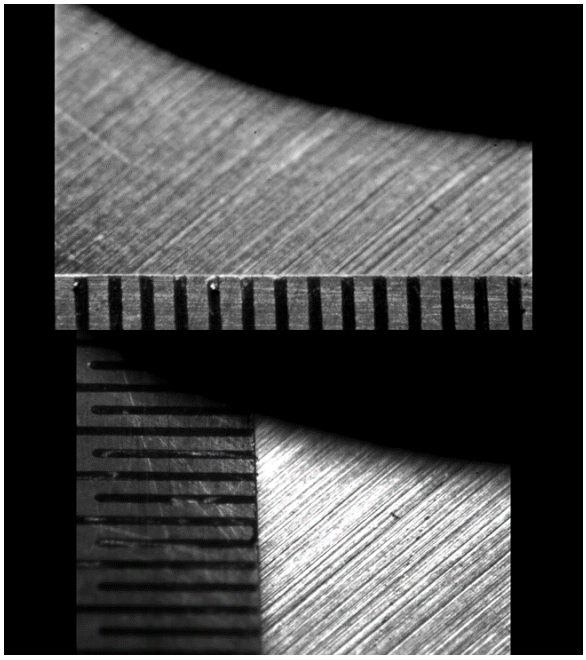

Figure 3.14 Still images showing the calibration method for calibrating distance to pixel ratio in on the high speed video. Increments given in 0.40 mm.

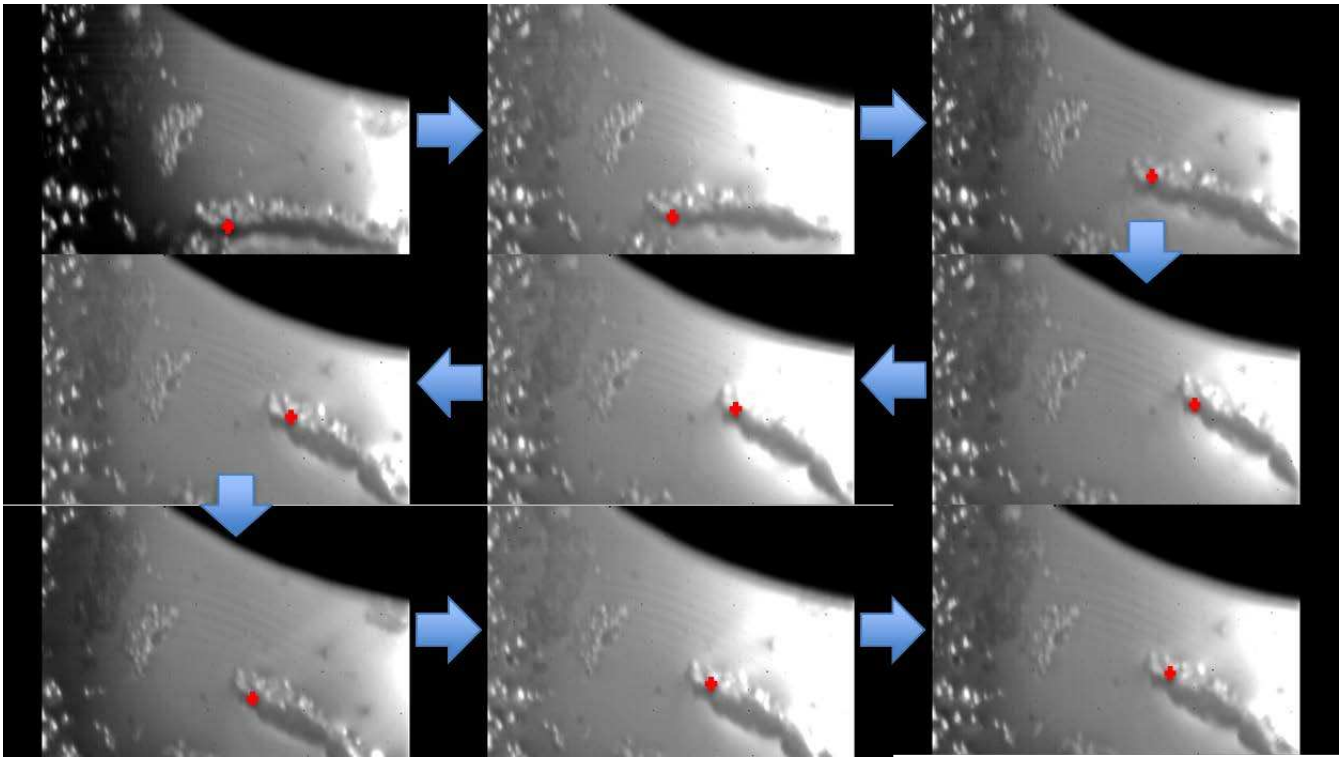

Figure 3.15 Still image time lapse showing the position tracking of the tracer particles indicated by dots.

CHAPTER 4: RESULTS AND DISCUSSION

This chapter discusses the results obtained from experiments developed in the previous chapters.

4.1 Consumable Characterization

Alloying and reinforcement powders were examined for size distribution and morphology. Light optical microscopy showed powder morphology. Scanning electron microscopy was then used to determine the consistency of coverage for the coated silicon carbide particles. Size distribution was determined using laser light scattering analysis on each of the individual powders.

The longitudinal cross-sectioned samples were used to determine the volume fraction of silicon carbide in the wire prior to deposition. The results were used to determine the amount of powder loss during the filling and drawing processes. The data collected was compared with the volume fraction of silicon carbide in deposits to determine the degree of powder loss during different processing steps. Approximately half of the powder fill was lost during the wire manufacturing process. Longitudinal analysis of cross-sections of the wires conducted by scanning electron microscopy was compared with x-ray radiography of the wires to qualitatively determine if the powder core maintained a uniform distribution throughout different lengths of wire. The results from both sets of analysis were conclusive in determining the quality of the wires. The wires maintained uniformity throughout different sections.

4.1.1 Powder Characterization

Metal alloying powders added to the wire core consisted of pure, atomized aluminum, silicon, copper and chromium. The powders were analyzed qualitatively for size and powder size using a light optical microscope. Figure 4.1 shows the images of the four alloying powders used in the powder core of the wire. Aluminum exhibits a globular morphology with a relatively uniform distribution with regards to size and shape. Silicon has an irregular shape with a dark non-reflective finish. Particles are relatively uniform in size. Copper powder is very small and granular in shape. Large shards of copper are present in the powders and must be extracted by powder sieving prior to addition in the metal core. Chromium displays a globular shape as well as a highly reflective finish.

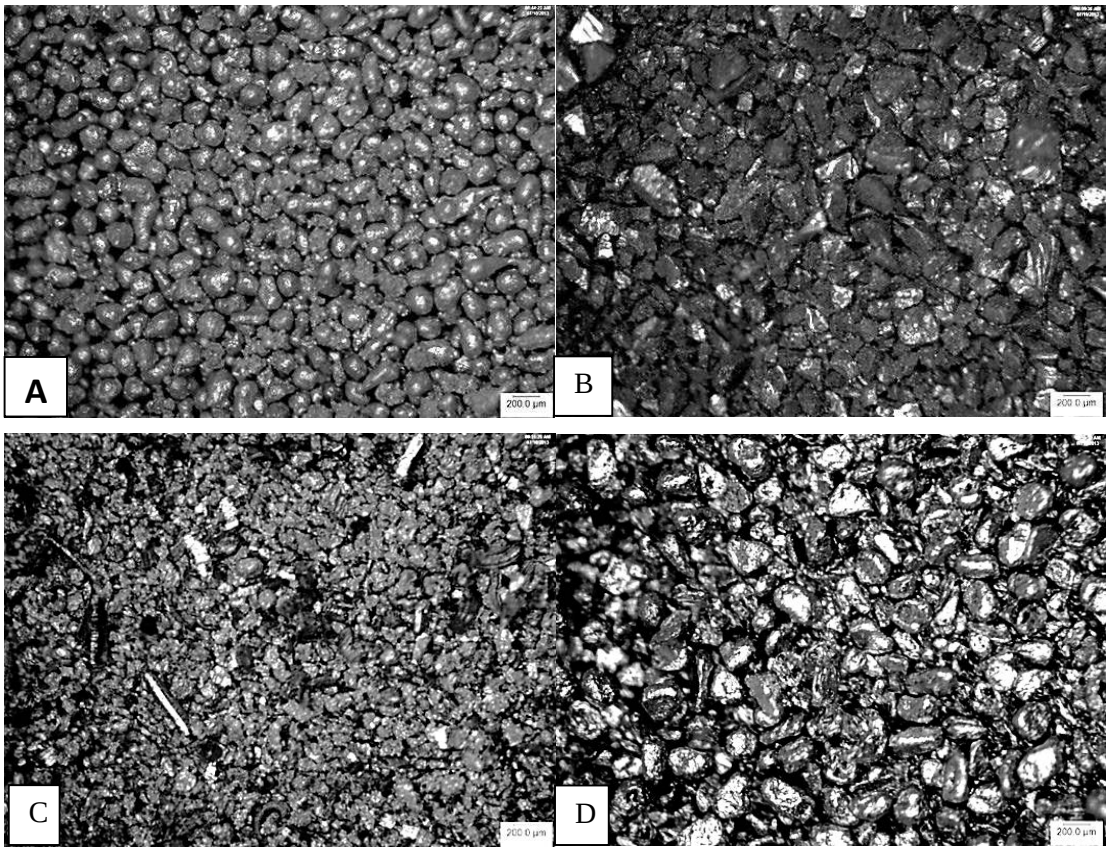

Figure 4.1 Light optical images of A) aluminum, B) silicon, C) copper, and D) chromium powders showing morphology and relative size distribution.

Uncoated silicon carbide was also examined for shape and powder characteristics using light optical microscopy. Figure 4.2 presents a light micrograph of the base silicon carbide that exhibits a sharply faceted morphology. Particles are reflective and prone to static charging and agglomeration. Particles were sieved to +44 microns to reduce small particles that are more prone to charging prior to addition in the powder core. SEM micrographs of the coated powders, represented in Figure 4.3, show the coverage of the nickel and copper coatings on the silicon carbide. High amounts of copper and nickel coating fully encase the silicon carbide particles. Particles with high nickel content, although maintained complete coverage, exhibited pores in the coating. Particles with a high copper content displayed nodules of copper forming on the surface. These surface irregularities also increased the surface area. Particles with low copper coating did not exhibit complete coverage of the coating. However, low nickel content coated silicon carbide particles did show full coverage as well as small nodules of nickel on the surface. This large increase of surface area increases the potential for contaminates such as organics, oxides, and

debris to be introduced into the wire and the deposits.

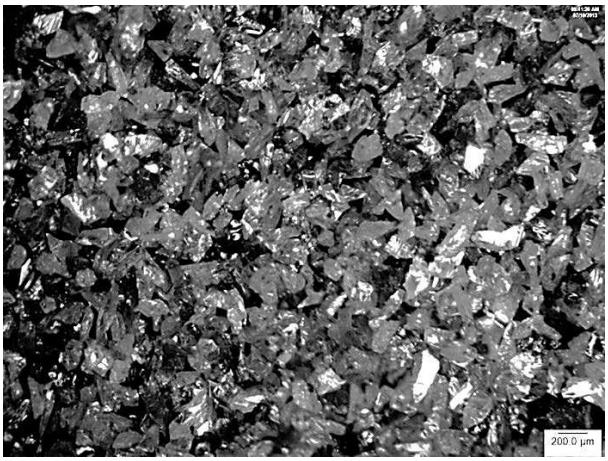

Figure 4.2 Light optical image of uncoated silicon carbide powder, showing the faceted morphology and relative uniform particle size.

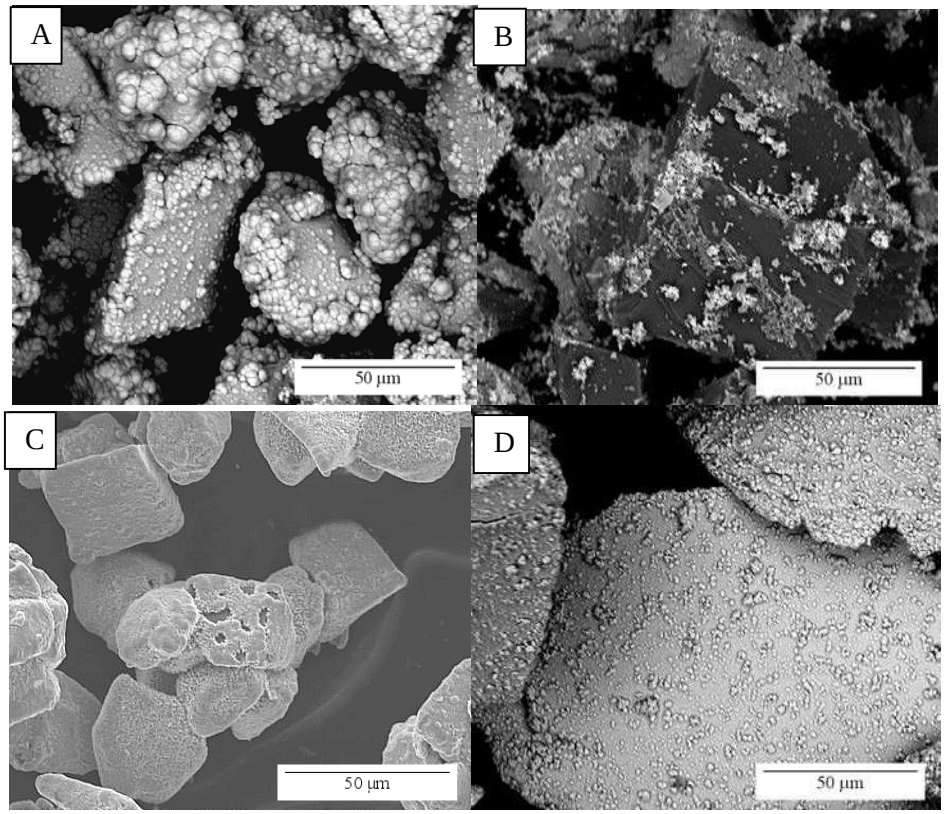

Figure 4.3 SEM images of A) high copper content (HCC), B) low copper content (LCC), C) high nickel content (HNC), and D) low nickel content (LNC) coated silicon carbide powders. Relative size distribution and coating quality can be compared.

Metal alloying powders as well as coated and uncoated silicon carbide powders were analyzed using the static laser light scattering system for determining particle size distribution. The data was reported as a histogram which gives the fraction of particles passing and fraction of particles channeled (retained) in a specific size range. This histogram was used to determine an average particle size and a size range for each type of powder added in the powder core. Figure 4.4 displays histogram data for the metal alloying powders. Aluminum powder incorporated into the wire had an average particle size of approximately 88.5 µm in diameter. Silicon had an average particle size of 105.2 µm, copper averaged at 64.3 µm, and chromium had an average diameter of 120.8 µm.

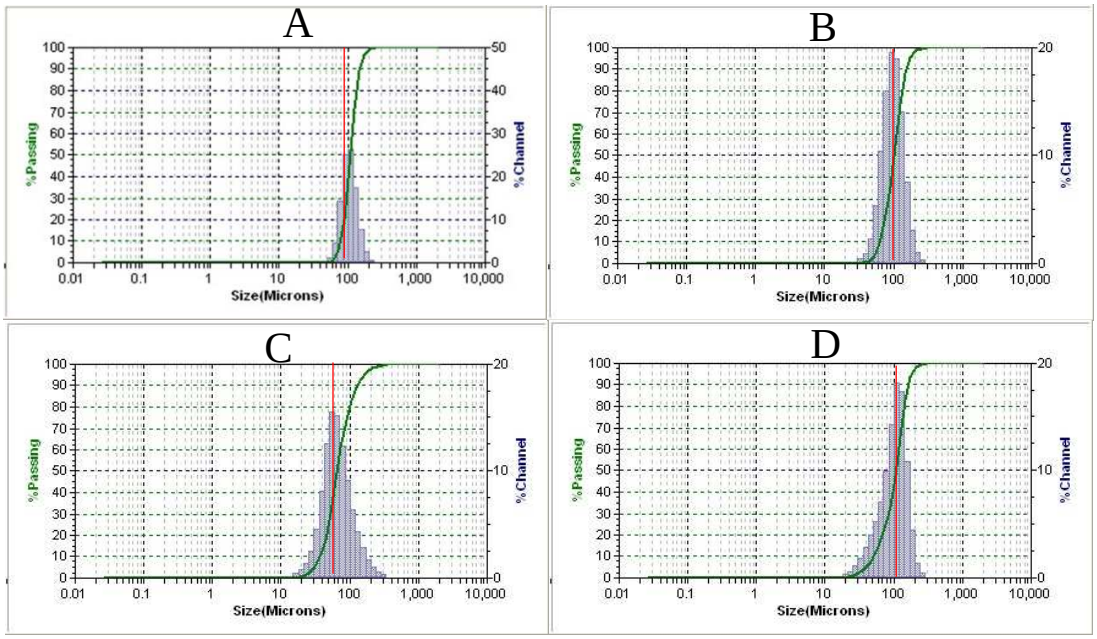

Figure 4.4 Particle size distribution histograms of A) aluminum, B) silicon, C) copper, and D) chromium powders analyzed by static laser light scattering.

Uncoated silicon carbide particles analyzed by laser light scattering had an average particle size of 55.5 µm. The particle size distribution histogram is given in Figure 4.5. Coated silicon carbide particles had a varied range of particle size given in various size distribution histograms in Figure 4.6. Silicon carbide particles with high copper content had an average diameter of 56.3 µm where low copper content coated silicon carbide averaged at 49.6 µm. Nickel coated silicon carbide powder varied greatly in size. High nickel content coated silicon carbide had an average diameter of 65.8 µm where low nickel content coated silicon carbide

averaged at 133.7 µm in diameter. This variation of particle size is due to the use of different grit silicon carbide particles prior to coating.

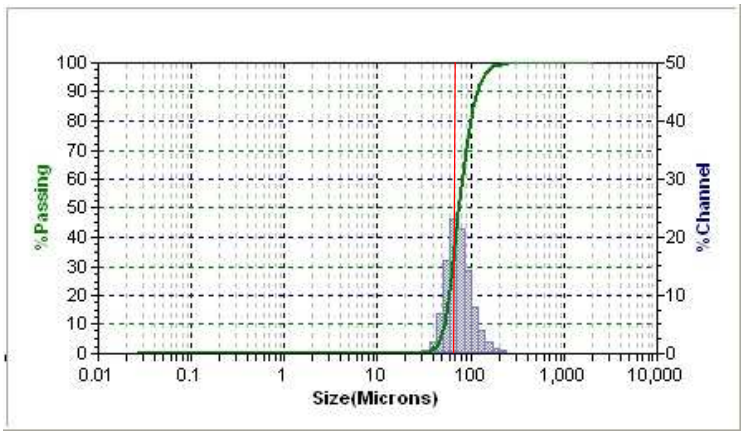

Figure 4.5 Particle size distribution histogram of uncoated silicon carbide powder analyzed by static laser light scattering.

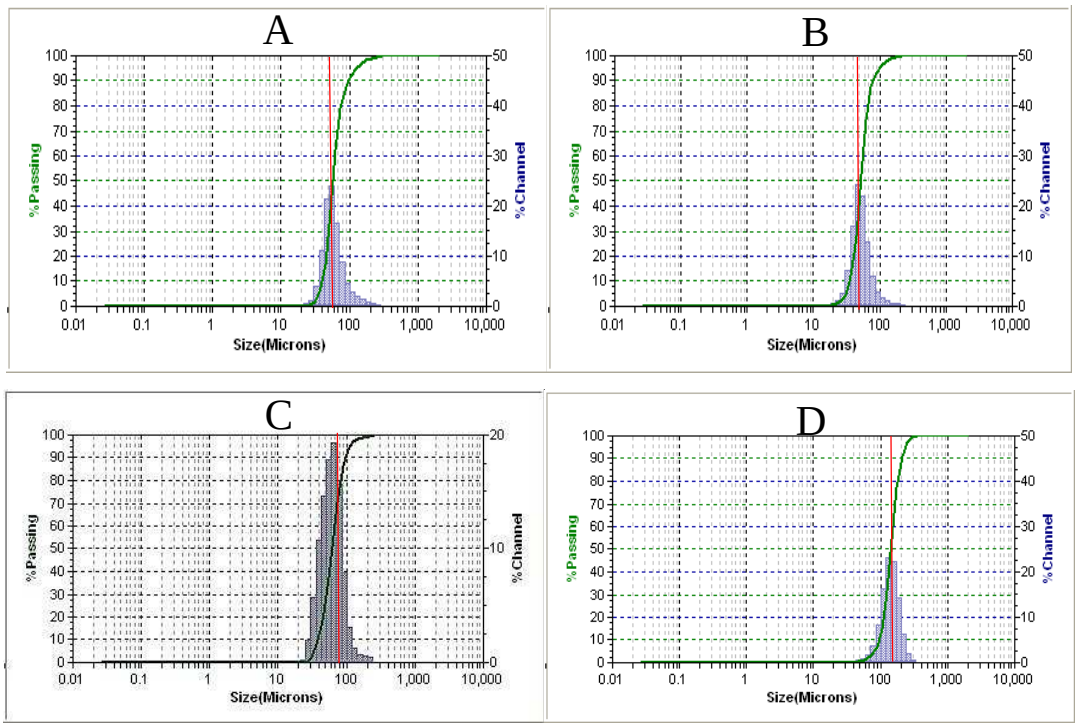

Figure 4.6 Particle size distribution histograms for A) high copper content (HCC), B) low copper content (LCC), C) high nickel content (HNC), and D) low nickel content (LNC) coated silicon carbide particles analyzed by static laser light scattering.

4.1.2 Wire Characterization

Each of the wires were analyzed using chemical and optical testing methods to determine consistency in the powder fill, dispersion and volume fraction of silicon carbide in the core as well as bulk composition of the wire. Consistency of the powder core was determined using longitudinal cross-section metallography.

Samples of each wire were analyzed using digestive ICP-OES analysis methods. A sample of Al 6061 alloy was analyzed and compared with both, spark ICP-OES results, as well as ASM specifications, to validate the digestive method and set a standard for further analysis to be conducted. Table 4.1 compares both ICP-OES techniques to specifications set by ASM International. All values by specifications are maximum allowable weight percentages of each alloying element. Each wire was analyzed using the digestive method for content in weight percentages of the same alloying elements. With the exception of silicon analysis is accurate to 100 ppm. Silicon content cannot be accurately measured using digestive ICP-OES due to interference from the fused silica crucible in which the analysis was conducted. Table 4.2 illustrates the comparison of composition for each of the five wires. Magnesium content was intentionally increased in the wires to account for vaporization loss during deposition. It was shown that copper was out of specification for all cases. Nickel content from the coating on the particles caused the wires to fall out of Al 6061 alloy specification. This occurrence was anticipated since nickel was used in these wires as a direct replacement for copper. Iron, manganese, chromium, and titanium were determined to be within the specifications of Al 6061 alloy. Results of this analysis were compared with compositional analysis results of depositions to determine modifications to the wire that are required to improve microstructure in future deposits.

Table 4.1 Comparison of analytical methods to material specifications.

Sample	Mg (wt. %)	Fe	Si	Cu	Ni	Mn	Cr	Ti	Analysis
6061	0.8	0.22	0.3	0.19	0.006	0.051	0.054	0.02	Digestive ICP-OES
6061	0.85	0.24	0.63	0.22	-	0.06	0.06	0.02	Spark ICP-OES
6061	0.8-1.2	0.7	0.4-0.8	0.15-0.40	-	0.15	0.04-0.35	0.15	ASM-Specifications

Table 4.2 Comparison of composition for each of five iterations of metal matrix composite powder cored tubular wires.

Sample	Mg (wt. %)	Fe	Si	Cu	Ni	Mn	Cr	Ti
UC_Wire	2.1	0.18	[redacted]	0.12	0.0042	0.0065	0.2	0.012
HCC_Wire	2.1	0.18	[redacted]	0.52	0.0041	0.0065	0.19	0.0096
LCC_Wire	2.2	0.18	[redacted]	0.078	0.0042	0.0069	0.22	0.0098
HNC_Wire	2.1	0.18	[redacted]	0.022	0.67	0.0066	0.18	0.0087
LNC_Wire	2.0	0.17	[redacted]	0.021	0.35	0.0061	0.18	0.0087

Samples were taken from each of the five iterations of wire and were cross-sectioned longitudinally to expose the powder core. SEM analysis was used to determine the uniformity of distribution for the silicon carbide particles as well as the volume fraction of silicon carbide in the wires. Due to the rapid rate of the wire feed during deposition, reinforcement uniformity needs to be maintained only at the scale of millimeters to result in uniformity throughout a single layer deposit. Small variations in the powder core at any length less than one millimeter are negligible as factors for affecting the overall deposit. Figure 4.8 shows backscattered electron images which compare the longitudinal cross-sections of the five iterations of wires. The silicon carbide particles are shown as irregular dark particles. Copper and nickel coatings appear to be white in the images. Image analysis was conducted on the cross-sections, using color thresholding techniques, to measure the volume fraction of particles in the wire prior to deposition. It was determined that the volume fraction of silicon carbide is up to 83 percent less than the design volumes fraction, shown in Table 4.3. As such, the target volume fraction of silicon carbide was not being met prior to deposition. This difference could be due to powder loss during the mixing and drawing processes. Particles with a higher weight percent of coating are much denser than the bulk metal powder which may lead to powder segregation during mixing and feeding into the wire. Other modes of powder loss were attributed to static charging of the particles making them adhere to surfaces during powder feeding, removing them from the bulk powder. Adjustments to the powder mixture must be made in future wire iterations to accommodate the differences observed. The full analysis of wires is given in Appendix A.

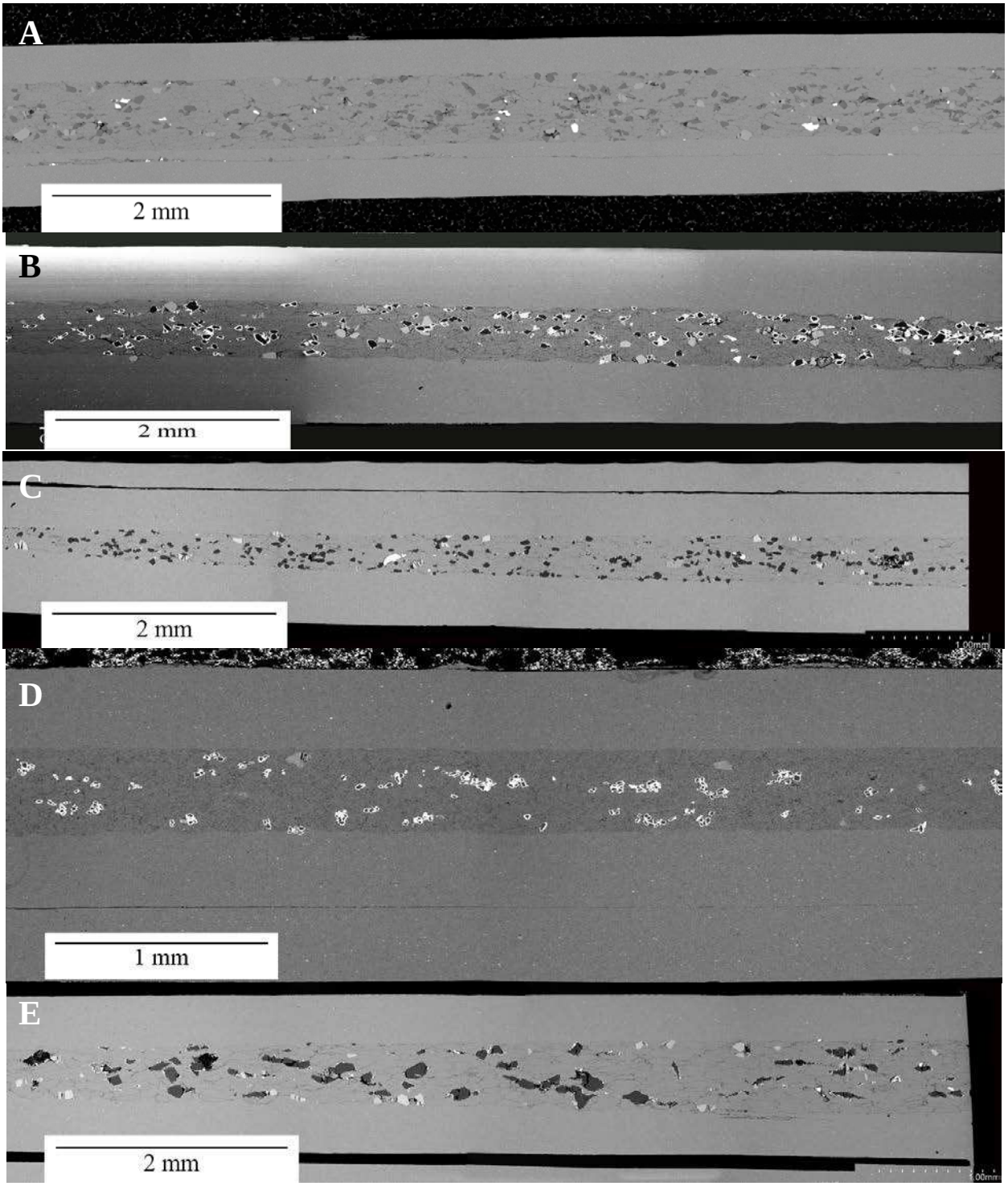

Figure 4.7 Logitudinal cross-sections of A) uncoated, B) high copper coated, C) low copper coated, D) high nickel coated, E) low nickel coated silicon carbide particle containing wires.

Table 4.3 Comparison of volume fraction measurements in the five iterations of wire.

Wire Sample	Volume Fraction of SiC (%)	Target Volume Fraction of SiC (%)
UC	3.41	10.00
HCC	1.79	
LCC	2.29	
HNC	1.70	
LNC	4.13	

4.2 Effect of Coating Conditions on Deposit Quality

Data was collected from analyzing single and multiple layer deposits containing the five different reinforcement coating conditions. Deposits were examined for uniformity of the microstructure across subsequent layers, amount of aluminum carbide formation, particle dispersion, and for target composition of the aluminum matrix and volume fraction of silicon carbide. Compositional analysis showed that vaporization loss of magnesium during deposition was greater than predicted. With the exception of copper and silicon most other alloying elements remained within specifications for Al 6061 alloy. The collected data was compared between the various deposits to determine how great of an effect the particle coatings had on meeting the desired criteria. Cross-sectional analysis of the multilayer deposits showed that there was an overall even distribution of interdendritic phases. Columnar grain growth was observed primarily in the fusion zone of the deposits as well as inter-pass fusion zones in some cases. Solidification cracking was observed in deposits containing uncoated silicon carbide and the high coating content conditions. Crack healing was observed in deposits containing lower coating content. The presence of aluminum carbide in the regions of clusters was qualitatively measured relative to the amount of clusters present. Analysis showed that nickel coated particles were less susceptible to forming aluminum carbide. Thermodynamic calculations supporting the observations are shown in Section 4.4. The volume fraction of silicon carbide present in the deposits was affected by the amount of coating. The trend shown in the wire was also observed in the deposits; the volume fraction of silicon carbide is lower with higher coating content. Mean

free path measurements for the clusters in the matrix of the deposits showed that dispersion of silicon carbide is higher in deposits containing either uncoated or a low coating content of nickel or copper. Fluid mechanics modelling of dispersion is presented in Section 4.5. The full experimental analysis and results are presented in Sections 4.2.1 and 4.2.2.

4.2.1 Build Characterization and Matrix microstructural Analysis

Compositional analysis was performed using digestive ICP-OES techniques. Two 100 mg samples were extracted from the focused rastered beam condition of multiple layer deposits for each of the five material conditions. The analysis of Al 6061 alloy base material, shown in Table 4.1, was used as a standard and compared with the results of each sample. The results given in Table 4.4 show the percentage by weight of seven alloying elements present in each deposition. It was noted earlier that silicon cannot be accurately measured due to interference of the crucible during analysis. It was determined that magnesium exhibited a 75-80 wt. % loss during deposition. Two mechanisms can be attributed to the observed loss. One, magnesium has a relatively vapor pressure and is highly susceptible to vaporization in a vacuum environment. Two, the sheath material can have a tendency to unravel at the lap joint during deposition. When the lap joint was not properly sealed or was not stress relieved during the baking step, it might unravel and not deposit into the melt properly. Since magnesium in the melt will come solely from the sheath, any sections of deposition made with unraveled wire would lose considerable amounts of magnesium in addition to vaporization loss. Copper additions varied greatly between samples of different coating conditions. For all but one sample, the copper content was not in specification for the Al 6061 alloy. It was shown that the result of low copper content, or replacing copper with nickel addition, the deposits also had a lower susceptibility to solidification cracking. Results of this analysis can be used to adjust the amount of powder additions for the development of future metal matrix composite consumable wires.

Scanning electron microscopy images of each multilayer deposit showed the effect of silicon carbide particulates on the microstructure of the deposit. A macroscale image was taken of each multilayer deposit shown in Table 4.5. Each deposit was then analyzed at higher magnifications to characterize the particle/matrix bond, secondary phases, the formation of aluminum carbide, and the retained volume fraction of silicon carbide in the matrix. The microstructural analysis for each of the five material conditions are compared below. All five samples shown in detail were deposited using a focused rastered (F_0) electron beam. The full microstructural analysis for all

material and beam conditions is presented in Appendix B.

Table 4.4 Compositional analysis of metal matrix composite depositions.

Sample	Mg (wt. %)	Fe	Si	Cu	Ni	Mn	Cr	Ti	Crack Susceptability
7_UC_Trial 1	0.48	0.18		0.14	0.0037	0.0073	0.19	0.013	Crack
7_UC_Trial 2	0.44	0.19		0.13	0.0037	0.0069	0.2	0.013	
6_HCC_Trial 1	0.53	0.2		0.46	0.0043	0.0092	0.22	0.011	Crack
6_HCC_Trial 2	0.53	0.19		0.22	0.0038	0.0086	0.22	0.011	
6_LCC_Trial 1	0.47	0.19		0.14	0.0033	0.0084	0.23	0.012	No Crack
6_LCC_Trial 2	0.5	0.19		0.14	0.0031	0.0087	0.23	0.012	
6_HNC_Trial 1	0.52	0.2		0.036	0.39	0.01	0.19	0.01	No Crack
6_HNC_Trial 2	0.54	0.19		0.038	0.39	0.0096	0.19	0.011	
6_LNC_Trial 1	0.46	0.19		0.04	0.31	0.0086	0.19	0.011	No Crack
6_LNC_Trial 2	0.44	0.19		0.036	0.3	0.0093	0.2	0.011	

All deposits showed clustering of silicon carbide particles. Deposits containing uncoated silicon carbide particles developed clusters with features highly detrimental to the overall microstructure shown in Figure 4.8. The clusters consisted of silicon carbide particles trapped in partially melted aluminum particles. At the boundary of the aluminum particles, aluminum oxide was detected which appeared to block the aluminum particles from completely fusing. This behavior creates clusters that can act as initiation points for solidification cracking and a path of least resistance for crack propagation. Figure 4.8b shows a highly magnified image of a cluster. The presence of aluminum carbide was detected in the vicinity of the cluster.

Depositions containing silicon carbide coated with high copper content showed an improvement in bonding between the matrix and reinforcement particles shown in Figure 4.9. The copper coating completely dissolved and formed intermetallic phases with silicon and aluminum which backfilled any separated particles. Aluminum carbide formation still remained present in copper coated deposits. Solidification cracking was observed in deposits with near regions with a high copper content. Figure 4.9b shows a deposit with high copper content. The high magnification image shows the large increase of copper-rich inter dendritic phases in the vicinity of the silicon carbide cluster.

Table 4.5 Comparison of macroscopic images for each of the various material and beam conditions.

Beam Condition	Uncoated (UC)	High Copper Content (HCC)	Low Copper Content (LCC)	High Nickel Content (HNC)	Low Nickel Content (LNC)
F_0	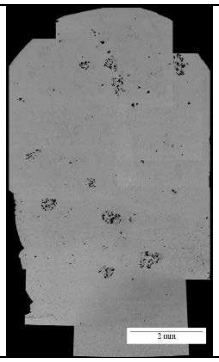	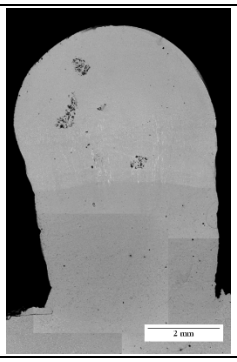	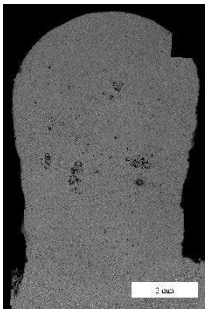	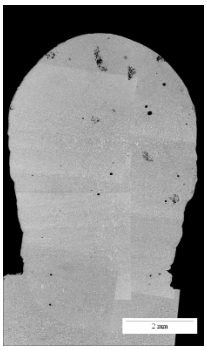	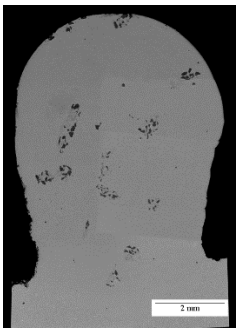
$F_{0.25f}$		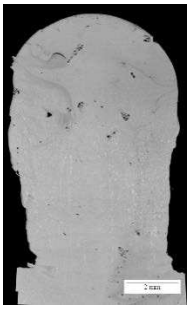	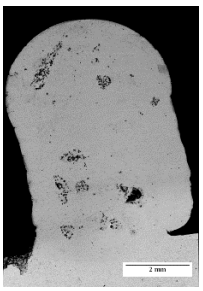	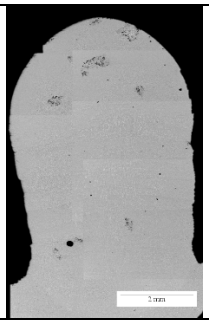	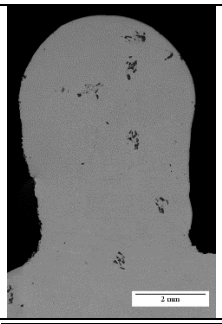
F_f	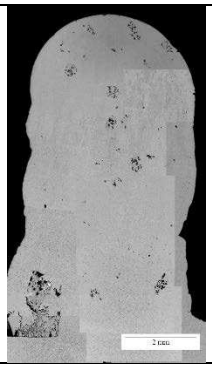	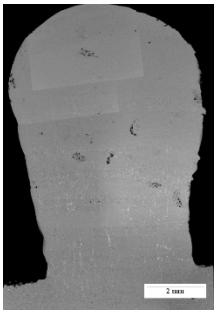	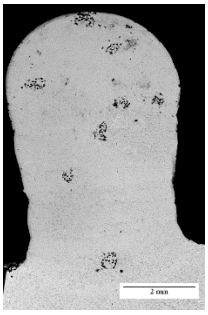	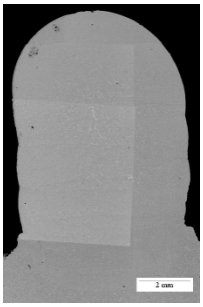	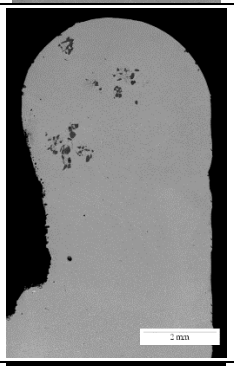
D_0	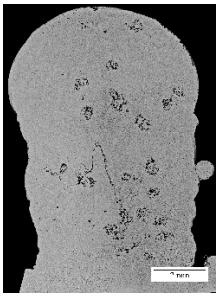		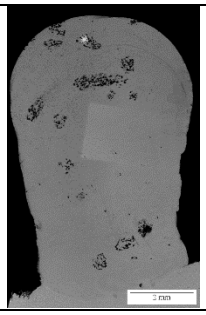		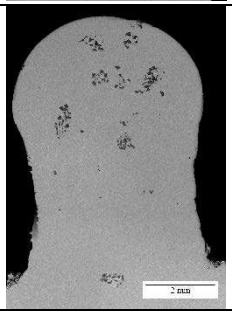

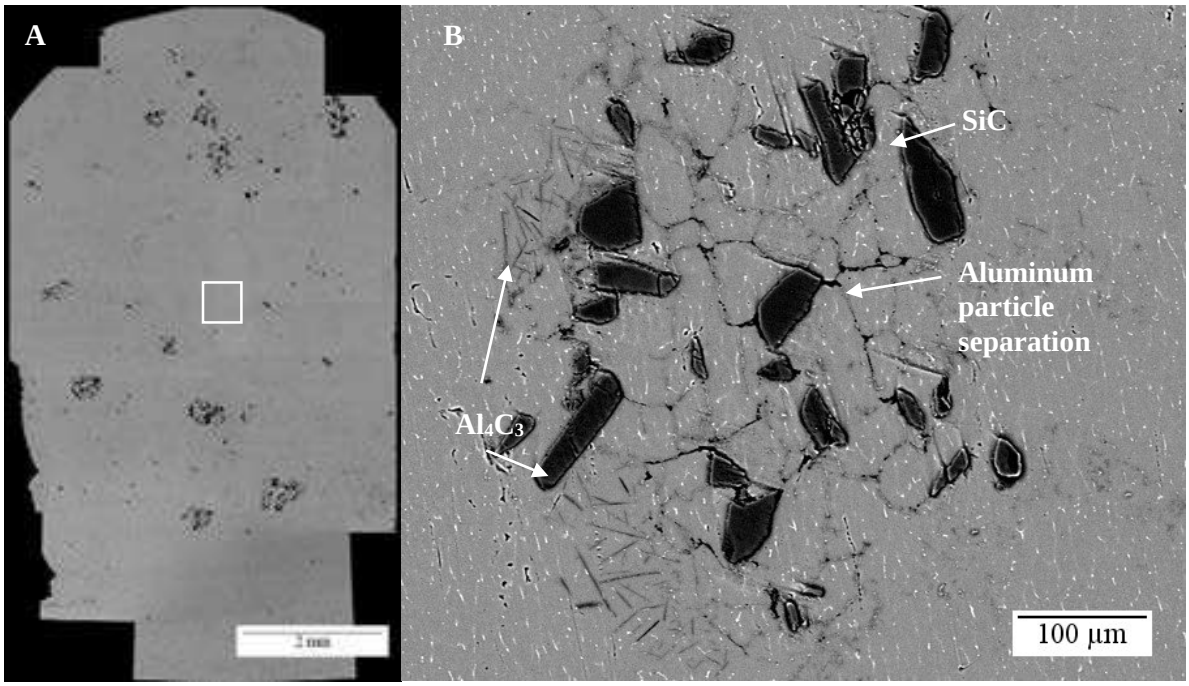

Figure 4.8 A) Macroscopic cross-section of uncoated SiC containing deposit using a focused rastered electron beam. B) High magnification of a silicon carbide cluster showing particle separation and aluminum carbide formation.

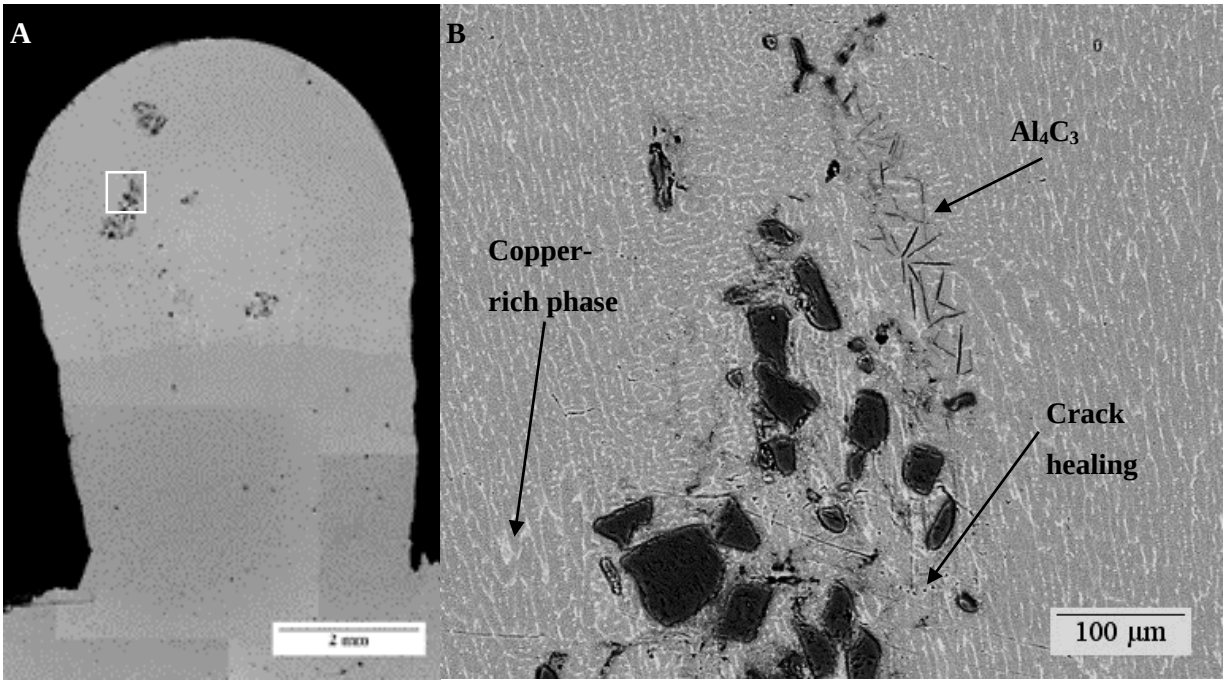

Figure 4.9 A) Macroscopic image of a deposit with high copper content made using a focused rastered beam. B) High magnification image of a cluster in the matrix showing high amounts of intermetallic compounds as well as the presence of aluminum carbide.

Deposits containing a lower content of copper (Figure 4.10) behaved similarly to deposits containing uncoated silicon carbide. Clusters exhibited insufficient fusion between the metal powders and aluminum carbide remained present in the vicinity of the clusters. However, the deposits did not show signs of solidification cracking. Due to the lack of copper, intermetallic compound formation was greatly reduced. The overall microstructure in the matrix remained uniform overall compared to the intermetallic compound gradients seen in the deposits containing high copper content. Figure 4.10b illustrates the characteristics of the microstructure for the low copper content containing deposits.

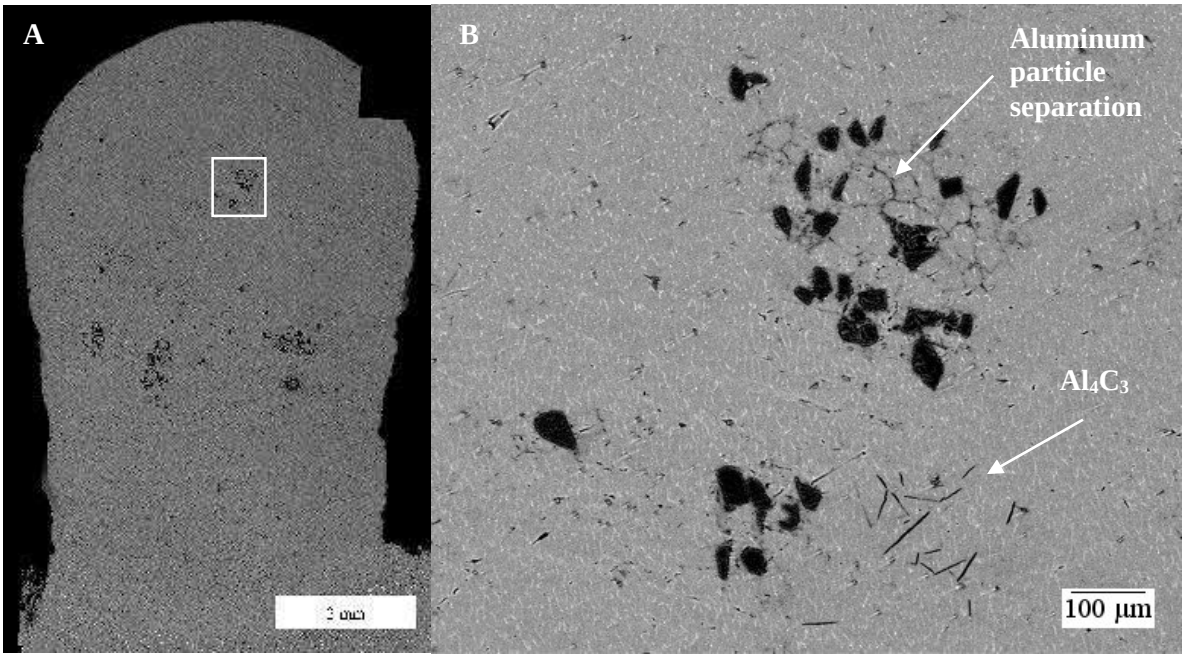

Figure 4.10 A) Macroscopic image of a deposit with low copper content made using a focused rastered beam. B) High magnification image of clusters in the matrix showing low amounts of intermetallic compounds as well as the presence of aluminum carbide.

The deposits containing silicon carbide with high nickel content (Figure 4.11) developed a microstructure very similar to that of deposits with high copper content. The clusters are surrounded by completely melted aluminum rather than partially melted powder. The microstructure also exhibited no solidification cracking or aluminum carbide formation. Figure 4.11b shows the microstructure of a deposit made with high nickel content.

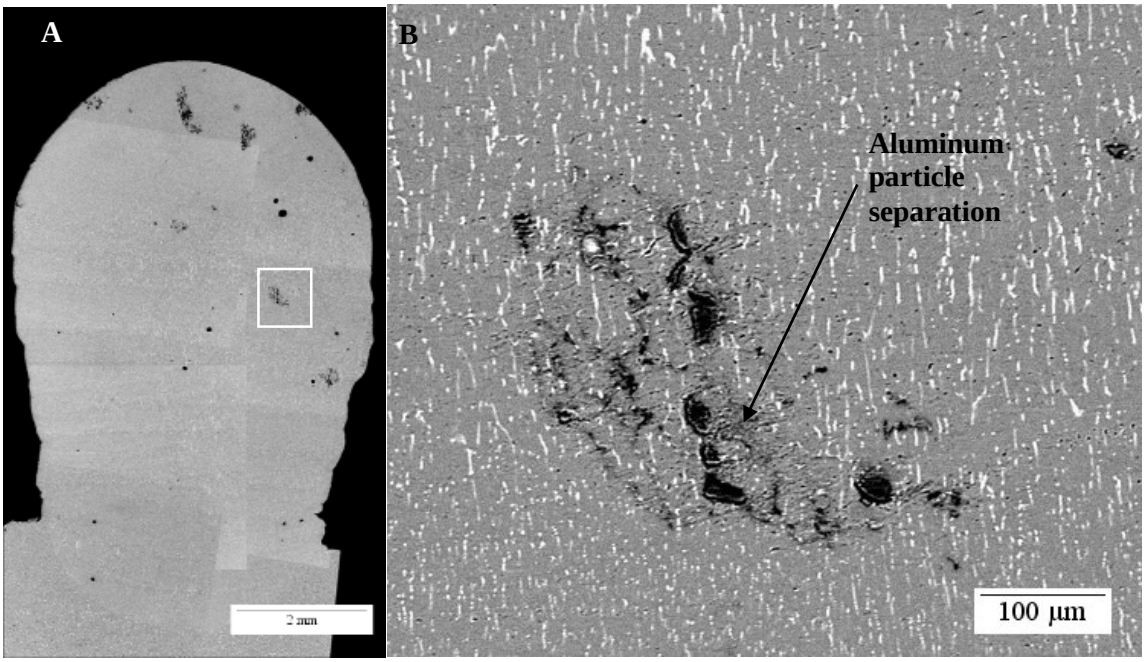

Figure 4.11 A) Macroscopic image of a deposit with high nickel content made using a focused rastered beam. B) High magnification image of clusters in the matrix showing high amounts of intermetallic compounds with no presence aluminum carbide.

The deposits containing low amounts of nickel (Figure 4.12) behaved in the same manner as deposits with low copper content, however, no aluminum carbide was detected in the matrix. Figure 4.12b demonstrates the similarities the low nickel content deposits share with the low copper and high nickel containing deposits.

The amount of aluminum carbide present in each deposit was quantified as a percentage of silicon carbide clusters containing aluminum carbide from the total number of clusters present in the cross-section. This data was used to draw a comparison to determine the effect coatings have in mitigating aluminum carbide formation. Figure 4.13 demonstrates this comparison between the different coating conditions at mitigating aluminum carbide formation. It is clearly shown that increasing the copper content in the deposits increases the amount of aluminum carbide present in the matrix. It was also shown that increasing nickel content effectively eliminates aluminum carbide in the deposit.

The volume fraction of silicon carbide was also analyzed in the matrix. Threshold tools in image analysis software were used to measure the volume fraction of silicon carbide particles retained in the matrix. Figure 4.14 compares average values of the volume fraction of silicon carbide for different coating conditions. Values are given in percentages. It was determined that

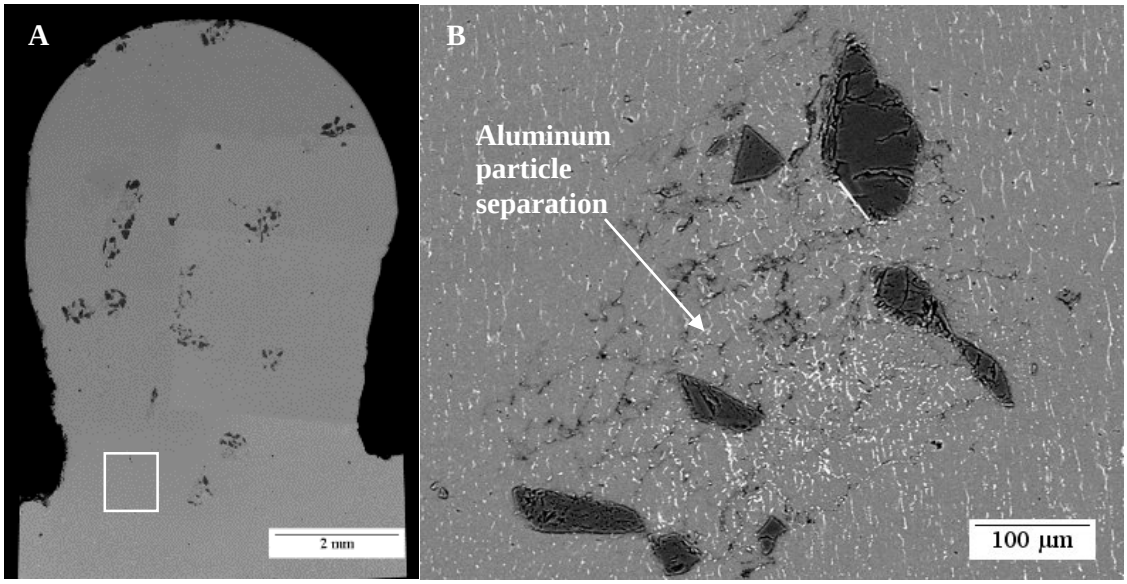

Figure 4.12 A) Macroscopic image of a deposit with low nickel content made using a focused rastered beam. B) High magnification image of clusters in the matrix showing low amounts of intermetallic compounds with no presence aluminum carbide.

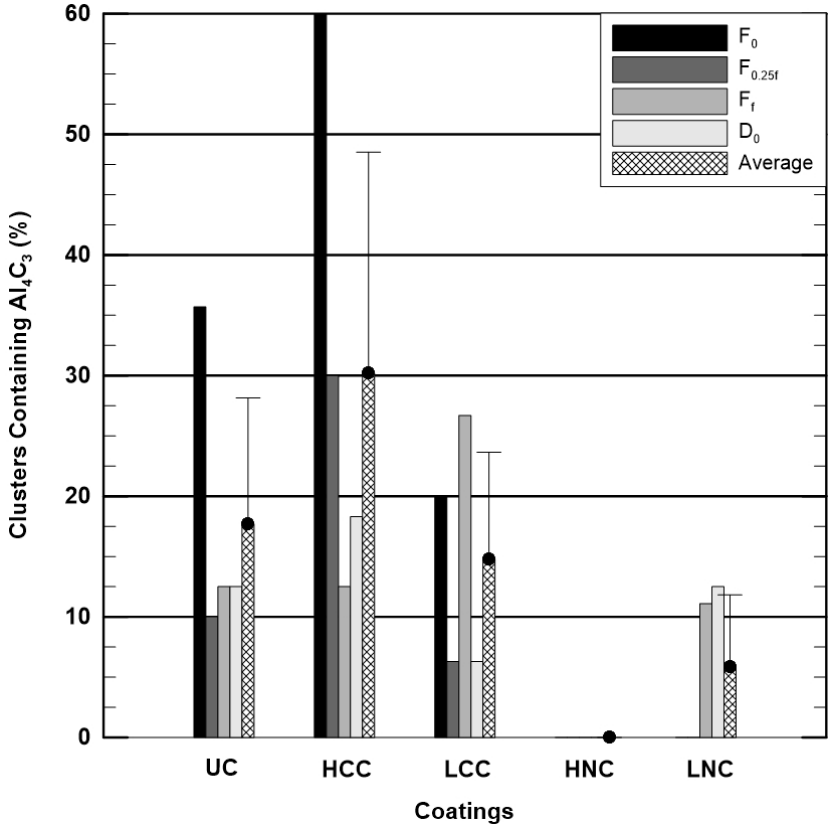

Figure 4.13 Comparison of coatings and the effect they have on mitigating aluminum carbide formation.

deposits with a higher content of nickel or copper coating retain a lower volume fraction of particles. This trend also relates to the decrease in volume fraction of coated silicon carbide particles in the wire cross-section. It is determined that the higher amounts of copper and nickel drastically increase the density of the particles. This leads to segregation of the silicon carbide particles during powder mixing therefore less is incorporated into the wire used in deposition. Appendix B provides tables of values collected for all of the charts given for deposit characterization.

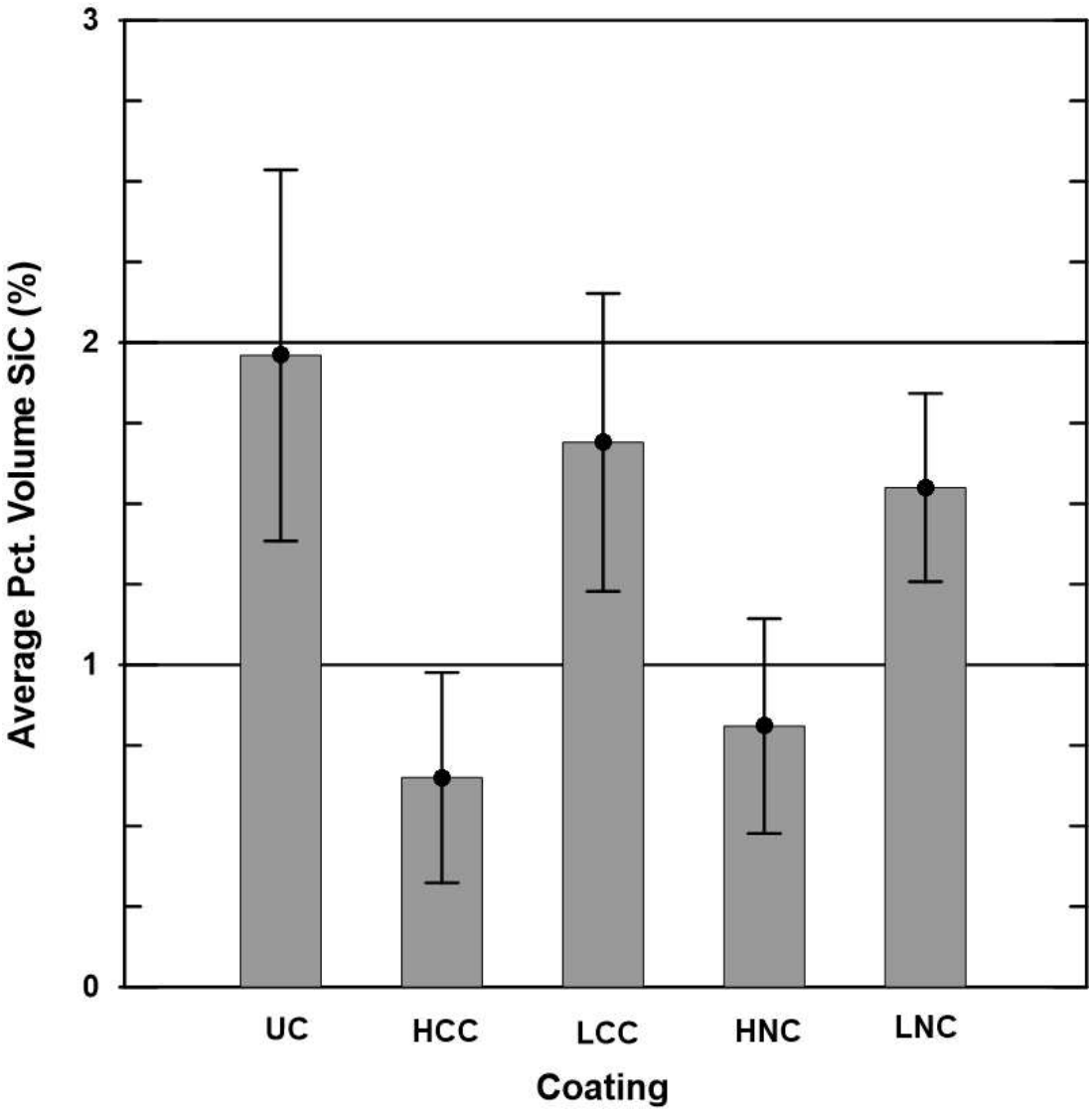

Figure 4.14 Comparison of average volume percent of silicon carbide retained in the matrix between different coating conditions.

4.2.2 Particle Dispersion

Particle analysis was conducted on each of the deposition cross-sections to calculate a relative mean free path and determine the effect of coating type has on dispersing silicon carbide in an aluminum matrix. Clusters of silicon carbide were treated as single particles. In some cases, dispersed particles and very small clusters were detected in the matrix. Using FIJI image analysis software, the cross sectional area of each cluster, or particle, was measured. An overall count of clusters was made for a given volume of matrix. The mean free path, i.e. the nearest neighbor distance, in mm, for a given cluster was calculated by inputting these values in Equation 9, where A is given as the area of the cluster and n_v is the number of clusters per given volume. The mean free path for each cluster was calculated; the overall mean free path for the deposit was determined by averaging the values for each of the clusters. The cluster area and mean free path measurements were normalized by volume fraction of silicon carbide in the deposit since these vary significantly between different builds. Figure 4.15 plots mean free path as a function of cluster size for each of the five coating conditions. Values residing in Quadrant I indicate that deposits have relatively small cluster size, a sign of increased dispersion, but a high mean free path, which indicates a low volume percent of silicon carbide. The more favorable values follow the direction of the arrow in Quadrant III. These values indicate a high volume fraction of dispersed particles. Values in Quadrants II and IV indicate large amounts of agglomeration and are highly unfavorable.

The data in Figure 4.15 indicates that low copper content (LCC), and low nickel content (LNC) coated conditions provide the highest amount of dispersion in the matrix. Silicon carbide particles with high copper and nickel content can be ruled out as feasible coating conditions to enhance dispersion. Due to the thick coating and high melting temperatures, along with thermal gradients generated by transitions of material, it is likely that the high coating content solidifies too rapidly trapping the particles in large clusters.

Comparing the data collected from microstructural and particle dispersion measurements, it was determined that low amounts of nickel coating facilitates the fabrication of the best overall deposits.

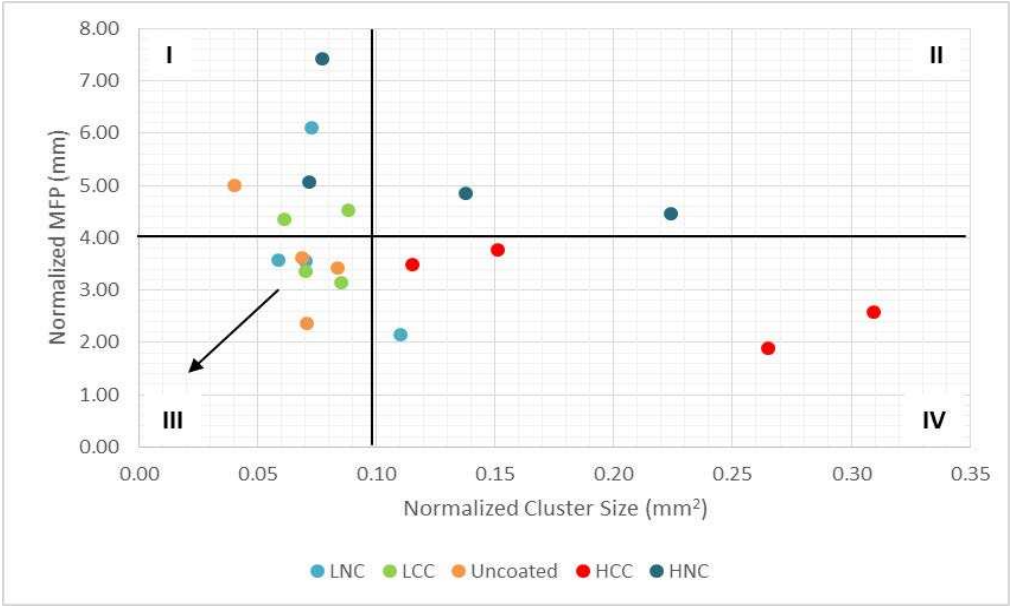

Figure 4.15 Plot comparing normalized mean free path and cluster size values for the five coating conditions. Dispersion increases in the direction of the arrow.

4.3 Effect of Process Parameters on Deposit Quality

Deposits were analyzed to determine the effect of beam conditions on overall deposit quality. As described in the Experimental Procedures section, beam spot size (focused or defocused), motion, and pulse frequency were varied; four sets of beam conditions were used in the experimental matrix. Three focused rastered beam conditions were studied. The pulsing conditions were set at zero (F_0), low frequency ($F_{0.25f}$) and high frequency (F_f). The fourth condition studied was a defocused beam with no beam motion or pulsing (D_0). Several other variations to the parameters were studied and included in Appendix B. Deposits were examined for uniformity in the microstructure, the amount of aluminum carbide formation, particle dispersion and volume fraction of silicon carbide and defects such as solidification cracking. Particle coatings have a much greater effect on the matrix than beam parameters. Single layer deposits were cross-sectioned and analyzed to determine the effect of beam parameters on deposit geometry. It was determined that variations in deposit geometry measurements can be up to an 18 pct. difference which is discussed further in Section 4.3.1. It was also shown that using a defocused beam increases the volume fraction of the silicon carbide trapped in the matrix and reduces the amount of aluminum carbide formation. Solidification cracking was found to be controlled more by material variations rather than deposition conditions. Mean free path

measurements taken to quantify particle dispersion revealed that greater dispersion resulted in deposits made using a non-pulsed electron beam. Sections 4.3.1 and 4.3.2 present the experimental analysis and collected data to validate these observations.

4.3.1 Build Characterization and Matrix microstructural Analysis

Microstructural analysis was performed on the various deposits, comparing characteristics with respect to the parameters of the electron beam used for deposition. Deposit geometry was studied and compared for the four beam conditions by collecting height, depth and width measurements of the single layer deposits. Four beam conditions were examined to determine the effect on aluminum carbide formation and retained silicon carbide in the matrix. Figure 4.16 compares the amount of aluminum carbide formation as a fraction of the amount of silicon carbide clusters containing aluminum carbide to the total number of clusters in the matrix. This ratio is compared as a function of beam conditions. The results show that the defocused beam condition has the least amount of variability as well as one of the lowest average percentages of aluminum carbide formation. The focused rastered beam with no pulse showed the highest variability as well as the largest amount of aluminum carbide formation in the matrix. This behavior is most likely due to the high intensity of the focused beam combined with the uninterrupted contact with the melt pool. Direct interaction of SiC with the electron beam causes the particle to shatter instead of melt because of the low electrical conductivity of silicon carbide.

It was speculated that varying degrees of agitation in the melt pool as well as silicon carbide interaction with the beam may cause significant differences in the amount of retained silicon carbide. Figure 4.17 shows the result of this study. These values are averages of multiple measurements of volume percentage for different beam conditions. Again, the defocused beam provides the most favorable condition for retaining silicon carbide in the matrix. The lower intensity of the beam has less of an effect when put in contact with a silicon carbide particle, therefore particles are less likely to be ejected during deposition.

Single layer deposits were compared to determine which beam conditions result in the most ideal deposit morphology. Table 4.6 gives cross-sectional examples of all single layer deposits compared. Each cross-section was examined using image analysis software. The deposit width, depth of penetration and overfill height were measured. These dimensions were averaged

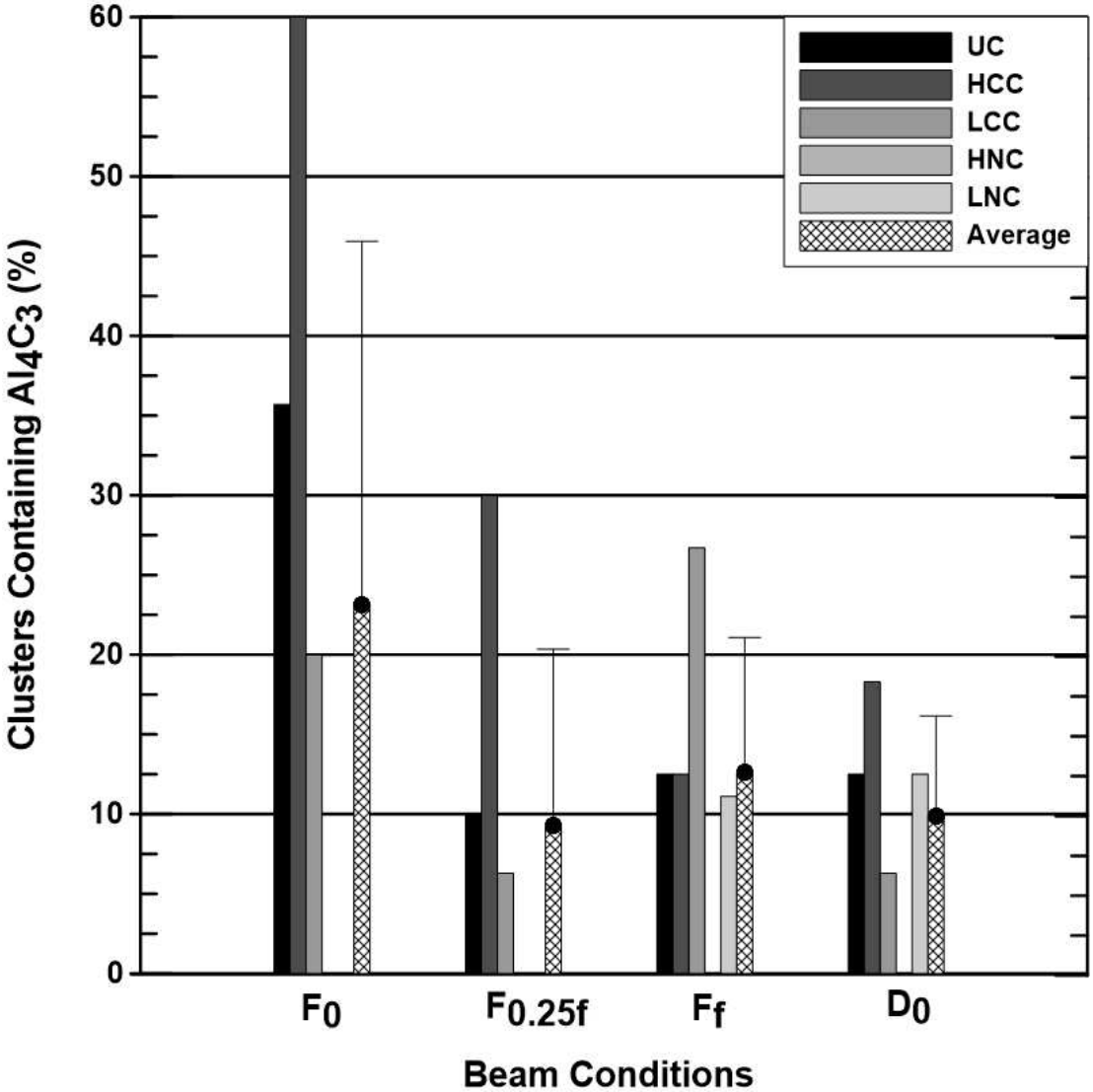

Figure 4.16 Comparison of aluminum carbide formation as a function of beam conditions for each of the deposits.

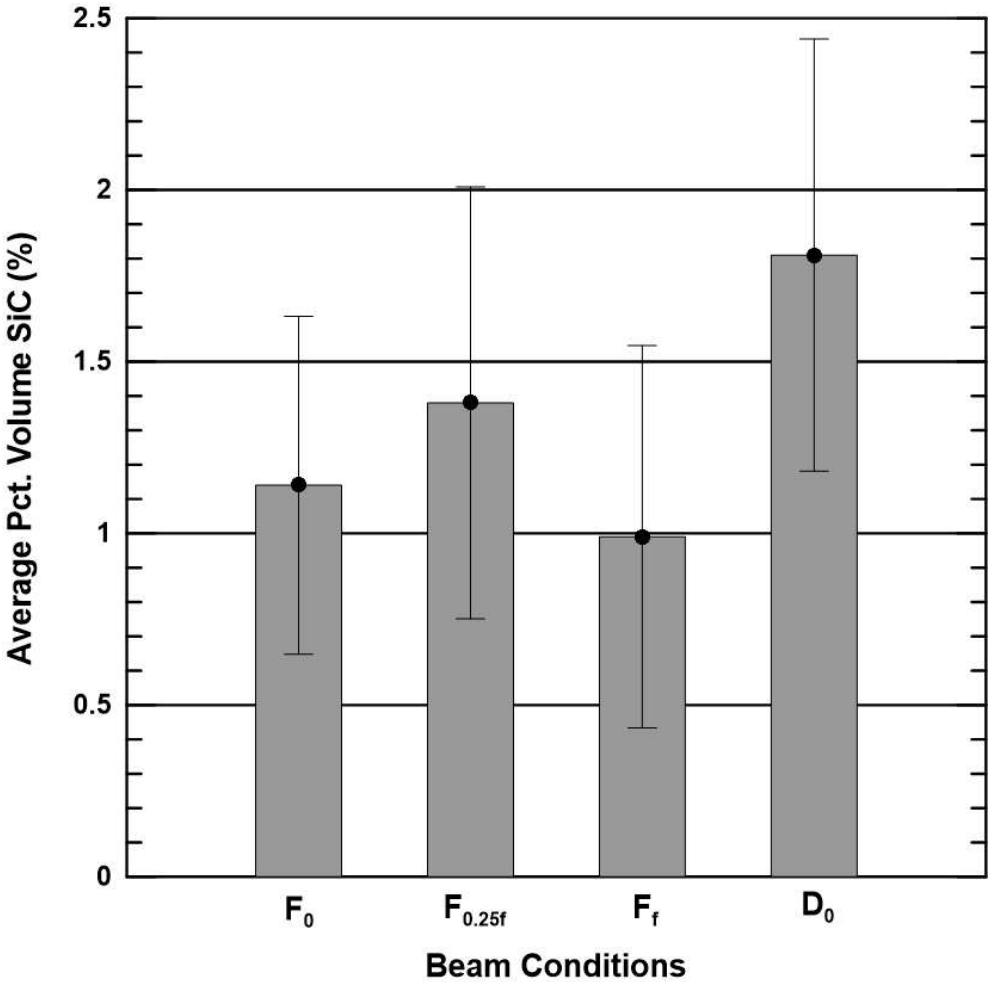

Figure 4.17 A comparison of average volume fraction of silicon carbide in the matrix as a function of beam conditions.

and compared as a function of beam conditions. The defocused beam condition produced single layer deposits which had the shortest width and depth of penetration while having the greatest height as shown in Figure 4.18. This condition would be the most efficient for deposition of structures such as stiffeners. The single layer deposit characterization, including all values in data tables, is located in Appendix C.

4.3.2 Particle Dispersion

Cluster area and mean free path calculations were conducted for silicon carbide suspended in the matrix with respect to beam conditions. The same methodology was followed as in previous calculations with respect to coating conditions. Figure 4.19 shows the data for

Table 4.6 Comparison of single layer deposit cross-sections.

Beam Condition	Uncoated (UC)	High Copper Content (HCC)	Low Copper Content (LCC)	High Nickel Content (HNC)	Low Nickel Content (LNC)
F_0		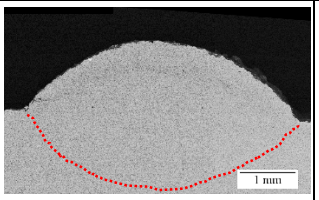	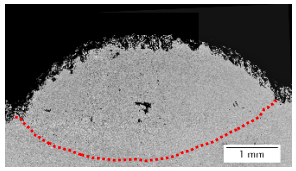	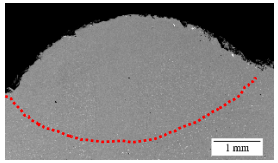	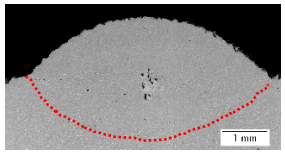
$F_{0.25f}$	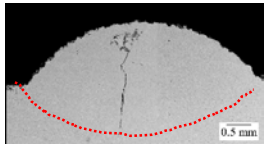	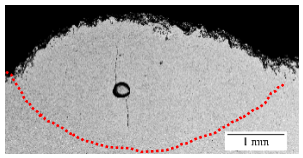	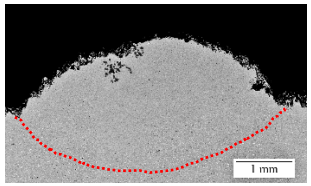	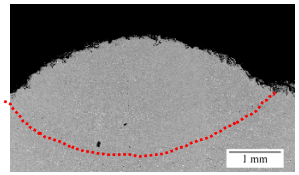	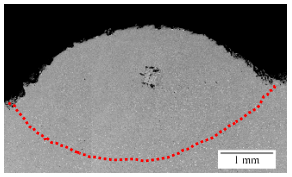
F_f	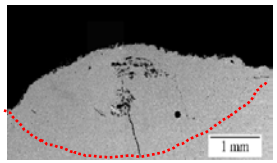	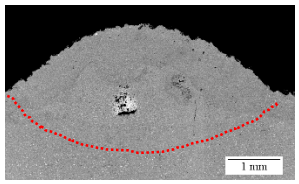	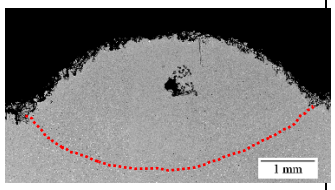	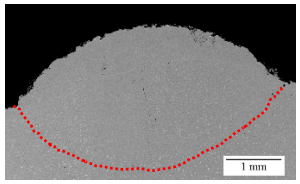	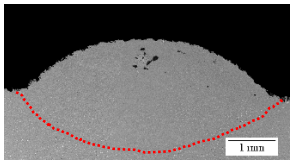
D_0		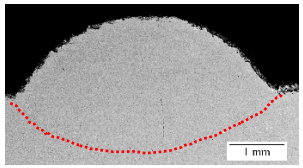	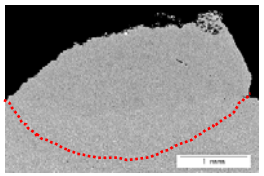	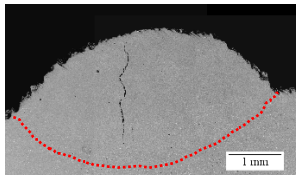	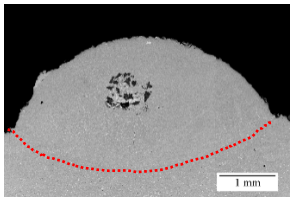

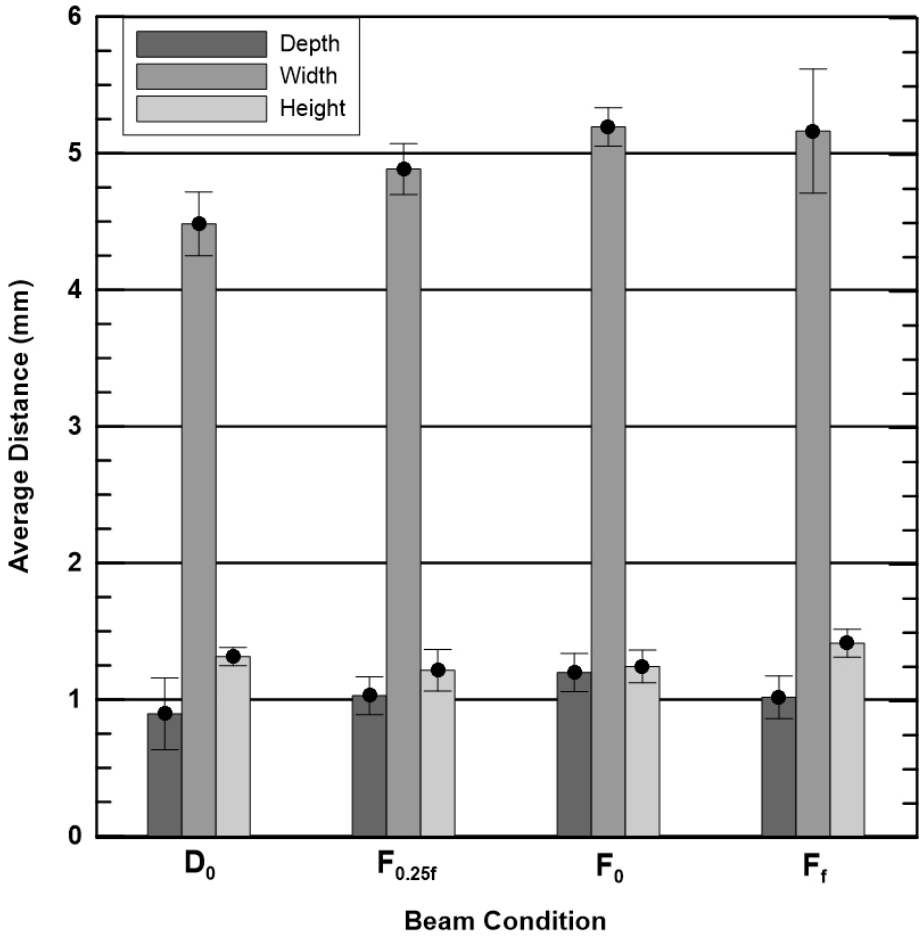

Figure 4.18 The effect of beam conditions on single layer deposit morphology.

normalized cluster area and mean free path for each of the four coating conditions. Again, the greatest favorability for dispersion in the matrix is indicated by the direction of the arrow. The data shows that the highest degree of dispersion was generally exhibited in samples deposited by a defocused beam, followed by a non-pulsed focused beam. It is not completely understood why pulsed conditions do not improve dispersion. One theory is that the pulsing conditions create more convective flow in the melt pool. This increase in convective flow would increase the ability for particles to move throughout the matrix and come in contact with one another, at which point they would more likely agglomerate. Results of this data recommend that further depositions of aluminum – silicon carbide metal matrix composites should implement a non-pulsed beam to promote dispersion. Confirmation that beam pulsing actually occurred at the set frequencies should be determined using an oscilloscope before any further pursuit of using pulsed electron beam conditions for the deposition of metal matrix composites. Based on the

initial data collected, pulsing conditions used were not suitable for enhancing dispersion. It is recommended that ultrasonic pulsing should be explored, matching the resonance of the particles, if pulsing is desired to accommodate particle dispersion.

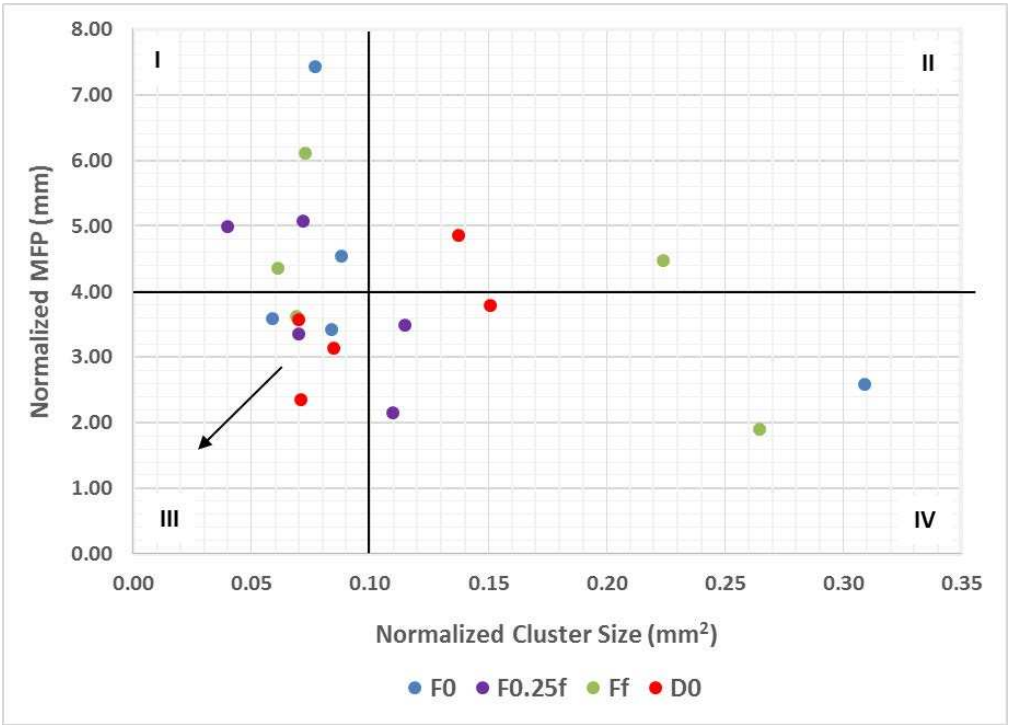

Figure 4.19 Plot comparing normalized mean free path and cluster size values for the four beam conditions. Increased dispersion in the direction of the arrow.

4.4 Computational Thermodynamic Modeling

Computational thermodynamic models were used to determine the propensity for phases to form and to determine if aluminum carbide formation can be eliminated from the matrix. All phase diagrams and reactions were developed under equilibrium heating and cooling conditions. Due to the rapid solidification of the EBF[3] process, high temperature calculations were considered to interpret what microstructures are present upon solidification. Since limited physical property this metal matrix composite was found in the literature, data must be extrapolated for certain values in the models. The average composition for 6061 aluminum alloy was used as a baseline for these models. To simplify the models only major alloying elements were considered when calculations were performed for this system. The composition was given as , 1.0 wt. % Mg – 0.6 wt. % Si – 0.25 wt. % Cu – 0.7 wt. % Fe, balance Al. Secondary phases and precipitates such as Mg_2Si, $Al_{12}Fe_3Si$, $Al_7Cu_3Mg_6$, and $Al_3Cu_2Mg_9Si_7$ were included in the computation for

comparison with literature data [47], [48]. The results of these calculations were used to determine the potential phases to form under optimal deposition conditions. Note that the calculations did not take into consideration the magnesium loss observed in actual deposits

4.4.1 Thermo-Calc Software Calculations

Thermo-Calc is a software package which uses data from various compiled thermodynamic property databases to calculate and produce diagrams such as Scheil-Gulliver solidification models, binary and ternary phase diagrams and other equilibrium thermodynamic data. Thermo-Calc was used to create i) pseudo-binary phase diagrams for the metal matrix, ii) ternary isothermal sections for phase transformations near the particle boundary, and iii) Scheil-Gulliver simulations to determine the favorability for aluminum carbide to form in the matrix. These results were interpreted to predict what reactions and phase transformations will occur under non-equilibrium conditions. The results were then compared with data and observations from depositions to gain a better understanding of the system.

Pseudo-binary phase diagrams were developed for 6061 aluminum alloy. The model was simplified to include only aluminum, magnesium, silicon, and copper in the calculations. Al - 0.6 wt. % Si – 0.25 wt. % with Mg varying between 0.0 and 3.0 wt. % was modeled. According to literature regarding 6061 aluminum alloy, Mg_2Si, Al_2Cu, and $Al_3Cu_2Mg_9Si_7$ are all likely to form during cooling. The phase diagram illustrated in Figure 4.21 predicts that this is likely to happen with approximately 1.0 wt. % Mg, which is the amount used in the 6061 system. This prediction verifies that the model is producing relatively accurate results. The powder cored tubular wires produced have a magnesium composition of approximately 2.0 wt. % Magnesium vaporization loss is approximately 75 pct., as determined by compositional analysis of the wire and deposits, which leaves 0.5 wt. % magnesium present in the as-solidified deposits. This excess loss as compared to the 50 wt. % loss initially predicted would change the as-solidified microstructure to resemble the 0.5 wt. % composition given by the model. The phase diagram with varying magnesium content can be used to verify changes in the microstructure due to vaporization loss as well as predict the composition for future wire iterations. A pseudo-binary phase diagram of the same composition, but rather varying silicon content was developed and given in Appendix D.

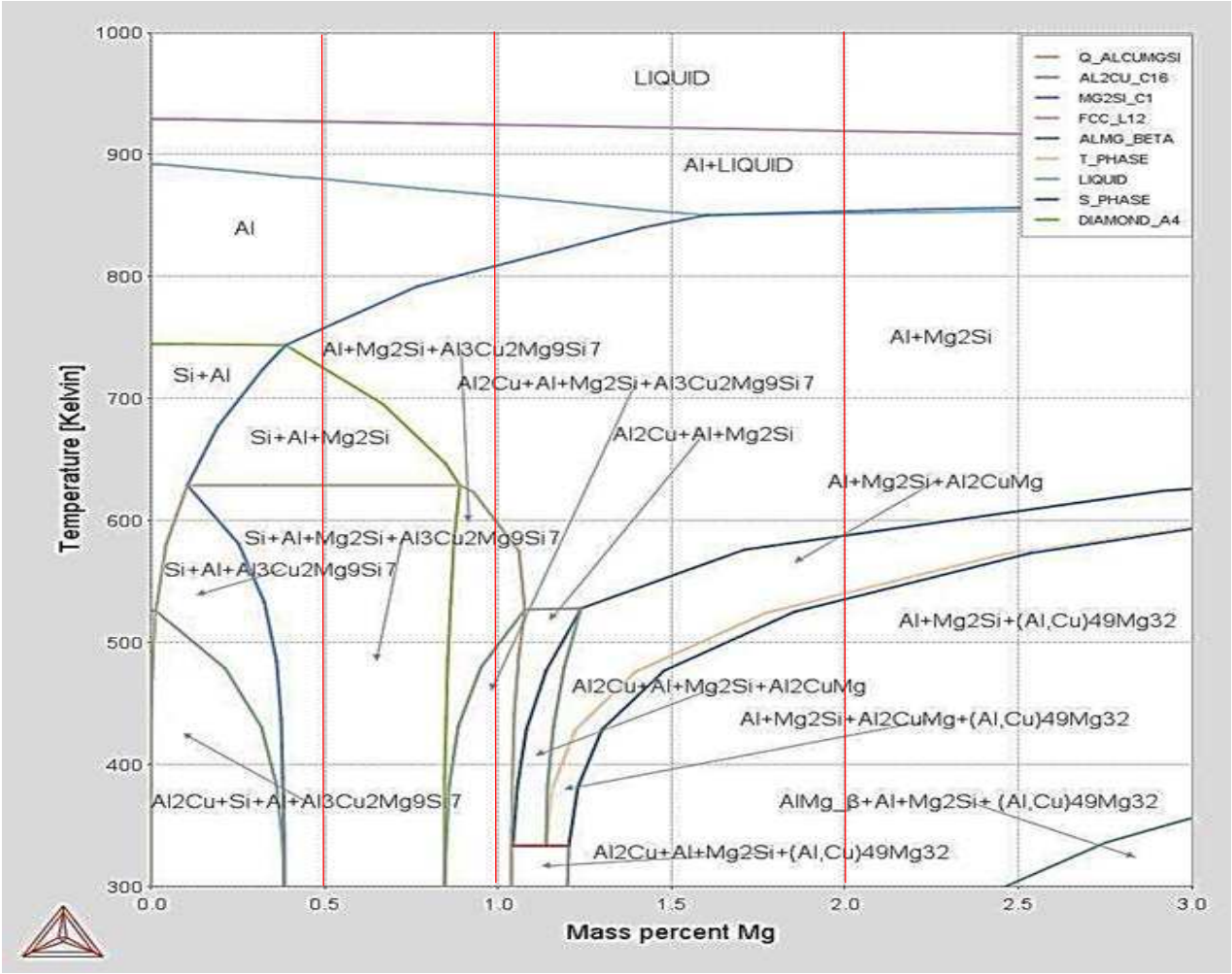

Figure 4.20 Pseudo-binary phase diagram of the Al 6061 alloy. Composition set at Al – 0.6 wt. % Si – 0.25 pct. wt. Cu with varying amounts of magnesium.

The Scheil-Gulliver model was used to create an equilibrium cooling diagram and to determine the mass fraction of phases to form in the solid upon normal cooling conditions [49]. The composition was set to Al – 1.0 wt. % Mg – 0.6 wt. % Si – 0.25 wt. % with the addition of 12.5 wt. % SiC in elemental form to simulate the target 10 vol. pct. desired in the final microstructure. The liquid was cooled from 2250 K (1977°C) to approximately 650 K (377°C), when the final liquid is solidified as illustrated in Figure 4.22. It was shown that the potential for aluminum carbide formation only occurs at temperatures above 1450 K (1177 °C). Since, melt pool temperatures can often reach values well above 1450 K, the presence of aluminum carbide can be expected. This calculation validates the importance of coating the particles to prevent this formation from occurring.

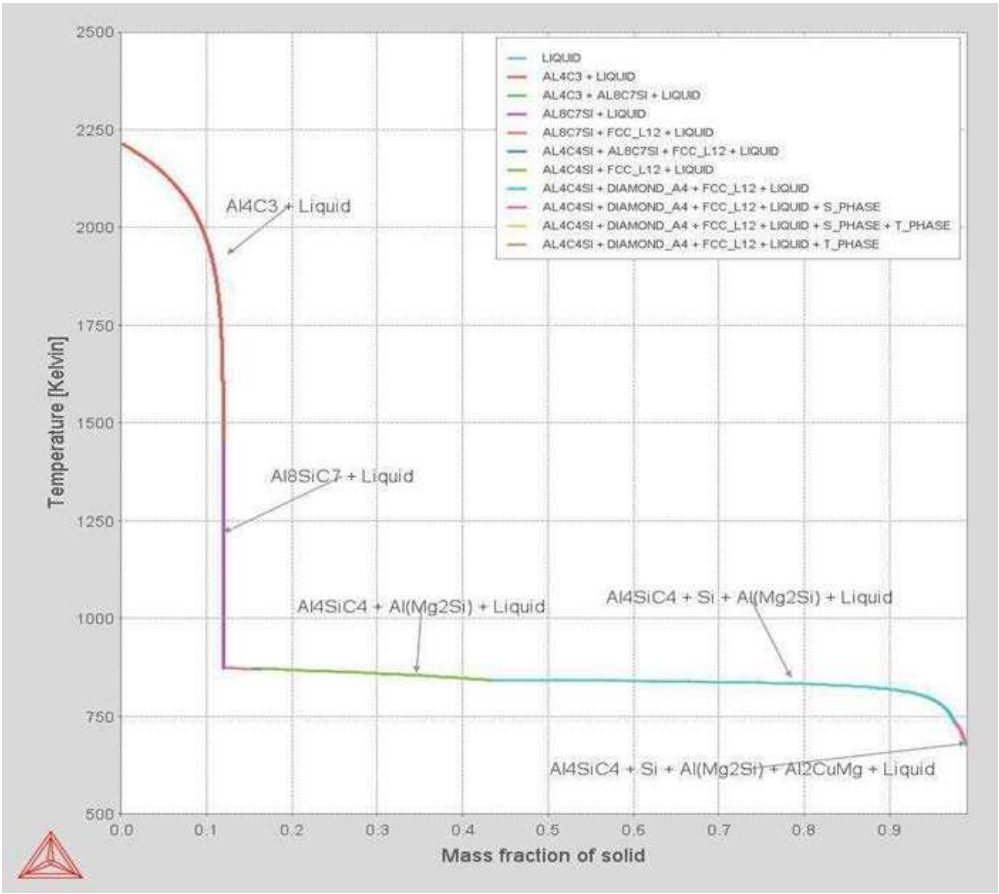

Figure 4.21 Scheil solidification model predicting phases in the Al 6061/SiC system under equilibrium cooling conditions.

Isothermal ternary phase diagrams were calculated to predict which phases would form in near the SiC particle-Al matrix interfacial region. Cu-Si-C and Ni-Si-C ternary systems were studied to determine if any other detrimental phases would form due to the addition of these coatings. Isotherms at 2700 K (2427°C), 1350K (1077°C), and 675 K (402°C) were developed for each of the ternary systems. Each isotherm contains a highlighted box estimating the regions of interest for analysis. Each component is given in elemental form, simulating the outcome if SiC had broken down to silicon and carbon elements. All phase diagrams are under equilibrium atmospheric and cooling conditions.

The Cu-Si-C system at 2700 K is given in Figure 4.23. At that temperature copper is liquid and silicon and carbon preferentially form silicon carbide. The 1350 K isotherm, Figure 4.24, shows that silicon will form along with liquid copper and silicon carbide. This temperature

is in the range of the melt pool during deposition. Due to the fast cooling rate of the process, it is likely that the phases formed at this temperature for the given composition range will dominate the final microstructure upon cooling. If the deposit is allowed to slow cool, the final microstructure will contain phases similar to that shown in Figure 4.25. These isothermal sections all indicate that copper is not likely to react with carbon. It is possible for a single intermetallic compound to form at low temperatures, however, copper does not seem to form any other detrimental phases when contacted with silicon carbide.

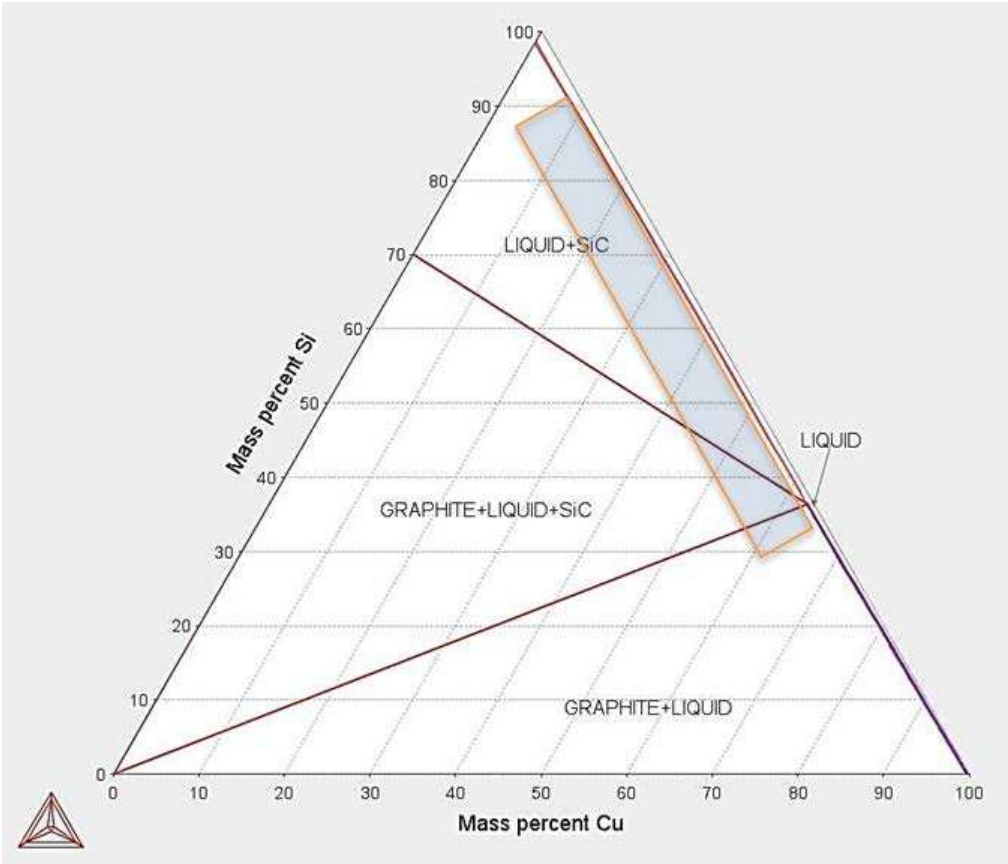

Figure 4.22 Cu-Si-C isothermal ternary phase diagram at 2700 K.

The Ni-Si-C system behaves similarly to the Cu-Si-C system since nickel also has little affinity for reacting with carbon. Figure 4.26 illustrates the reactions likely to occur at 2700 K. At this temperature nickel is liquid as well as silicon. High amounts of silicon will produce

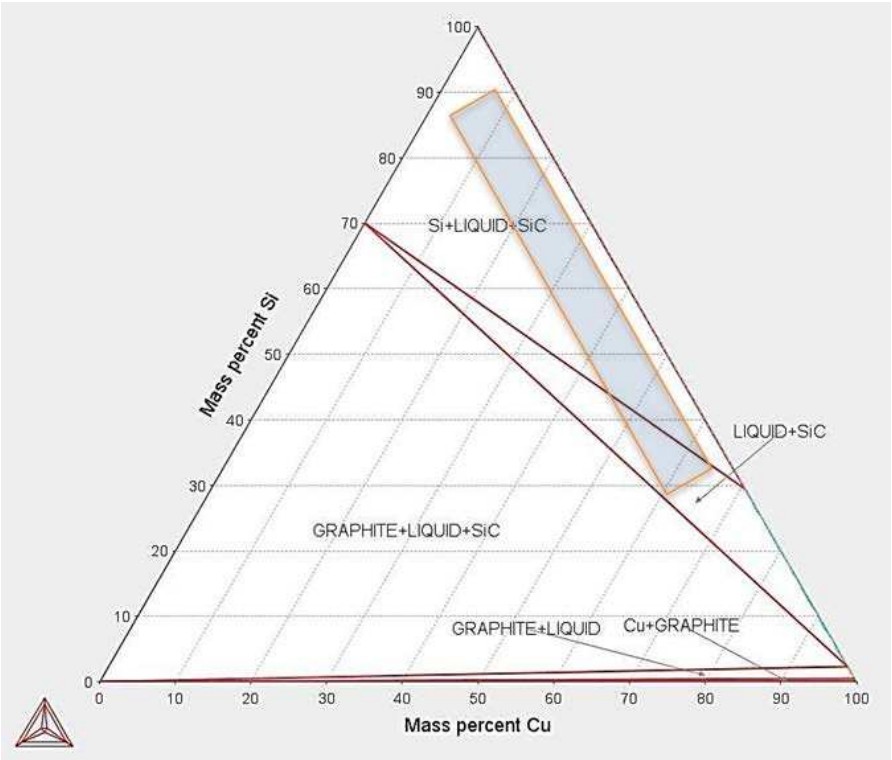

Figure 4.23 Cu-Si-C isothermal ternary phase diagram at 1350 K.

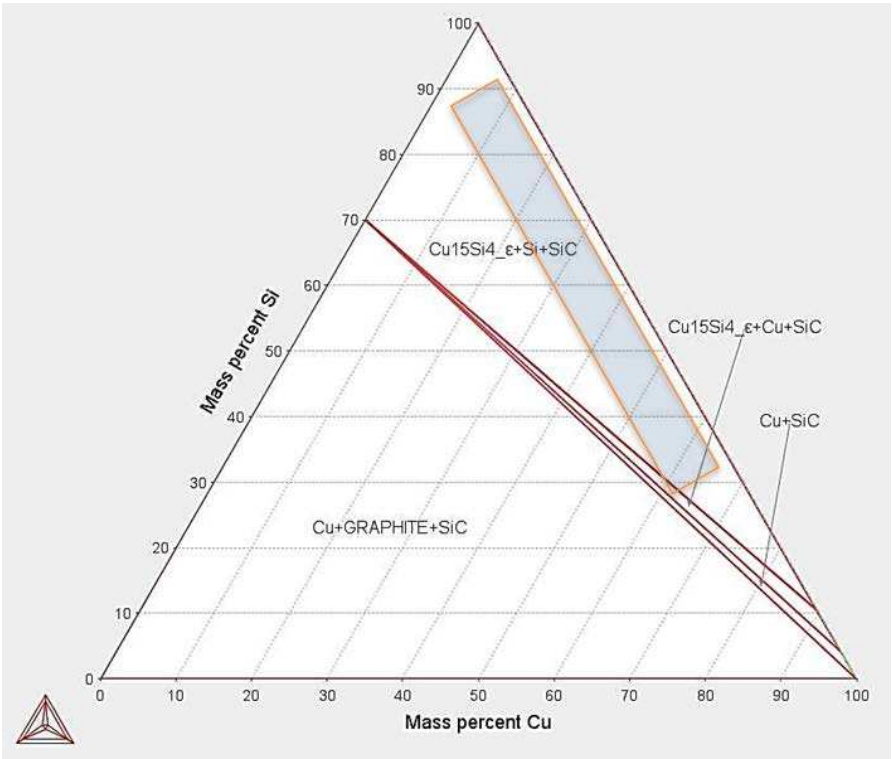

Figure 4.24 Cu-Si-C isothermal ternary phase diagram at 675 K.

silicon carbide, but carbon is also stable as graphite. At 1350 K, intermetallic compounds form in compositions with a high mass fraction of nickel in the matrix shown in Figure 4.27. The variability of intermetallic compound formation grows at 675 K demonstrated by Figure 4.28. High amounts of nickel may potentially destabilize silicon carbide and allow for aluminum carbide to form. However, the opposite was observed in EBF[3] deposits; high amounts of nickel completely eliminated the formation of aluminum carbide. Appendix D shows ternary phase diagrams for Cu-Al-Si and Ni-Al-C systems which expand the amount of predicted phases as a result of using copper or nickel coatings.

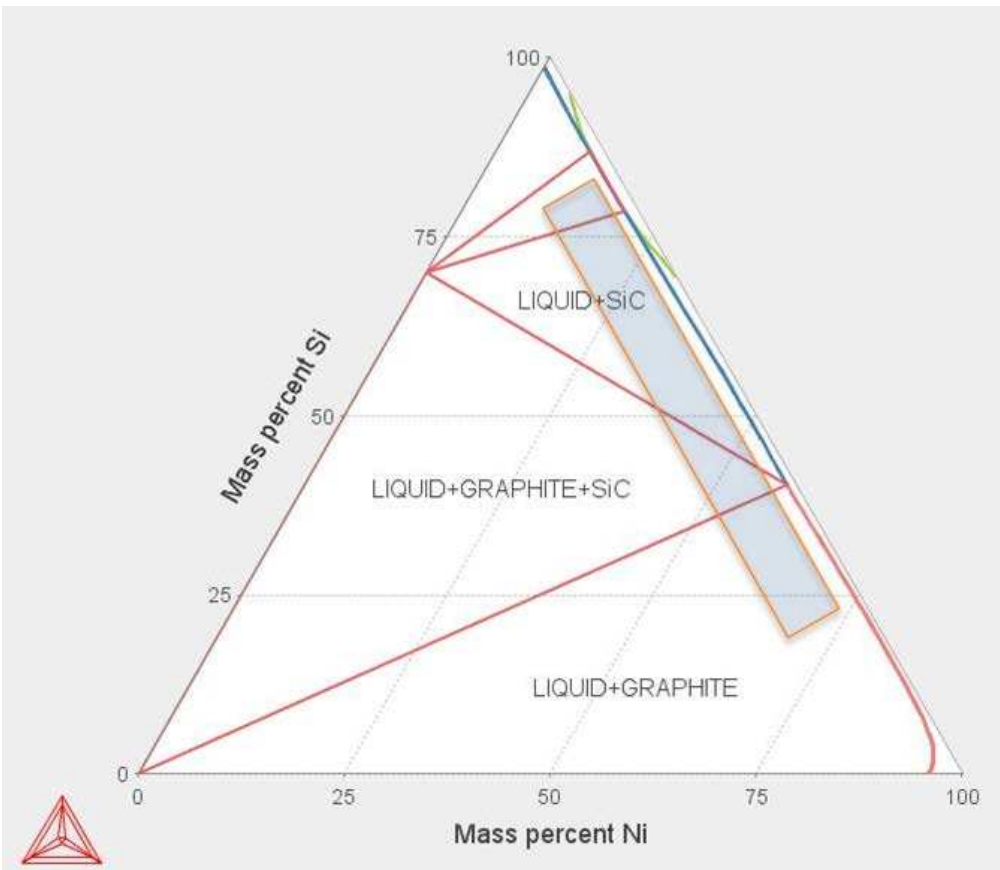

Figure 4.25 Ni-Si-C isothermal ternary phase diagram at 2700 K.

4.4.2 HSC Software Calculations

HSC is a computational thermodynamic software package used for generating free energy tables for various equilibrium reactions at a range of given temperatures. Balanced

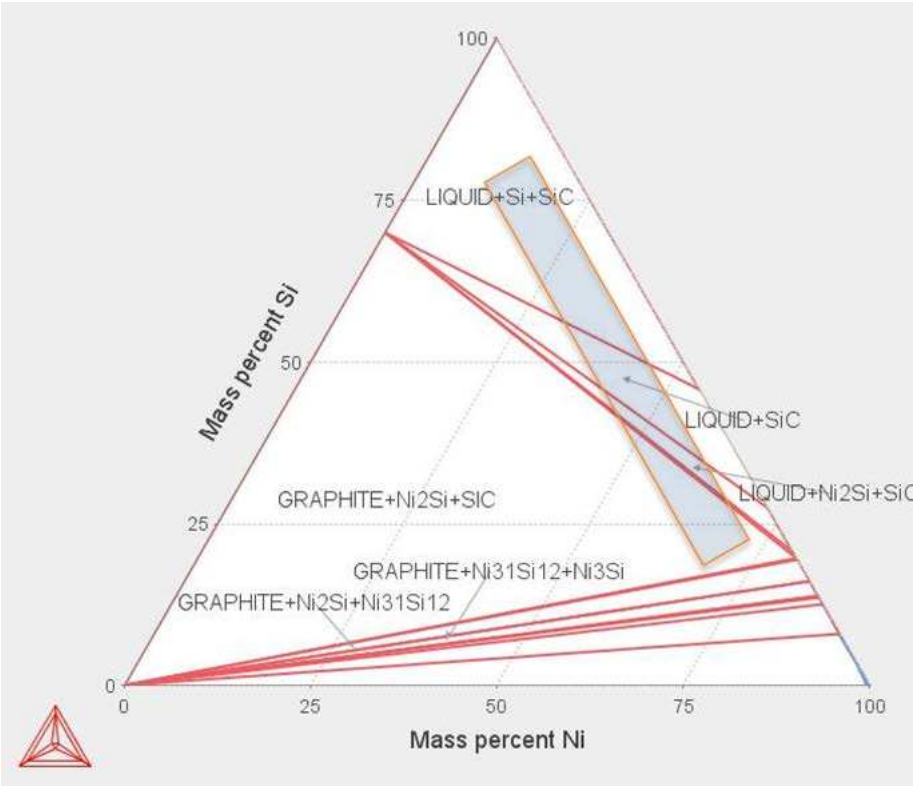

Figure 4.26 Ni-Si-C isothermal ternary phase diagram at 1350 K.

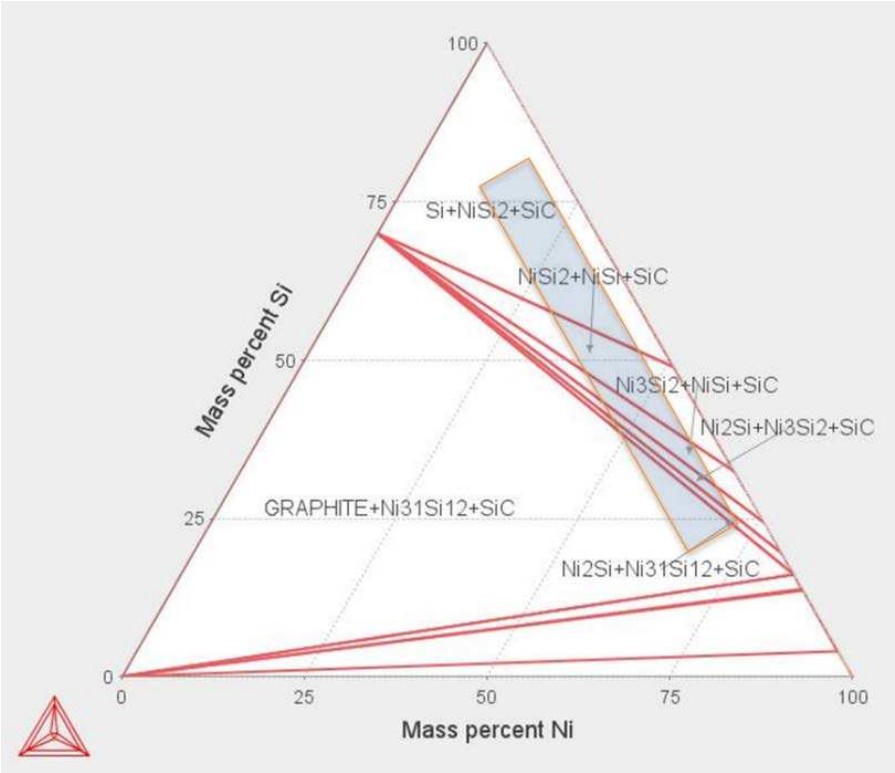

Figure 4.27 Ni-Si-C isothermal ternary phase diagram at 675 K.

reactions are input into the software. Using known thermodynamic values, enthalpy, entropy and free energy, for the overall reaction are generated at a range of temperatures. Comparing free energy (ΔG) values of different reactions at the same temperatures will determine the likelihood for one reaction to occur preferentially over another. Increasingly negative ΔG values mean that the reaction, under equilibrium conditions, does not require the input of an external energy source so it is more thermodynamically favorable for that reaction to occur. By determining which reactions are more negative at high temperatures (deposition temperatures), it can be inferred that said reactions are most likely to occur during deposition. Due to rapid solidification in the deposit, it is likely that phases formed during reactions occurring at high temperatures will constitute the microstructure of the solidified matrix. Table 4.7 shows reaction values generated for a simple Al-SiC reaction. It was assumed that no other alloying elements were present and the reaction takes place under equilibrium heating from 25°C to 2425°C, nearing the vaporization temperature of aluminum under atmospheric pressure. It is determined that, under equilibrium conditions, for all temperatures, it is thermodynamically unfavorable for aluminum and silicon carbide to spontaneously react to form aluminum carbide.

The reaction was expanded to model reactions between Al-Cu-SiC as an example of what may happen in the presence of a copper coating. The model determined that aluminum carbide formation is thermodynamically unfavorable for an Al-Cu-SiC system. This system is illustrated in Table 4.8. The reaction calculation was repeated for the same system with the exception that silicon and carbon were separated and treated as individual elements as reactants. This scenario was considered to simulate the condition of silicon carbide being broken down, as it does when contacted by the electron beam. Evidence of silicon carbide interacting with the electron beam during deposition was observed in the cross-sections of some deposits. The calculations yielded extremely negative free energy values, shown in Table 4.9, which indicate that the formation of aluminum carbide is highly favorable even in the presence of the coating. This, again, is assuming the electron beam had broken the silicon carbide down into individual elements. Aluminum carbide formation is most prevalent around silicon carbide clusters directly under the incident electron beam. Many cases showed shattered particles of silicon carbide surrounded by aluminum carbide, often in regions above the shattered particle. This thermodynamic model validates the proposed mechanisms for forming aluminum carbide in the matrix. Further variations of equilibrium reaction tables are given in Appendix E.

Table 4.7 Equilibrium reaction between aluminum and silicon carbide over 100°C increments.

4Al + 3SiC = Al4C3 + 3Si					
T (K)	**ΔH (kJ)**	**ΔS (J/K)**	**ΔG (kJ)**	**K**	**Log(K)**
298	8.806	-17.148	13.916	3.64E-03	-2.439
398	8.729	-17.368	15.642	8.85E-03	-2.053
498	8.58	-17.697	17.393	1.50E-02	-1.825
598	8.252	-18.292	19.19	2.11E-02	-1.676
698	7.614	-19.27	21.065	2.65E-02	-1.576
798	6.531	-20.712	23.06	3.09E-02	-1.51
898	4.863	-22.674	25.224	3.41E-02	-1.467
998	-39.61	-70.311	30.56	2.51E-02	-1.6
1098	-40.76	-71.41	37.649	1.62E-02	-1.791
1198	-41.705	-72.235	44.833	1.11E-02	-1.955
1298	-42.377	-72.776	52.086	8.01E-03	-2.096
1398	-42.732	-73.041	59.379	6.04E-03	-2.219
1498	-42.738	-73.046	66.686	4.73E-03	-2.326
1598	-42.374	-72.813	73.981	3.82E-03	-2.418
1698	108.915	16.986	80.072	3.44E-03	-2.463
1798	109.371	17.247	78.362	5.29E-03	-2.277
1898	110.099	17.64	76.618	7.78E-03	-2.109
1998	111.1	18.153	74.83	1.11E-02	-1.956
2098	112.372	18.774	72.984	1.52E-02	-1.817
2198	113.91	19.49	71.072	2.05E-02	-1.689
2298	115.711	20.291	69.083	2.69E-02	-1.57
2398	117.768	21.166	67.011	3.47E-02	-1.46
2498	120.073	22.108	64.848	4.40E-02	-1.356
2598	122.62	23.107	62.588	5.52E-02	-1.258
2698	125.399	24.157	60.225	6.82E-02	-1.166
Al4C3	***Extrapolated from***	***2500 K***			
Formula	**FM (g/mol)**	**Conc. (wt-%)**	**Amount (mol)**	**Amount (g)**	**Volume (ml)**
Reactants					
Al	26.982	47.291	4	107.926	39.973
SiC	40.097	52.709	3	120.29	38.066
Products					
Al4C3	143.959	63.08	1	143.959	61
Si	28.086	36.92	3	84.257	36.177

Table 4.8 Equilibrium reaction between aluminum and silicon carbide over 100°C increments in the presence of a copper coating.

4Cu + 5Al + 7SiC = 3Si + 4Cu + Al4C3 + 4SiC +Al					
T (K)	ΔH (kJ)	ΔS (J/K)	ΔG (kJ)	K	Log(K)
298	8.806	-17.148	13.916	3.64E-03	-2.439
398	8.729	-17.368	15.642	8.85E-03	-2.053
498	8.58	-17.697	17.393	1.50E-02	-1.825
598	8.252	-18.292	19.19	2.11E-02	-1.676
698	7.614	-19.27	21.065	2.65E-02	-1.576
798	6.531	-20.712	23.06	3.09E-02	-1.51
898	4.863	-22.674	25.224	3.41E-02	-1.467
998	-39.61	-70.311	30.56	2.51E-02	-1.6
1098	-40.76	-71.41	37.649	1.62E-02	-1.791
1198	-41.705	-72.235	44.833	1.11E-02	-1.955
1298	-42.377	-72.776	52.086	8.01E-03	-2.096
1398	-42.732	-73.041	59.379	6.04E-03	-2.219
1498	-42.738	-73.046	66.686	4.73E-03	-2.326
1598	-42.374	-72.813	73.981	3.82E-03	-2.418
1698	108.915	16.986	80.072	3.44E-03	-2.463
1798	109.371	17.247	78.362	5.29E-03	-2.277
1898	110.099	17.64	76.618	7.78E-03	-2.109
1998	111.1	18.153	74.83	1.11E-02	-1.956
2098	112.372	18.774	72.984	1.52E-02	-1.817
2198	113.91	19.49	71.072	2.05E-02	-1.689
2298	115.711	20.291	69.083	2.69E-02	-1.57
2398	117.768	21.166	67.011	3.47E-02	-1.46
2498	120.073	22.108	64.848	4.40E-02	-1.356
2598	122.62	23.107	62.588	5.52E-02	-1.258
2698	125.399	24.157	60.225	6.82E-02	-1.166
	Al4C3	***Extrapolated from***	***2500 K***		
Formula	**FM (g/mol)**	**Conc. (wt-%)**	**Amount (mol)**	**Amount (g)**	**Volume (ml)**
Reactants					
Cu	63.546	37.951	4	254.184	28.369
Al	26.982	20.142	5	134.908	49.966
SiC	40.097	41.906	7	280.676	88.821
Products					
Si	28.086	12.58	3	84.257	36.177
Cu	63.546	37.951	4	254.184	28.369
Al4C3	143.959	21.494	1	143.959	61
SiC	40.097	23.947	4	160.386	50.755
Al	26.982	4.028	1	26.982	9.993

Table 4.9 Equilibrium reaction between aluminum and dissolved silicon carbide over 100°C increments in the presence of a copper coating.

4Cu + 5Al + 5Si + 7C = Si + 4Cu + Al4C3 + 4SiC +Al					
T (K)	**ΔH (kJ)**	**ΔS (J/K)**	**ΔG (kJ)**	**K**	**Log(K)**
298	-494.506	-73.667	-472.553	6.89E+82	82.838
398	-494.94	-75.015	-465.084	1.11E+61	61.044
498	-494.823	-74.753	-457.596	1.00E+48	48.001
598	-494.912	-74.905	-450.119	2.09E+39	39.321
698	-495.442	-75.715	-442.593	1.33E+33	33.124
798	-496.514	-77.141	-434.955	2.97E+28	28.473
898	-498.231	-79.16	-427.145	7.05E+24	24.848
998	-542.813	-126.912	-416.155	6.07E+21	21.783
1098	-544.169	-128.208	-403.396	1.56E+19	19.192
1198	-545.291	-129.187	-390.524	1.07E+17	17.029
1298	-546.222	-129.935	-377.566	1.57E+15	15.195
1398	-546.997	-130.511	-364.543	4.19E+13	13.622
1498	-547.64	-130.955	-351.469	1.81E+12	12.257
1598	-548.156	-131.29	-338.355	1.15E+11	11.061
1698	-749.274	-250.659	-323.655	9.06E+09	9.957
1798	-748.637	-250.295	-298.606	4.74E+08	8.676
1898	-747.707	-249.792	-273.601	3.39E+07	7.53
1998	-746.478	-249.162	-248.652	3.17E+06	6.501
2098	-744.941	-248.412	-223.772	3.73E+05	5.572
2198	-743.087	-247.549	-198.973	5.36E+04	4.729
2298	-740.904	-246.579	-174.266	9.15E+03	3.961
2398	-738.38	-245.504	-149.661	1.82E+03	3.26
2498	-735.503	-244.329	-125.169	4.15E+02	2.618
2598	-732.259	-243.057	-100.799	1.06E+02	2.027
2698	-728.636	-241.688	-76.561	3.04E+01	1.482
	Al4C3	***Extrapolated from***	***2500 K***		
Formula	**FM (g/mol)**	**Conc. (wt-%)**	**Amount (mol)**	**Amount (g)**	**Volume (ml)**
Reactants					
Cu	63.546	41.425	4	254.184	28.369
Al	26.982	21.986	5	134.908	49.966
Si	28.086	22.886	5	140.428	60.295
C	12.011	13.702	7	84.077	32.09
Products					
Si	28.086	4.577	1	28.086	12.059
Cu	63.546	41.425	4	254.184	28.369
Al4C3	143.959	23.462	1	143.959	61
SiC	40.097	26.139	4	160.386	50.755
Al	26.982	4.397	1	26.982	9.993

4.4.3 Empirical Heat Diffusivity Criterion

Industrial producers of metal matrix composites generally use casting methods to produce large quantities of the material. This is done by melting the metal matrix, then introducing the reinforcement particulates into the melt. During the design process of the composite, a simple model is used to determine the affinity for various particulates to preferentially disperse in the melt or be pushed out of the melt ahead of the solidification front. The empirical heat diffusivity criterion uses material constants, thermal conductivity (K), density (ρ), and specific heat (C), to predict whether dispersion is likely to occur. A ratio is calculated by the formula [50]:

$$\sqrt{\frac{(K_p \rho_p C_p)}{(K_l \rho_l C_l)}} > 1 \qquad \textbf{\textit{(4.1)}}$$

If the ratio is greater than one, dispersion is likely to occur. If the ratio is less than one, particles are likely to be pushed ahead of the solidification front and be rejected from the matrix. Table 4.10 illustrates the prediction of this simple model for different cases of coated and uncoated particles in the matrix. It was assumed that the coated silicon carbide behaves as the coating would if it were a solid particle. The data shows that it is unfavorable for silicon carbide to disperse in an aluminum matrix. If the coating does not dissolve and there is no mixing with the liquid, copper coated particles would likely disperse easily in the matrix. However, if the coating dissolves and creates a region of high liquid copper or nickel content around the matrix, it can be assumed that the particulates are suspended in either a copper or nickel liquid. In that case it is more likely for silicon carbide to disperse by having a nickel coating. This scenario is represented by measurements taken from the cross-sections of deposits containing coated and uncoated deposits. Uncoated deposits are generally rejected from the matrix. Deposits containing high copper content coated silicon carbide particles showed the worst dispersion values, while deposits that contain nickel coated particles generally showed the highest amount of dispersion.

4.5 Computational Fliud Mechanics Modeling

A computational fluid mechanics model was created to predict what velocity the melt pool must achieve to disperse particles in the matrix. The model is dependent on two main variables, particle radius (r_p) and viscosity (η). Equation 7 was used to predict the various steady-state velocities (ν_{ss}) that must be surpassed in the melt pool in order to disperse silicon carbide under different liquid matrix conditions. It was assumed that the nickel and copper

coatings were

Table 4.10 Empirical heat diffusivity criterion values calculated for various possible particle/liquid interactions.

Particle/Liquid	SiC/Al	Ni/Al	Cu/Al	SiC/Ni	SiC/Cu
Ratio	0.51	0.49	2.39	1.05	0.22

incorporated into the liquid metal, so all conditions use 1250 kg/m^3 as the particle density (ρ_p), the density of silicon carbide. Liquid density (ρ_1) is 2385 kg/m^3, the density of 6061 aluminum alloy. Using density values of aluminum and silicon carbide, the equation is:

$$v_{ss} = \frac{2474.3 * r_p^2}{\eta} \quad \textbf{(4.2)}$$

The equation was analyzed with respect to particle radius and viscosity, respectively. Average particle radius was 22.8 µm given by laser light scattering of uncoated silicon carbide particles. This value was used when calculating steady-state velocities with respect to viscosity. For aluminum, viscosity is given by:

$$\eta = 0.1492\exp\left(\frac{1984.5}{T}\right) \quad \textbf{(4.3)}$$

where T is the melt pool temperature. Melt pool temperature was determined by using an infrared pyrometer to measure temperature values in the GTAF^3 system during deposition shown in Figure 4.28. The average temperature is given by the dashed line. These values were used to calculate the change in viscosity of the matrix during deposition. Figures 4.29 and 4.30 display Al-Cu and Al-Ni phase diagrams, respectively. These phase diagrams were used to determine compositions of various liquids that may exist in local regions around coated particles. Viscosities for liquid Al, Cu, Ni, Al_3Ni, AlNi, $AlNi_3$, Al_2Cu, and $Al_{0.1}Cu_{0.9}$ were calculated using the rule of mixtures. From this procedure outlined an approximation of velocities can be used to determine the best coating for enhancing dispersion.

High speed video analysis of particles moving in a matrix during deposition provided data for actual melt pool velocities. Comparing melt pool velocity to steady-state velocity it can be determined that melt pool velocities higher than steady-state velocities will yield dispersion in the matrix. Figure 4.31 Illustrates the velocities required for silicon carbide particles to disperse

in various liquid matrices with respect to particle radius. Data points above respective solid lines indicate that particles of the specified radius will disperse in that particular liquid composition. This data is validated by mean free path measurements taken from EBF^3 deposits.

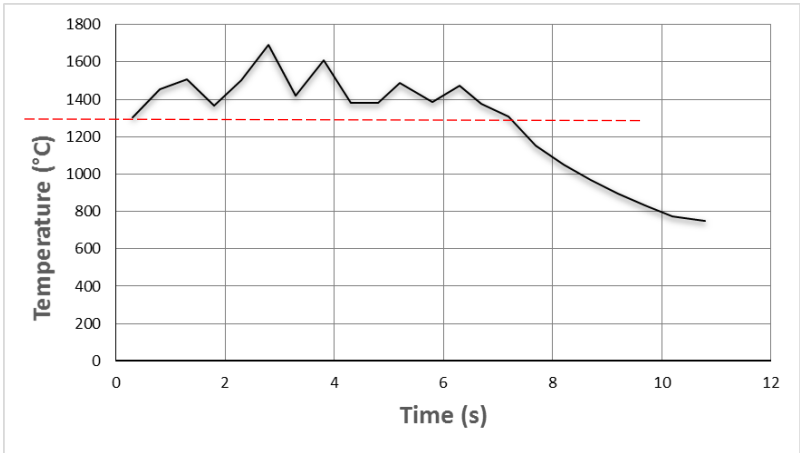

Figure 4.28 Time and temperature data of the melt pool in the GTAF^3 system measured using an infrared pyrometer.

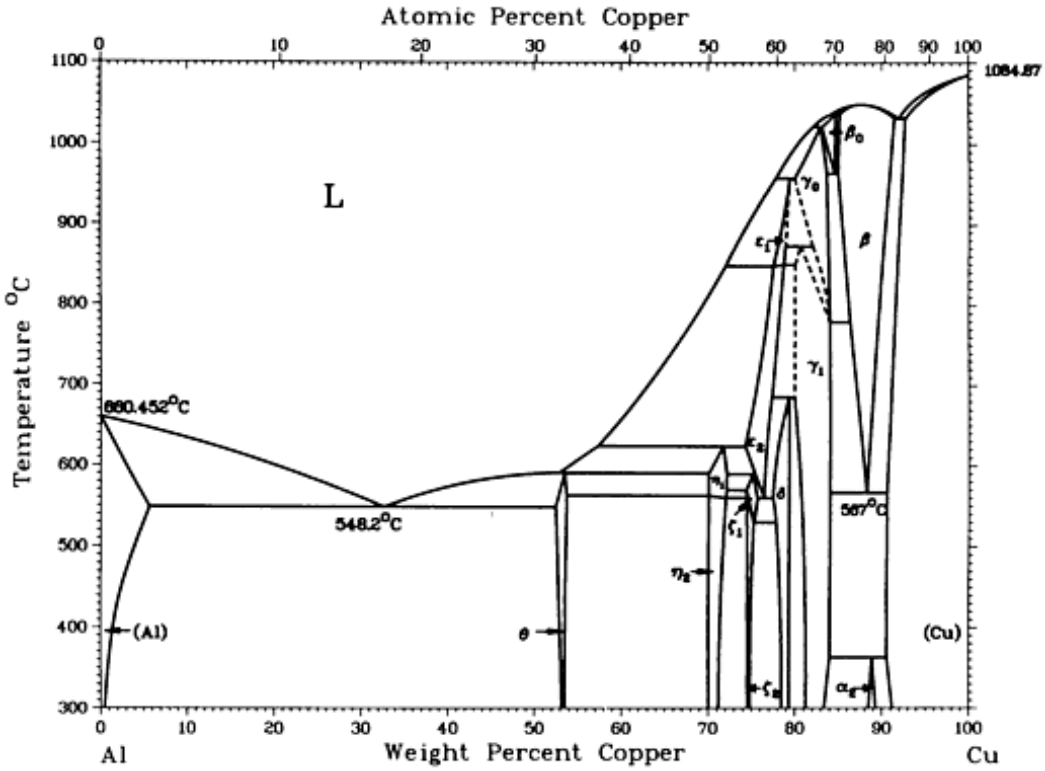

Figure 4.29 Al-Cu binary phase diagram used to predict what phases may form in localized regions as a result of using copper coated silicon carbide particles [51], [52].

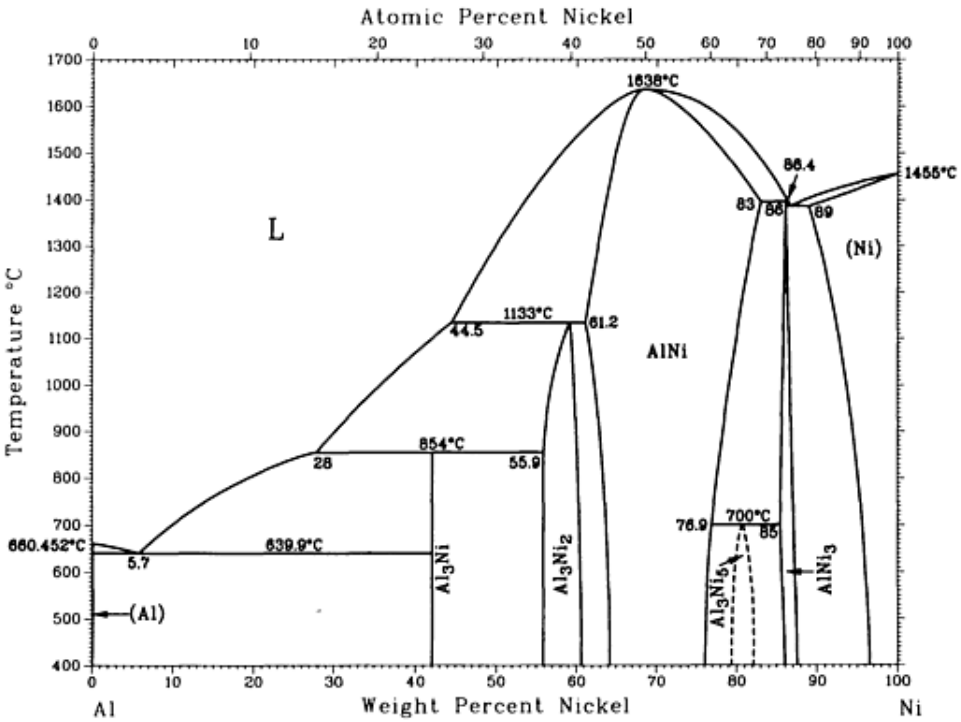

Figure 4.30 Al-Ni binary phase diagram used to predict what phases may form in localized regions as a result of using nickel coated silicon carbide particles [51], [53].

Deposits with nickel content and low copper content enhanced dispersion compared to deposits containing uncoated and high copper coated silicon carbide. By examining the relationship of velocity to temperature, or viscosity, Figure 4.32 again shows the favorability for silicon carbide to disperse in nickel and low copper containing liquids. However, deposits containing nickel will have a higher melting temperature as illustrated by vertical lines in Figure 4.32 which makes it difficult for complete dispersion due to the shortened time in the liquid state. Solidification rate, convection and particles radius are important factors when determining dispersion. This model did not take into account convection or the critical agglomeration size for particles. High convection rates and small particle size can lead to agglomeration even if the critical velocity for dispersion is reached or exceeded [38]. Future iterations or wire must contain particles with a critical particle size to mitigate agglomeration. Data tables and charts containing particle radius, viscosity, temperature, and velocity values are available in Appendix E.

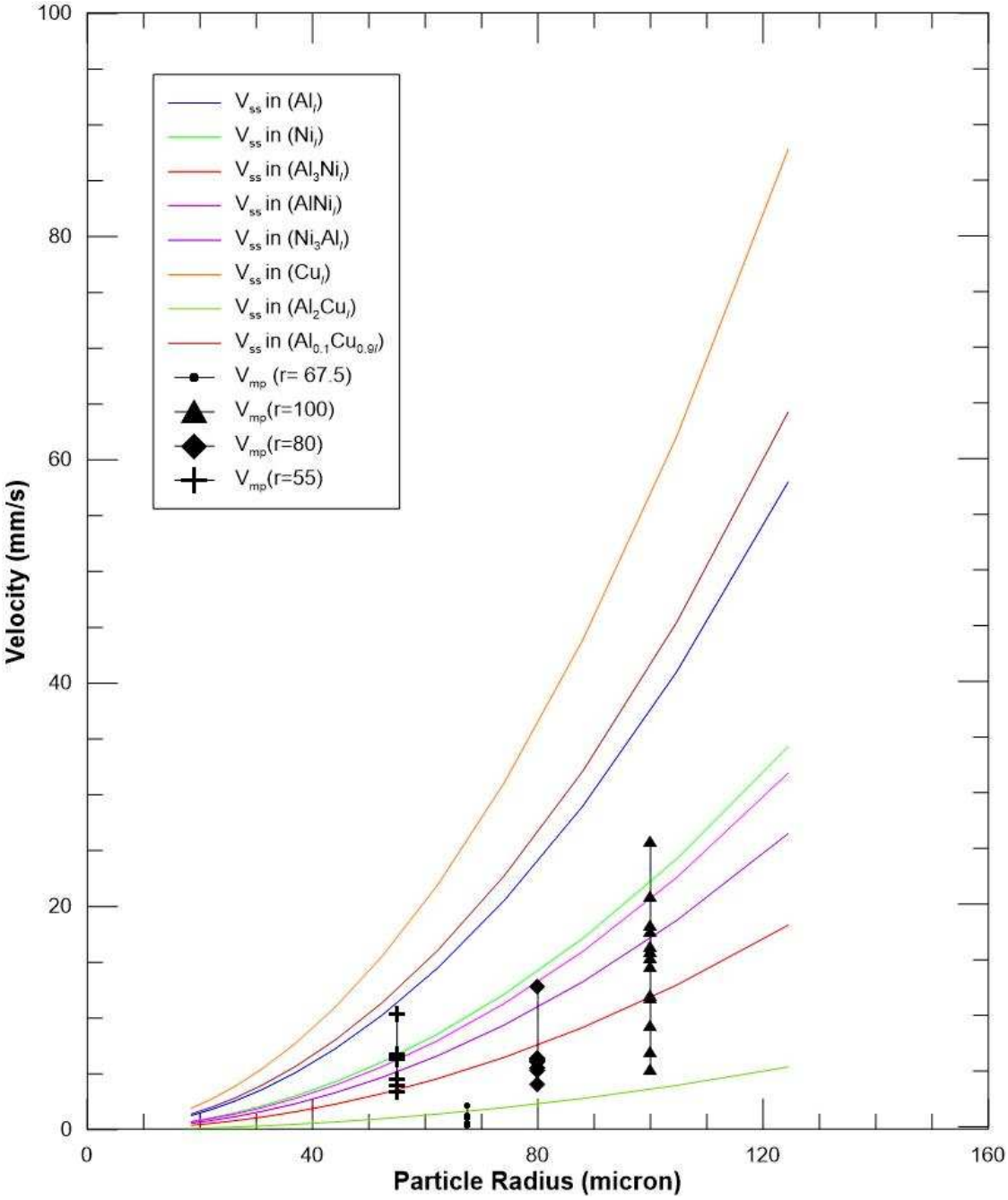

Figure 4.31 The required velocity to promote dispersion as a function of particle radius for various liquids that may be present in the matrix in localized regions.

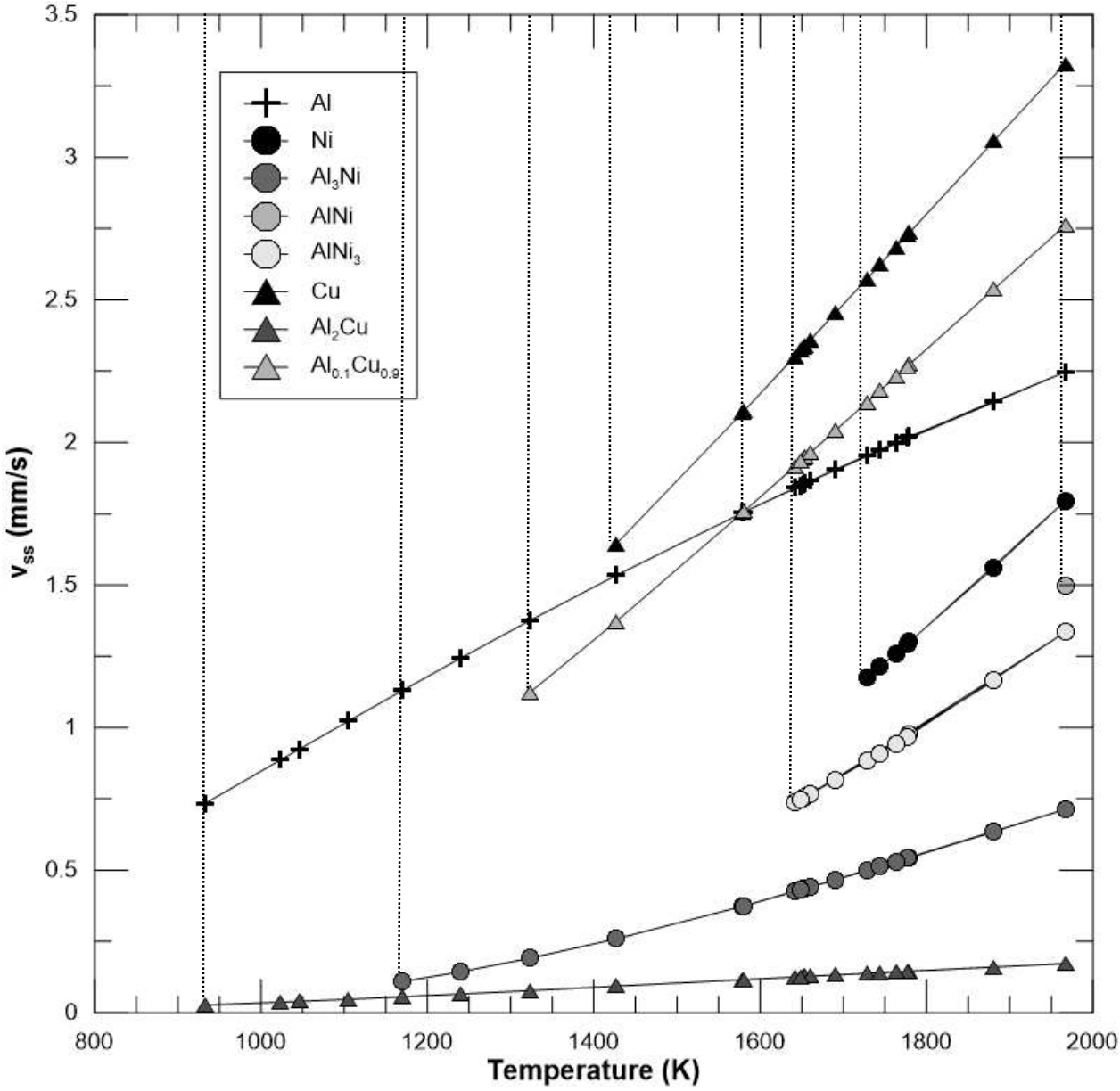

Figure 4.32 The required velocity to promote dispersion as a function of temperature (viscosity) for various liquids that may be present in the matrix in localized regions. Vertical lines indicate the melting temperature for each liquid.

CHAPTER 5: CONCLUSIONS

Metal matrix composite wire consumables were created at the Colorado School of Mines specifically to be used in the EBF^3 system at NASA-Langley Research Center. Variations of the coatings of the reinforcement particles as well as electron beam parameters were made to create a uniform metal matrix composite structure using EBF^3. Analysis conducted on the wire consumables and EBF^3 deposits was used to determine modifications made to wire development for future metal matrix composite consumables. Major conclusions drawn from this research are as follows:

Through image analysis, it was determined that silicon carbide was uniformly distributed in the wire prior to deposition. The volume fraction of reinforcement particles in the wire reached a maximum of 41 pct. of the target volume fraction. The difference may have been caused by segregation issues during mixing due to density differences and static charging of the particles.

Compositional analysis revealed that copper additions in the wires were out of Al 6061 alloy specifications prior to deposition. The magnesium content was increased to 200 pct. of the desired composition to accommodate vaporization loss during deposition.

Compositional analysis of the deposits, however, determined that there is actually 75 to 80 pct. vaporization loss of magnesium during deposition, compared to the 50 pct. measured for monolithic aluminum alloy wires. This extra loss of magnesium caused the deposits to fall outside the compositional specifications designated for Al 6061 alloys.

All deposits, regardless of particle coating or beam condition, exhibited some degree of clustering of the reinforcement particles. It was determined that using low amounts of copper or nickel coating, or non-pulsed electron beam parameters, enhanced particle dispersion in the matrix.

High nickel content eliminates the formation of aluminum carbide. Low nickel content was the best coating for mitigating aluminum carbide formation, enhancing dispersion, and retaining a high volume fraction of silicon carbide in the matrix. Deposits with high copper content performed poorly in all areas of study.

It was determined that the use of a defocused beam provides the best depositions for all materials. Deposits made using a defocused beam contained low amounts of aluminum carbide formation and high amounts of retained silicon carbide while providing the best conditions for

particle dispersion. The defocused beam condition also produced deposits with a large overfill height and small depth of penetration, which is ideal for reducing the amount of disturbance to previous layers during deposition.

Thermodynamic models were created to predict phases formed during deposition. The models showed that if the silicon carbide is broken up, carbon and aluminum are likely to form aluminum carbide because of the favorable thermodynamics.

The empirical heat diffusivity criterion shows that it is much more favorable for silicon carbide to disperse with a nickel coating rather than a copper coating. The fluid dynamics model also determines that kinetically it is easier to disperse silicon carbide with a nickel coating. Low amounts of copper were found to disperse the SiC particulates. Results from analysis of the deposits validate the models. The fluid mechanics model also shows that high amounts of nickel will disperse the particles, but only at temperatures higher than the operating temperatures measured.

Materials created for this study showed potential to deposit metal matrix composite structure using EBF^3. The results collected from this study were used to gain a better understanding of the compatibility and interactions of silicon carbide particles with an aluminum matrix under non-equilibrium conditions. These results will serve as a baseline for modifying current iterations of materials and beam conditions to create homogenous metal matrix composite structures, using EBF^3, for commercial production.

CHAPTER 6: RECOMMENDATIONS FOR FUTURE WORK

Thermodynamic and kinetic calculations were used to predict particle behavior, and exploratory deposition of the Al/SiC MMC was performed under the current activity. Two main challenges left to overcome are the elimination of aluminum carbides which are detrimental to the matrix and uniform particle dispersion. Initial calculations did not account for surface tension effects. It is theorized that surface tension of the liquid aluminum matrix may be contributing to particle clustering of the matrix. Thermodynamic models can be expanded to include the effects of surface treatments of the SiC on the propensity for matrix/particulate reaction. Creating a computational model of the Al/SiC system including the effects of surface tension will provide additional insight to modify particulate surface conditions and the matrix alloy to eliminate aluminum carbide formation and enhance particle dispersion. Further optimization of the EBF^3 deposition parameters, including melt pool agitation, may be explored to further promote uniform dispersion. Surface tension and fluidity experiments conducted based on current compositional ranges can be used to verify the model and determine an optimal compositional range for dispersing the particles uniformly throughout the matrix. The anticipated outcome is to produce materials with superior mechanical properties (e.g. stiffness and strength) that can be tailored for optimal structural efficiency.

As guided by the models, modifications can be made to the aluminum alloy and the surface condition of the reinforcement particles to inhibit the formation of detrimental phases (secondary carbides), enhance the wettability and dispersion of the particles in the matrix and reduce the crack susceptibility of the solidified structure. A number of powder cored tubular wires produced using design of experiments (DOE), adjusting particulate volume fraction and size can be deposited using the EBF^3 process. Samples extracted for compositional analysis can be compared with the composition of the wires to determine vaporization loss. Microstructural analysis using electron microscopy combined with image analysis methods would serve as viable methods to determine grain size and spatial distribution of the particles in the matrix and perform phase identification. Mechanical property testing of the deposited materials will evaluate strength, elastic modulus, and fracture toughness and additional properties as directed by results. Measured properties compared with commercial metal matrix composites would verify the feasibility of using this material in real applications. Iterations in alloy chemistry and particulate condition and volume percent would optimize the PCTW composition and properties of the

resulting deposited materials.

Upon successful deposition of the MMC wires, materials with composition grades from monolithic aluminum to the metal matrix composite can be deposited and characterized to determine uniformity of the gradient. Since the development of graded metal matrix composite structures created by electron beam freeform fabrication is a new sector of research, methods for characterization of graded composition materials should be researched and modified as needed to enable characterization sufficient to correlate mechanical properties with composition and microstructural gradients. Mechanical testing techniques such as micro-tensile testing with digital image correlation and micro hardness are such examples of characterization techniques that may be used to determine properties along the gradient.

Reinforcement variations such as whisker, and continuous fiber SiC can be explored for the future development of MMC deposits with orientation dependent properties. The feasibility of implementing other carbides into an aluminum matrix would serve as a precursor to develop other MMC wire feedstock for the EBF^3 system.

CHAPTER 7: REFERENCES

[1] K.Tamminger, M. Domack, R. Hafley, NASA Langley Research Center, Unpublished communication. 2015.

[2] Hillier, C. K. (2010). Powder-cored Tubular Wire Development for Electron Beam Freeform Fabrication.

[3] J.J. Beaman, et al., Solid Freeform Fabrication: A New Direction in Manufacturing, Kluwer Academic Publishers: Norwell, Massachusetts, 1997.

[4] K.M.B. Taminger and R. A. Hafley, "Electron beam freeform fabrication: a rapid metal deposition process," Proceedings of the 3rd Annual Automotive Composites Conference, Society of Plastics Engineers, Sept. 9-10, Troy, Michigan, 2003.

[5] Mitzner, S. V. (2012). Grain Refinement and Epitaxial Interruption.

[6] M. Karen and M. T. Robert, "Electron Beam Freeform Fabrication for Cost Effective Near-Net Shape Manufacturing."

[7] K. M. B. Taminger and R. A. Hafley, "ELECTRON BEAM FREEFORM FABRICATION : A RAPID METAL DEPOSITION PROCESS," 2003.

[8] J. H. Adams, M. Ammons, and H. S. Avery, ASM Handbook: Volume 2 Properties and Selection: Nonferrous Alloys and Special-Purpose Materials. ASM International, 1992, p. 3470.

[9] E. A. Starke and J. T. Staleyt, "Application of Modern Aluminum Alloys to Aircraft," vol. 32, no. 95, pp. 131–172, 1996.

[10] Mel M. Schwartz, "Metal Matrix Composite Processing," in in *Composite Materials Porcessing, Fabrication, and Applications*, Prentice Hall PTR, 1997, pp. 143–207.

[11] G. E. Totten and D. S. MacKenzie, *Handbook of Aluminum Volume 2 Alloy Production and Materials Manufacturing*. New York, NY: Marcel Dekker Inc., 2003, p. 724.

[12] J. V. Foltz and C. M. Blackmon, "Metal-Matrix Composites," in in *ASM Handbook: Composites*, 2001, pp. 903–912.

[13] A. R. I. Khedera, G. S. Marahleh, and D. M. K. Al-Jameaa, "Strengthening of Aluminum by SiC, Al2O3 and MgO," *Jordan Journal of Mechanical and Industrial Engineering*, vol. 5, no. 6, pp. 533–541, 2011.

[14] W.M. Khairaldien, A.A. Khalil, and M.R. Bayoumi, "Production of Aluminum-Silicon Carbide Composites Using Powder Metallurgy at Sintering Temperatures above the Aluminum Melting Point,"

[15] Davidson, A. M., & Regener, D. (2000). A comparison of aluminium-based metal-matrix composites reinforced with coated and uncoated particulate silicon carbide, *60*, 865–869.

[16] J. Hashim, L. Looney, and M. S. J. Hashmi, “The enhancement of wettability of SiC particles in cast aluminium matrix composites,” vol. 119, pp. 329–335, 2001.

[17] D. Olsen, T. Siewert, S. Liu, and G. Edwards, *ASM handbook: welding, brazing, and soldering*. ASM International, 1993, pp. 1350-2873.

[18] T. Iseki, T. Kameda, and T. Maruyama, INTERFACIAL REACTIONS BETWEEN SIC AND ALUMINUM DURING JOINING, *J. MATER. SCI.*, Vol. 19, 1984, P 1692-1698

[19] L. G. Suery M, “Interfacial reactions and mechanical behaviour of aluminium matrix composites reinforced with cera- mic particles,” Key Engineering Materials, 1993, pp. 79–80;33–46.

[20] J. Hashim, L. Looney, and M. S. J. Hashmi, “The wettability of SiC particles by molten aluminium alloy,” vol. 119, pp. 324–328, 2001.

[21] Leon, C. A., & Drew, R. A. L. (2000). Preparation of nickel-coated powders as precursors to reinforce MMCs. *Journal of Materials Science*, *35*, 4763–4768.

[22] W.H. Kearns, AWS Welding Handbook: Volume 4 Metals and Their Weldability. AWS, 7th ed. 1982, pp. 316-358.

[23] R.A. Chihoski, the Character Of Stress Fields Around A Weld Arc Moving On Aluminum Sheet, *Weld J.*, Vol. 51 (NO. 1), 1972, P 9-S.

[24] C.L. CROSS, "Weldability of Aluminum-Lithium Alloys: an Investigation of Hot Tearing Mechanisms," PH.D. Thesis, Colorado School of Mines, Golden, CO, 1986, P 144.

[25] A.R.E. Singer and P.H. Jennings, “Hot Shortness of the Aluminum Silicon Alloys of Commercial Purity,” *J. INST. MET.*, VOL 73, 1947, P 197.

[26] W.I. Pumphrey and J.V. Lyons, “Cracking During the Casting and Welding of the More Common Binary Aluminum Alloys,” *J. INST. MET.*, VOL 74, 1948, P 439.

[27] J.D. Dowd, “Weld Cracking of Aluminum Alloys” *Weld. J.*, VOL 31 (NO. 10), 1952, P 448-S.

[28] P.H. Jennings, A.R.E. Singer, and W.I. Pumphrey, “Hot-shortness of some High Purity alloys in the Systems Aluminum-copper-silicon and Aluminum-magnesium-silicon,” *J. INST. MET.*, 1948, P 227.

[29] J.K. Dawson, “Weld Crack Sensitivity of Aluminum Alloys,” *MET. PROG.*, VOL 76 (NO.1), 1959, P 116.

[30] R.P. Meister and D.C. Martin, "Welding of Aluminum and Aluminum Alloys, "Defense Metals Information Center, Battelle Memorial Institute, 1967, P 51.

[31] S. Kou, *Welding Metallurgy*, John Wiley & Sons, 1987, P 239.

[32] B. Altshuller, W. Christy, and B. Wiskel, “GMA Welding of Al-Al_2O_3 Metal Matrix Composite,” *Weldability of Materials, PROC. MATERIALS WELDABILITY SYMP.* ASM International, 1990, P 305-309.

[33] P.K. Rohatgi, R. Asthana, and S. Das, “Solidification, Structures, and Properties of Cast Metal-ceramic Particle Composites,” *INT. MET. REV.*, VOL 31 (NO. 3), 1986, P 115-139.

[34] S.H. Lo, S. Dionne, M. Popescu, S. Gedeon, and C.T. Lane, Effects Of Prior- and Post-weld Heat Treatments on the Properties of SiC/Al-Si Composite Gas Metal Arc Welded Joints, *Proc. Advances in Production and Fabrication of Light Metals and MMCs,* M. Avedesian, L. Larouche, and J. Masounave, ED., Canadian Institute of Mining, Metallurgy and Petroleum, 1992, P 575-588.

[35] Lienert, T. J., Brandon, E. D., & Lippold, J. C. (1993). Laser and electron beam welding of SiCp reinforced aluminum A-356 metal matrix composite. *Scripta Metallurgica et Materialia*, *28*(11), 1341–1346.

[36] Kivineva, E.I. (1991). Particulate Metal Matrix Composite as a Weld Deposit.

[37] D.R. Uhlmann, B. Chalmers and K.A. Jackson, “Interaction between Particles and a Solid-Liquid Interface,” J. Applied Physics, 25, 2986-2993 (1965).

[38] D.M. Stefanescu, B.K. Dhindaw, S.A. Kacar and A. Moitra, “Behavior of Ceramic Particles at the Solid-Liquid Metal Interface in Metal Composites,” Met. Trans., 19A, 2847-2855 (1988)

[39] D. Azbel and A.I. Liapis, “Motion of Solid Particles in a Liquid Medium,” ed. N.P. Cheremisinoff and R. Gupta, Ch. 34, Ann Arbor Science Publishers, Ann Arbor, Michigan (1982).

[40] L. Lajoye and M. Suery, “Modelling of Particle Segregation during Casting of Al-Matrix Composites,” Cast Reinforced Metal Composites, ASM, Metals Park, Ohio (1988)

[41] K. Kuper, Federal Technology Group, Unpublished Communication. 2015.

[42] Webb, P. A. (2000). A Primer on Particle Sizing by Static Laser Light Scattering. *Instrumentation*, (January).

[43] S. Gvorchin, CoorsTeK, Unpublished Communication. 2015.

[44] R. Serway, Physics for Scientists and Engineers with Modern Physics, 3rdEd, Saunders College Publishing, (1990).

[45] E.N. Andrade: Phil. Mag. 17 (1934) 698.

[46] Belov, N. a., Eskin, D. G., & Avxentieva, N. N. (2005). Constituent phase diagrams of the Al-Cu-Fe-Mg-Ni-Si system and their application to the analysis of aluminium piston alloys. *Acta Materialia*, *53*(17), 4709–4722.

[47] D.J. Chakrabarti, B. Cheong, D.E. Laughlin, "Precipitation in Al-Mg-Si-Cu Alloys and the Role of the Q Phase and its Precursors," Automotive Alloys II (1998)

[48] M. Lech-Grega, S. Boczkal, "Iron Phases in Model Al-Mg-Si-Cu Alloys," Mat. Science Forum, Vol. 674, pp 135-140, (2011).

[49] Porter, D. A., and Easterling, K. E., *Phase Transformations in Metals and Alloys* (2nd Edition), Chapman & Hall, 1992.

[50] D.M. Stefanescu, et al. *ASM handbook: Casting*. ASM International, 1993, pp. 1492-1584.

[51] *ASM handbook: Alloy Phase Diagrams*. ASM International, 1993, pp. 291.

[52] J.L. Murray. (1985)

[53] P. Nash, M.F. Singleton, J.L. Murray. (1991)

APPENDIX A: WIRE CHARACTERIZATION

Wire samples were cross-sectioned axially as well as longitudinally to examine the integrity of the lap joint as well as the compaction of the powder cored. Images are studied to distinguish the various powder additions, determine if there are large voids in the core and to determine if silicon carbide distribution is uniform throughout the core. Uniformity is considered over a 1 mm length of longitudinal cross-section.

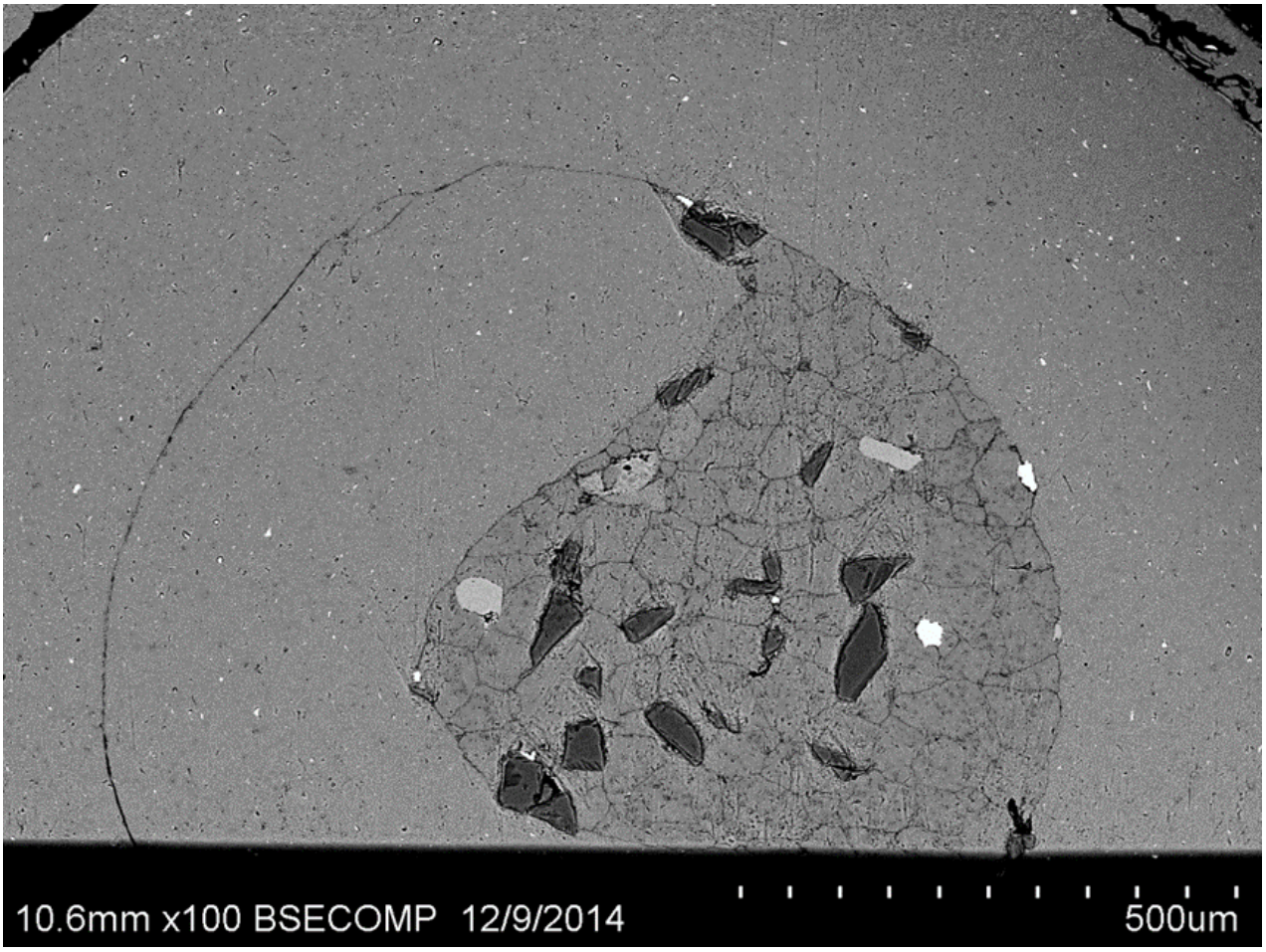

Figure A.1 Axial cross-sectional backscattered electron image of a wire containing uncoated silicon carbide. The integrity of the lap joint is maintained and particles are fully packed in a uniform distribution.

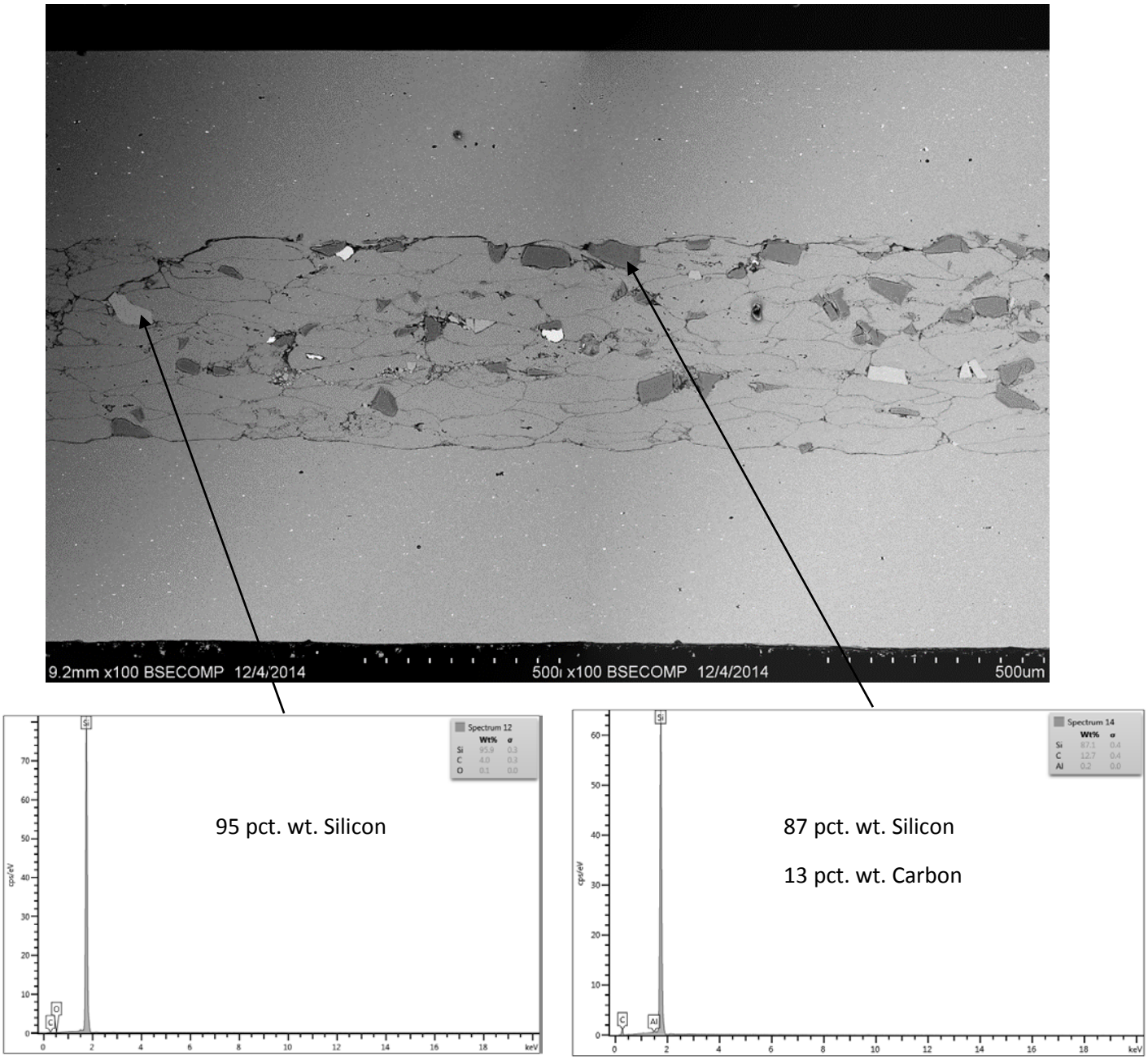

Figure A.2 A longitudinal cross sectional backscattered electron image of a wire containing uncoated silicon carbide. EDS and contrast measurements determine the difference between silicon (light) and silicon carbide (dark) particles in the wire. Relatively uniform distribution of silicon carbide particles in the wire is shown. Voids are not present in the core of the wire.

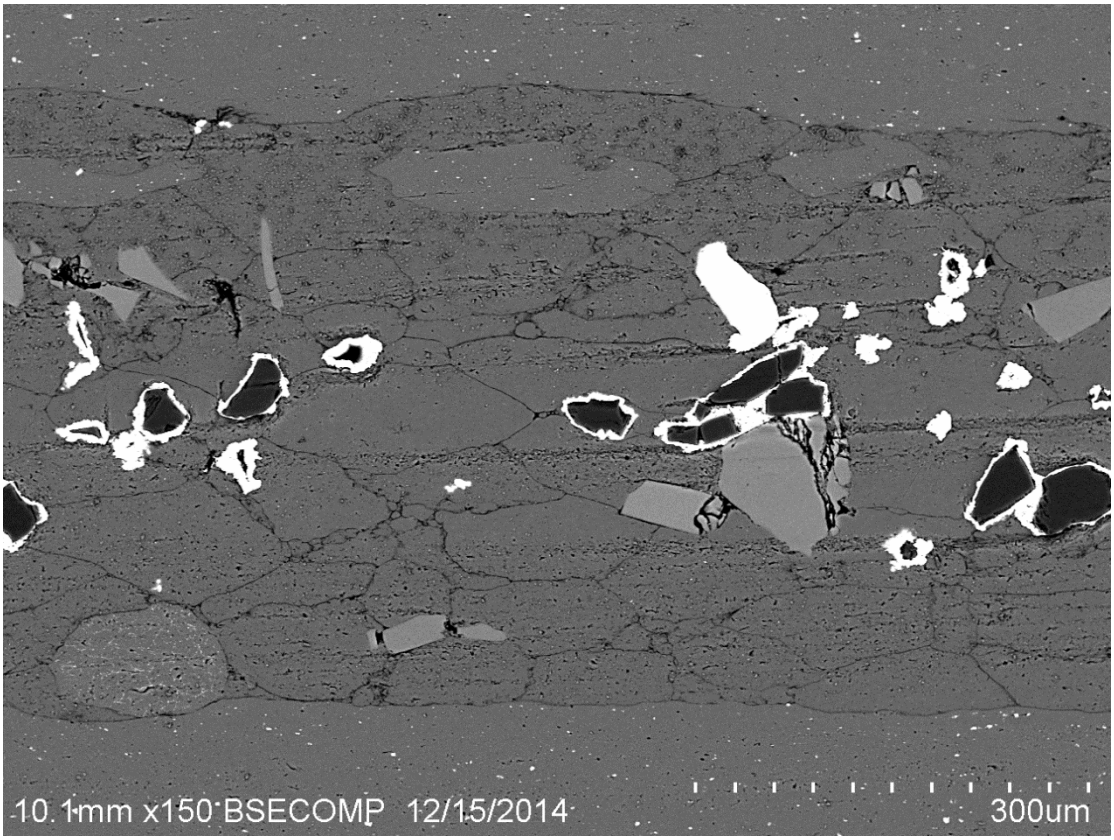

Figure A.3 A longitudinal cross sectional backscattered electron image of a wire containing silicon carbide with a high copper content. High copper content particles agglomerate towards the center of the wire in a straight line. The copper coating was determined to maintain uniform coverage on the silicon carbide particle.

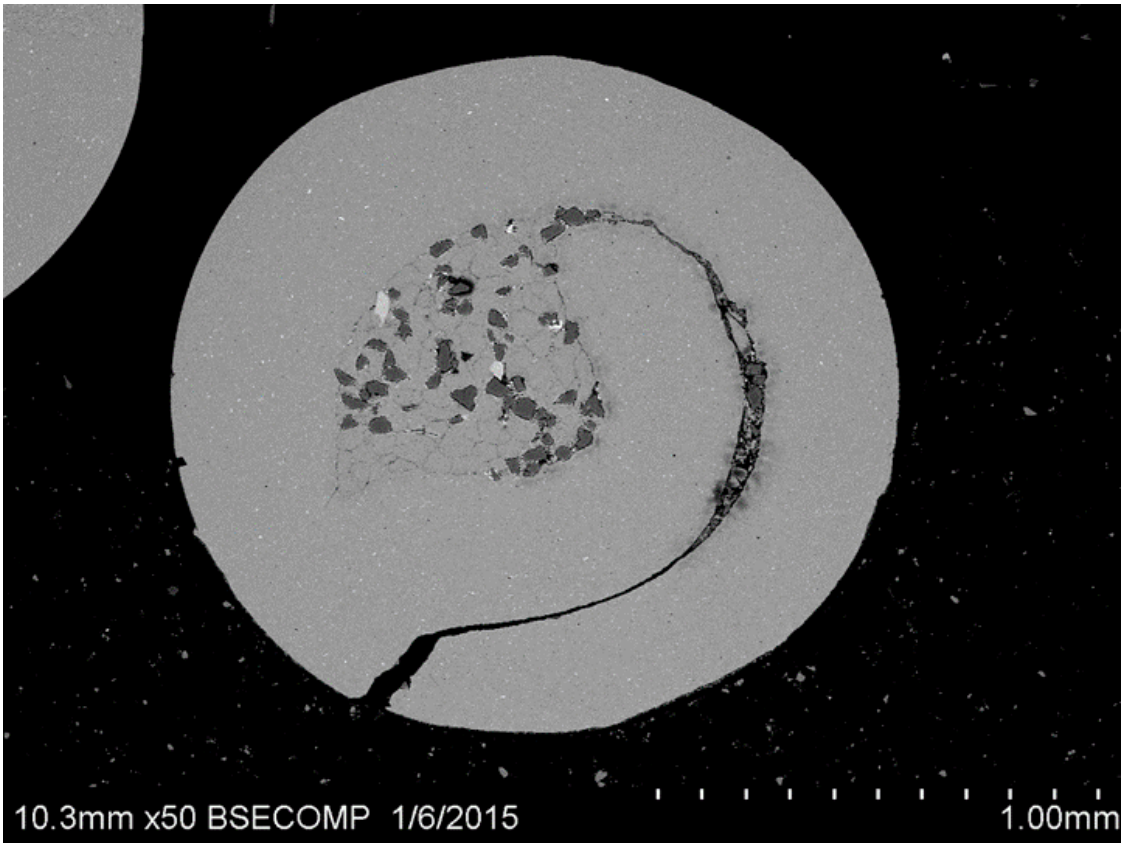

Figure A.4 Axial cross-sectional backscattered electron image of a wire containing silicon carbide with a low copper content. The integrity of the lap joint is compromised to due powder entrapment. This leads to unravelling of the sheath during deposition, which creates less desirable deposits. Uniform distribution of silicon carbide in the core was observed.

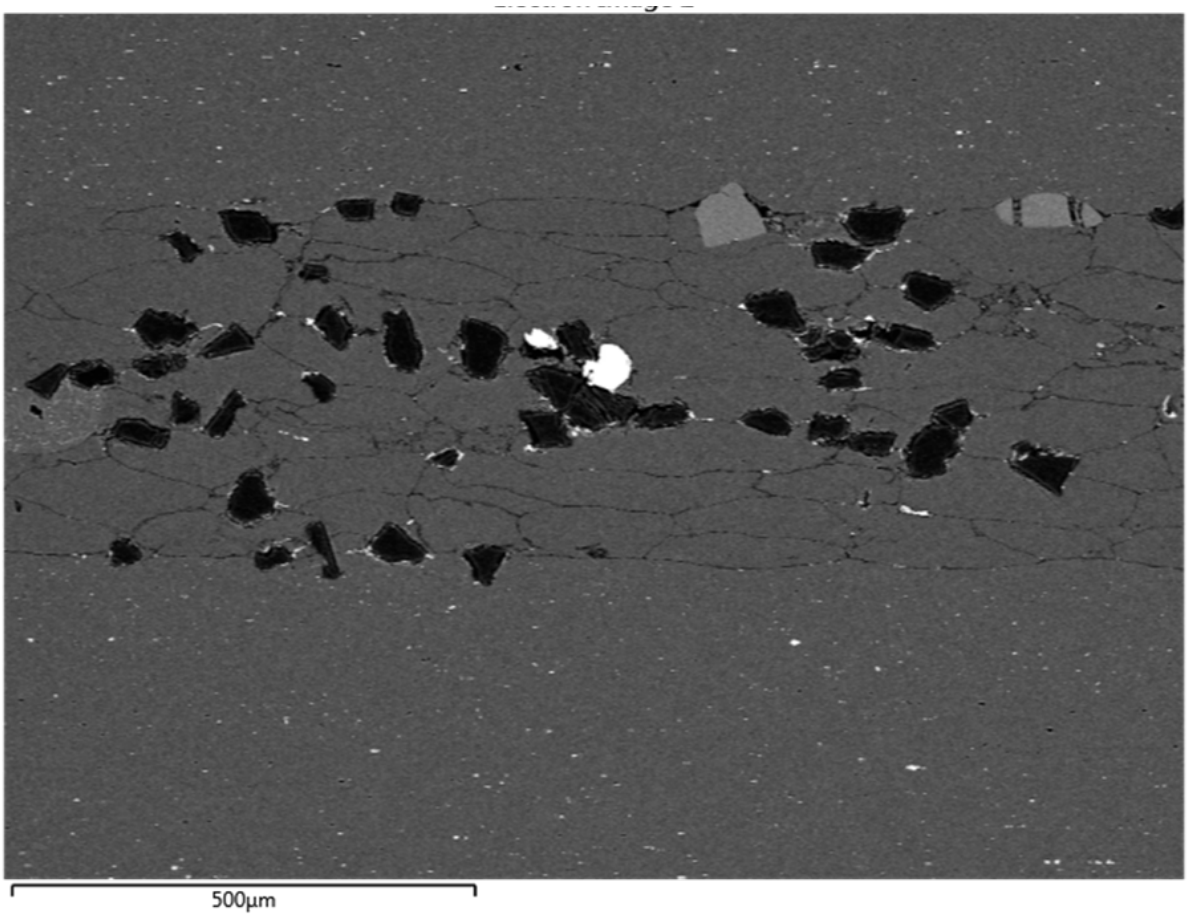

Figure A.5 A longitudinal cross sectional backscattered electron image of a wire containing silicon carbide with a copper content. There is incomplete coverage of copper coating on the silicon carbide. The particles show a much more uniform distribution high copper content particles.

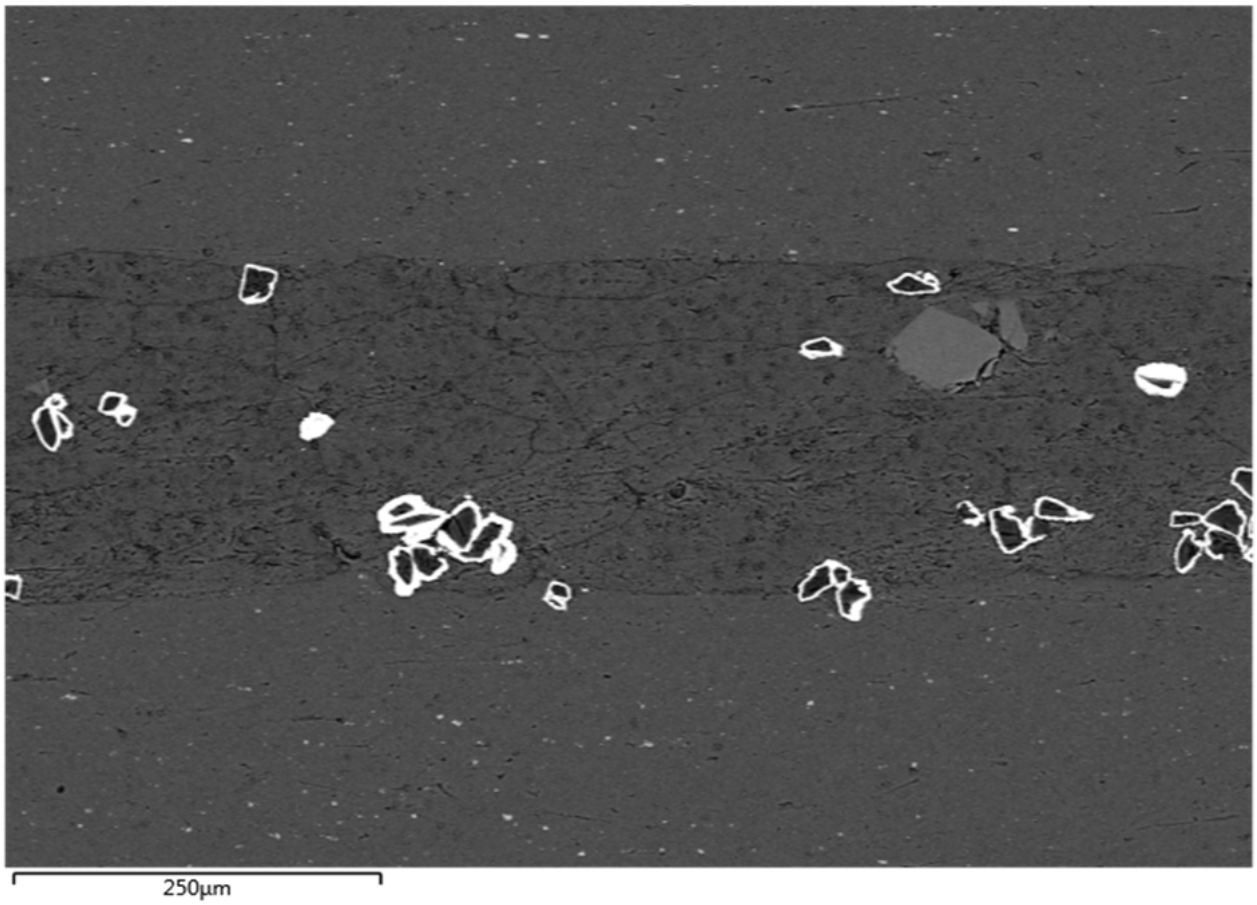

Figure A.6 A longitudinal cross sectional backscattered electron image of a wire containing silicon carbide with a high nickel content. Complete coverage of the coating was observed. Insufficient volume fraction can be observed compared to that of other wires.

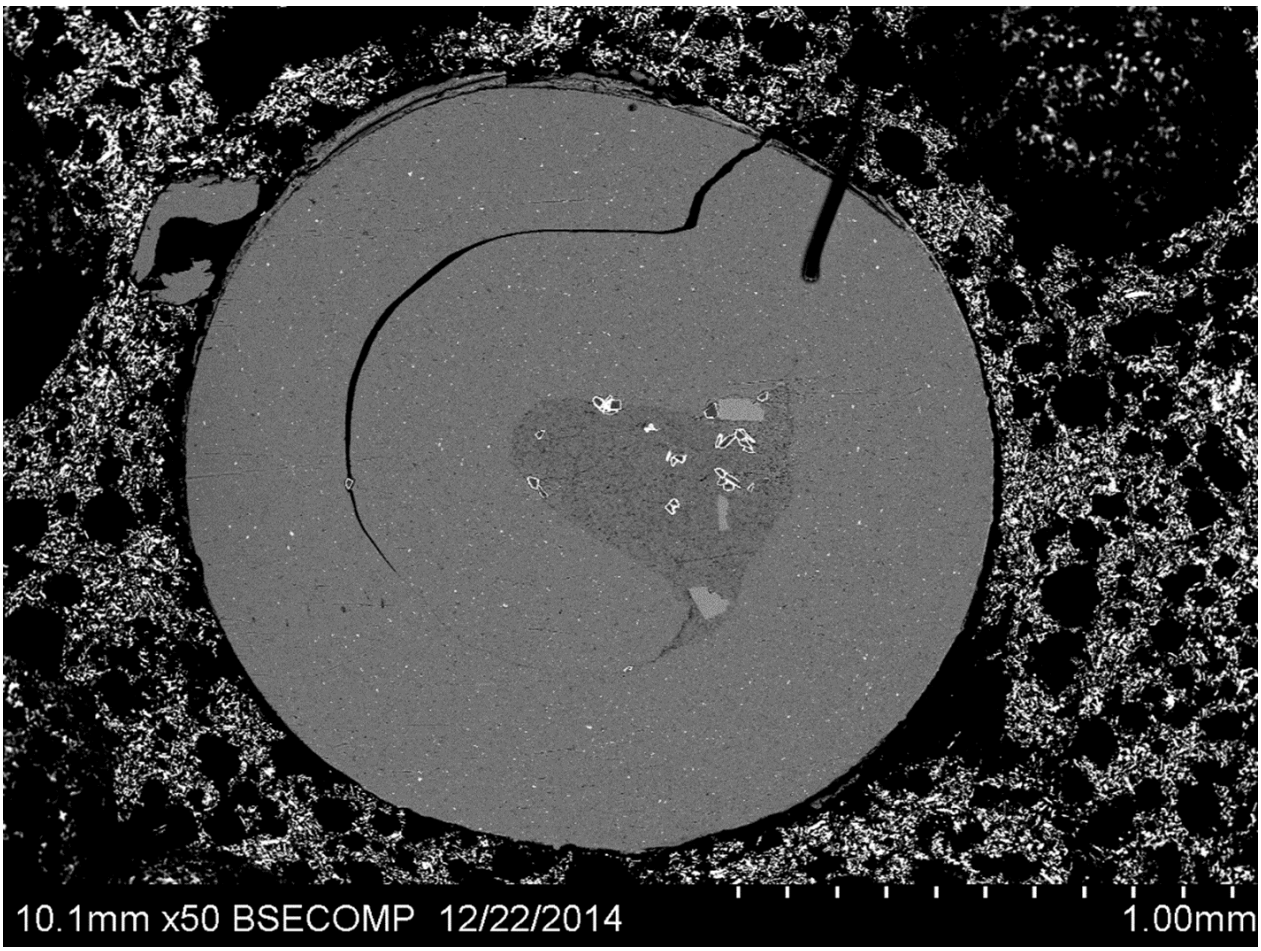

Figure A.7 Axial cross-sectional backscattered electron image of a wire containing silicon carbide with a high nickel content. The lap joint is completely sealed near the powder, protecting it from loss or contamination, however it maintains a gap which could lead to unravelling during deposition.

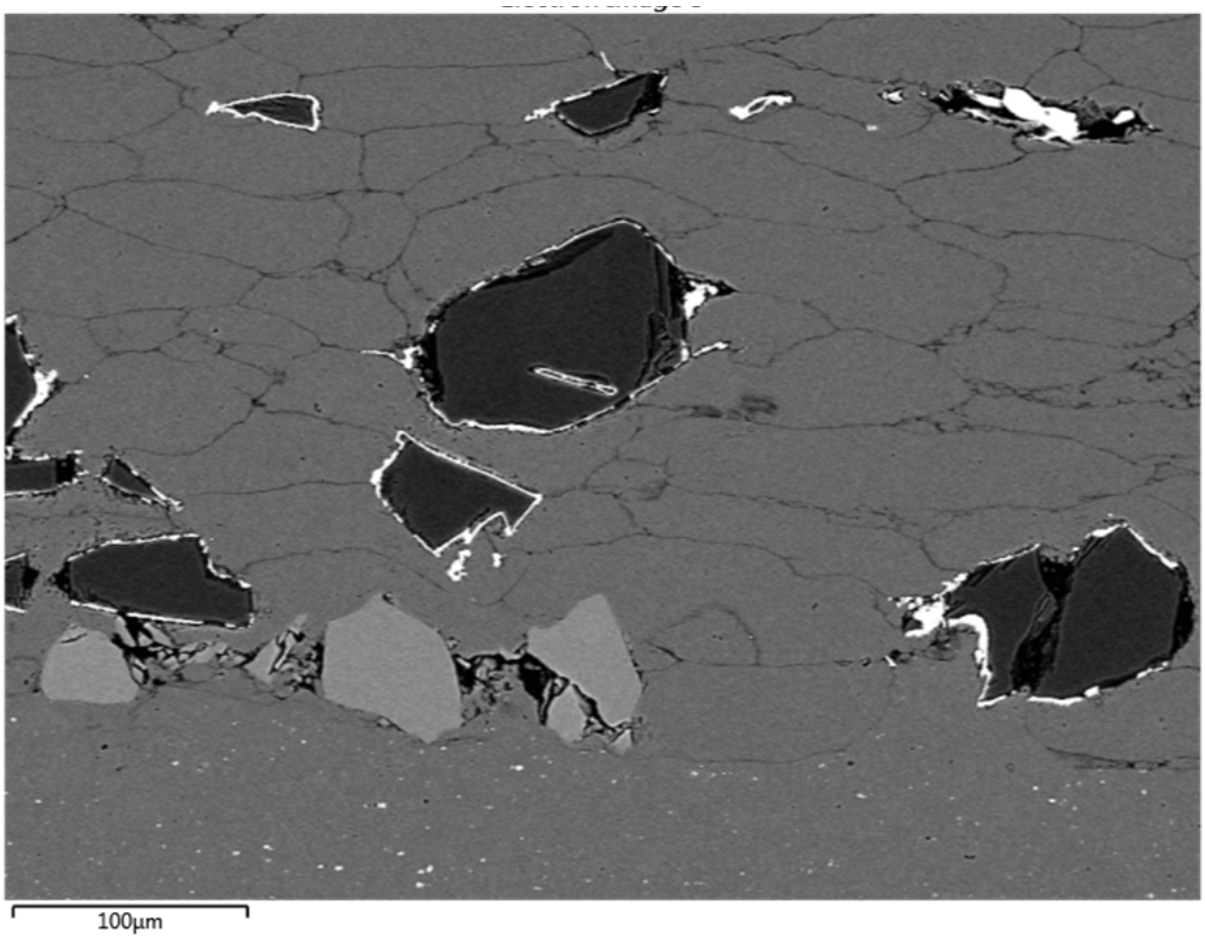

Figure A.8 A longitudinal cross sectional backscattered electron image of a wire containing silicon carbide with a low nickel content. Incomplete coverage of the coating was observed. Uniform distribution of the powder was maintained in the longitudinal direction.

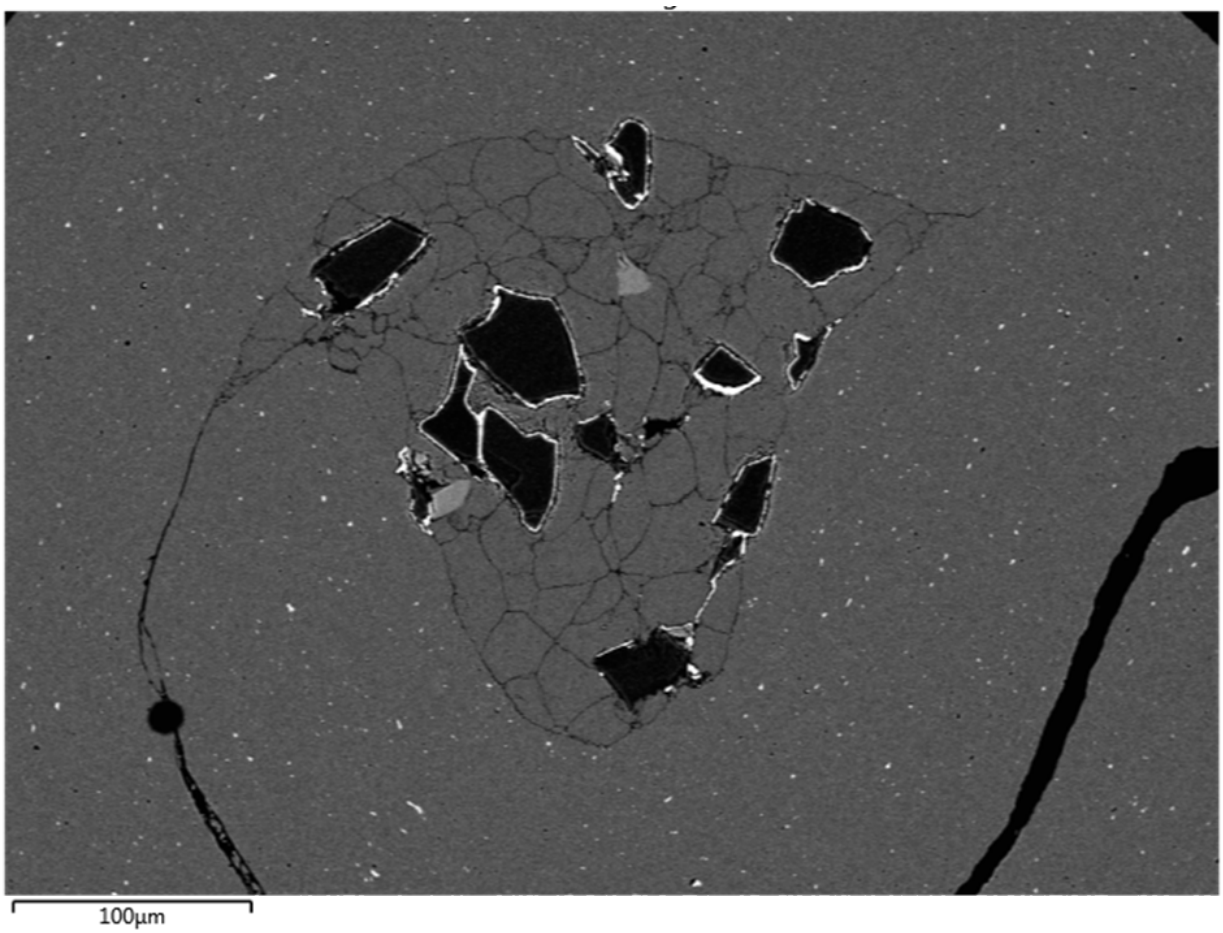

Figure A.9 Axial cross-sectional backscattered electron image of a wire containing silicon carbide with a low nickel content. The lap joint is not completely sealed which could lead to unravelling during deposition. The particles are evenly distributed in the powder core.

APPENDIX B: MULTIPLE LAYER DEPOSIT CHARACTERIZATION

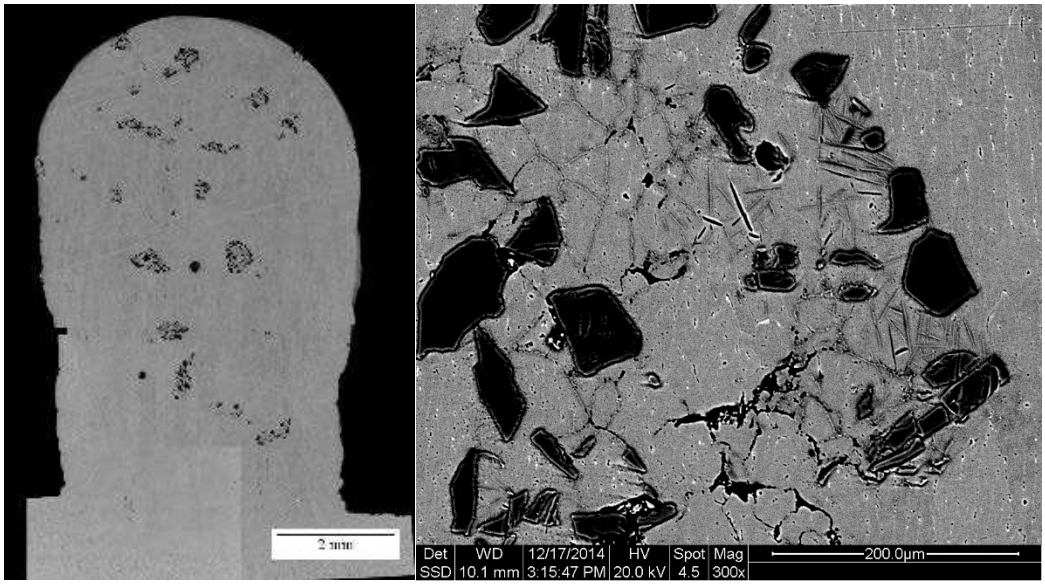

Figure B.1 A) Macroscopic cross-section of a multiple layer deposit containing uncoated silicon carbide using a focused rastered electron beam with a (0.25f) frequency pulse. B) High magnification of a silicon carbide cluster showing particle separation and aluminum carbide formation.

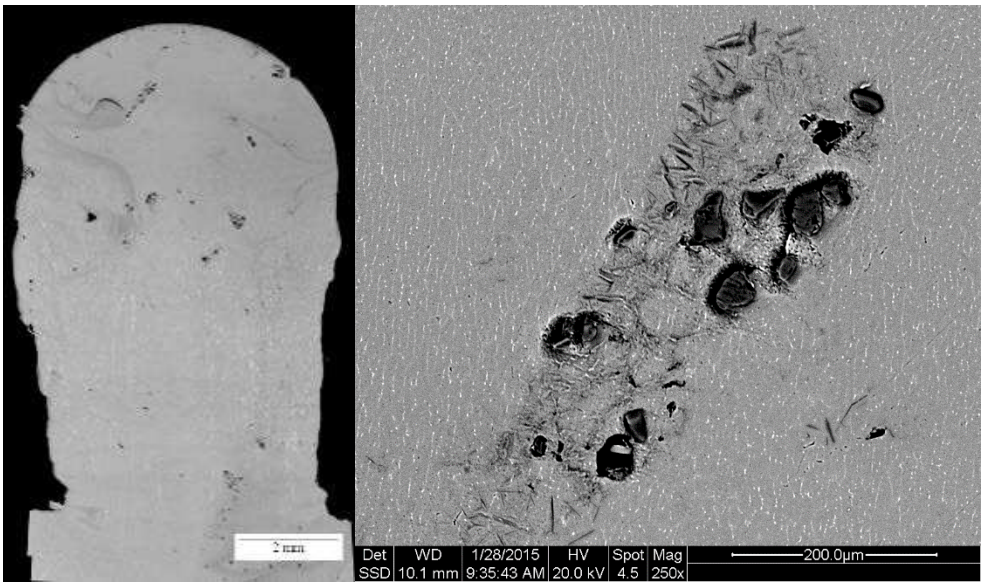

Figure B.2 A) Macroscopic image of a deposit with high copper content made using a focused rastered beam with a (0.25f) frequency pulse. B) High magnification image of a cluster in the matrix showing the high amounts of intermetallic as well as the presence of aluminum carbide.

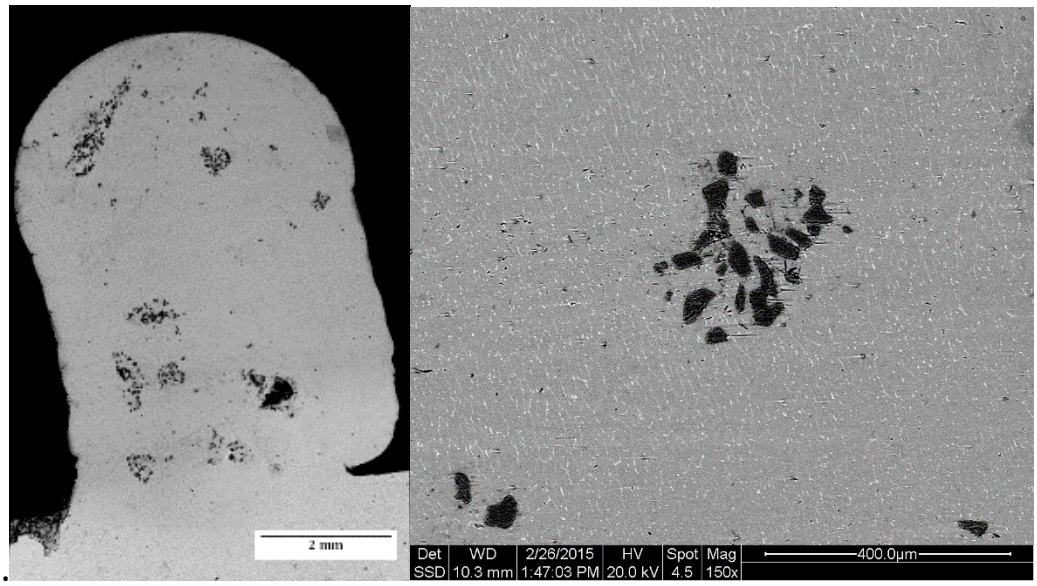

Figure B.3 A) Macroscopic image of a deposit with low copper content made using a focused rastered beam with a (0.25f) frequency pulse. B) High magnification image of clusters in the matrix showing the low amounts of intermetallic as well as the presence of aluminum carbide.

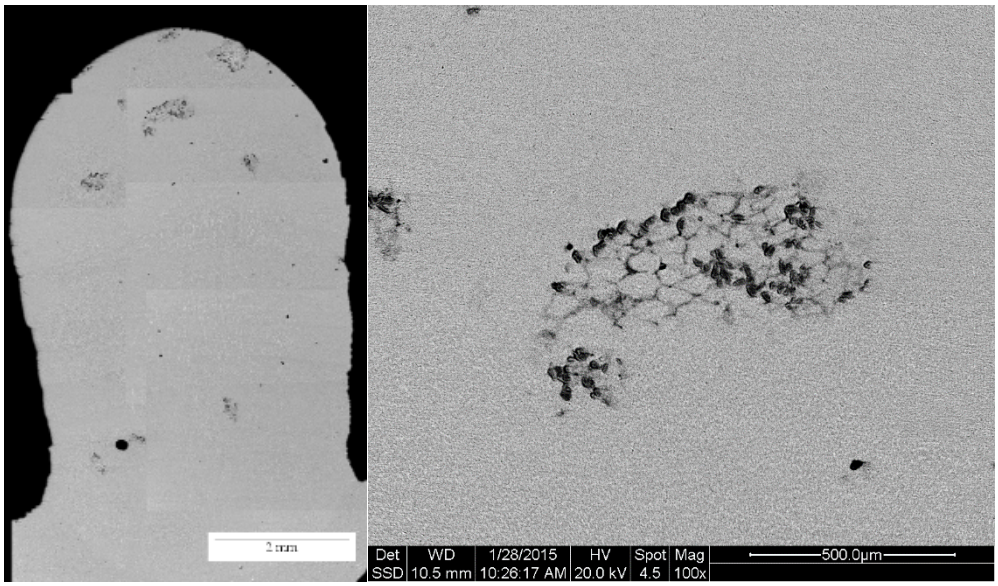

Figure B.4 A) Macroscopic image of a deposit with high nickel content made using a focused rastered beam with a (0.25f) frequency pulse. B) High magnification image of clusters in the matrix showing the high amounts of intermetallic with no presence aluminum carbide.

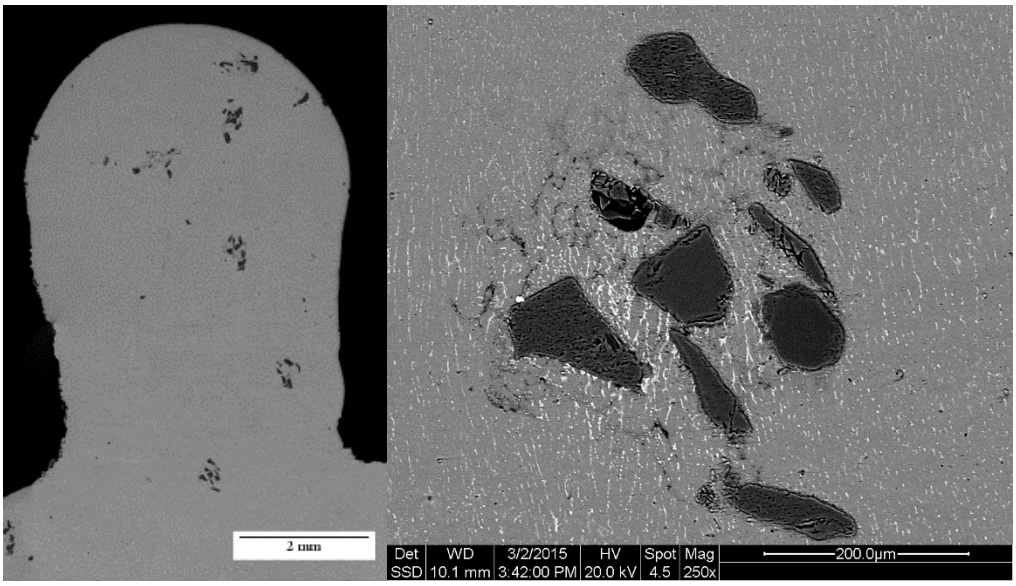

Figure B.5 A) Macroscopic image of a deposit with low nickel content made using a focused rastered beam with a (0.25f) frequency pulse. B) High magnification image of clusters in the matrix showing the low amounts of intermetallic with no presence aluminum carbide.

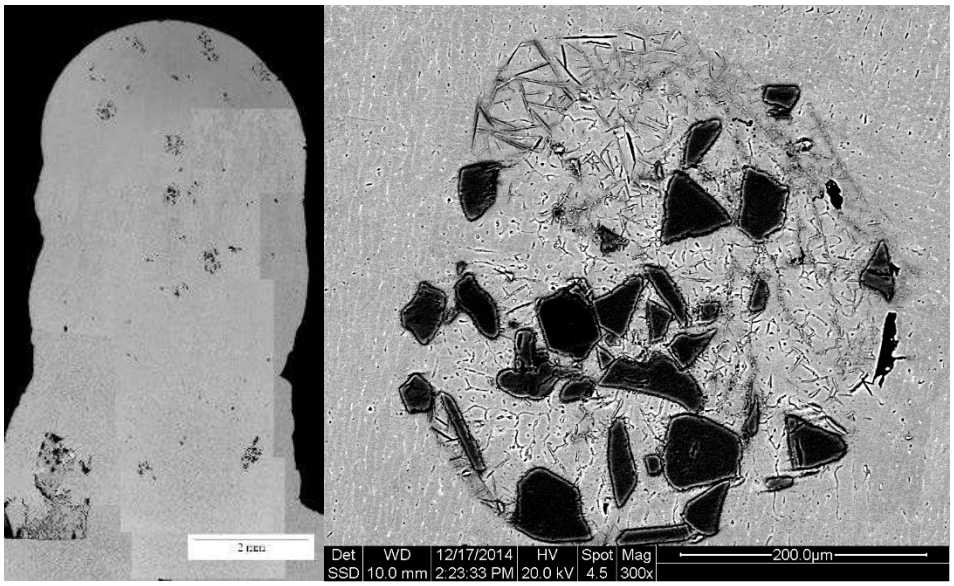

Figure B.6 A) Macroscopic cross-section of a multiple layer deposit containing uncoated silicon carbide using a focused rastered electron beam with a (f) frequency pulse. B) High magnification of a silicon carbide cluster showing particle separation and aluminum carbide formation.

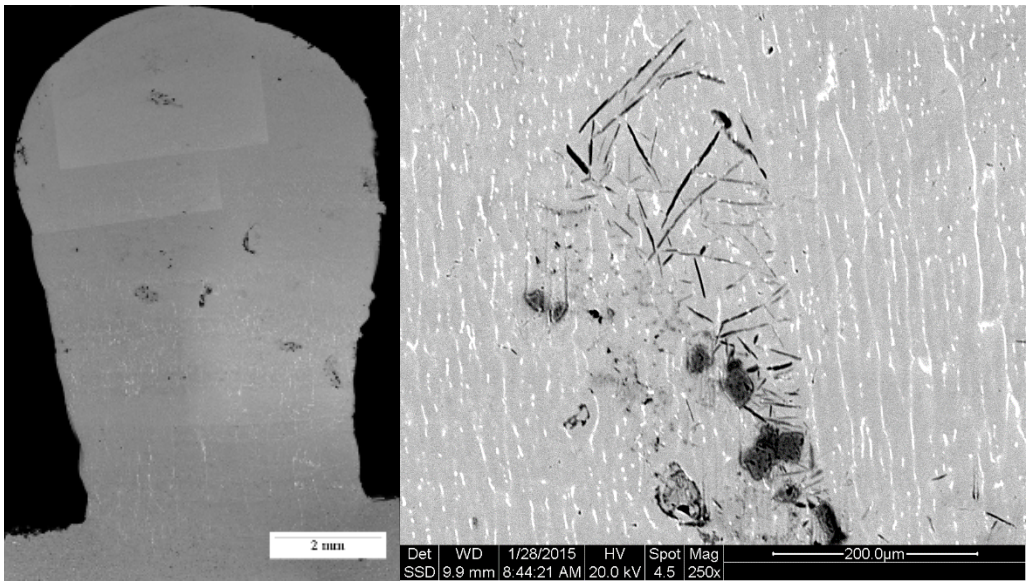

Figure B.7 A) Macroscopic image of a deposit with high copper content made using a focused rastered beam with a (f) frequency pulse. B) High magnification image of a cluster in the matrix showing the high amounts of intermetallic as well as the presence of aluminum carbide.

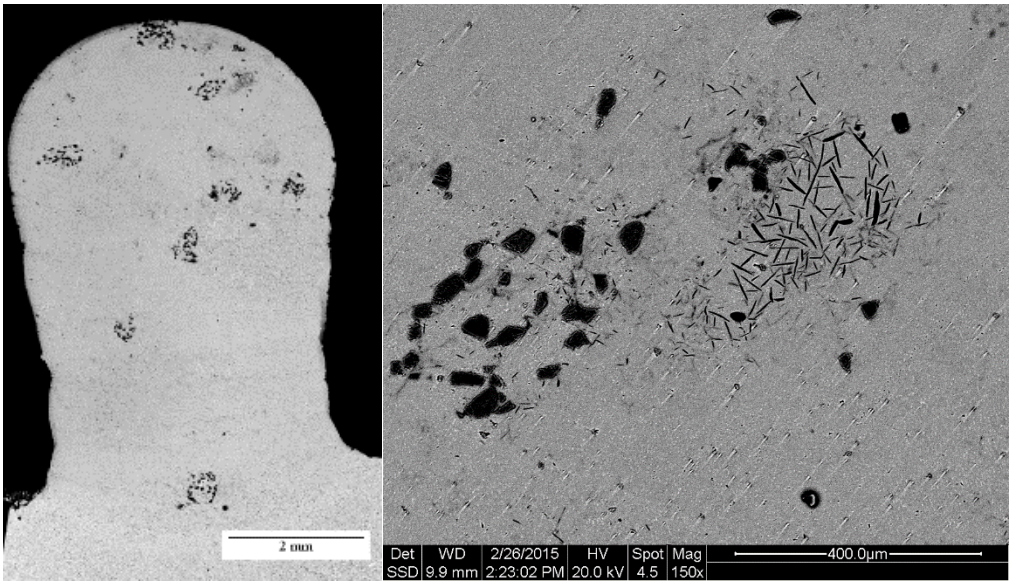

Figure B.8 A) Macroscopic image of a deposit with low copper content made using a focused rastered beam with a (f) frequency pulse. B) High magnification image of clusters in the matrix showing the low amounts of intermetallic as well as the presence of aluminum carbide.

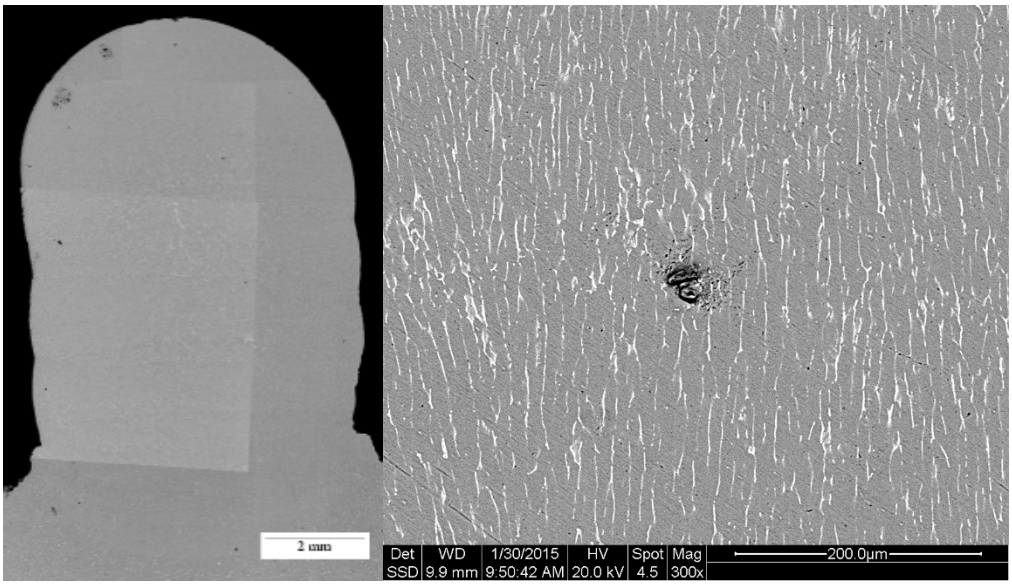

Figure B.9 A) Macroscopic image of a deposit with high nickel content made using a focused rastered beam with a (f) frequency pulse. B) High magnification image of clusters in the matrix showing the high amounts of intermetallic with no presence aluminum carbide.

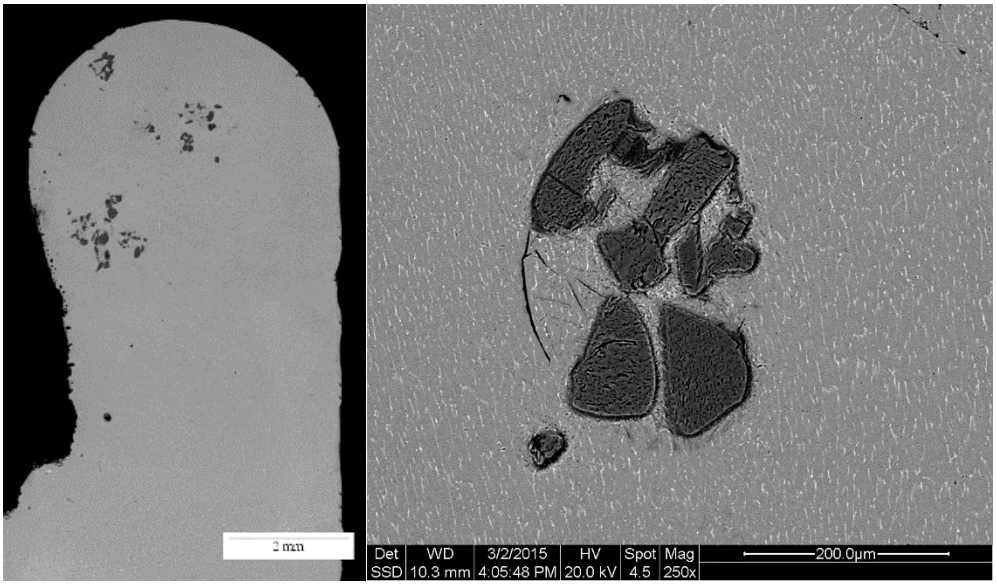

Figure B.10 A) Macroscopic image of a deposit with low nickel content made using a focused rastered beam with a (f) frequency pulse. B) High magnification image of clusters in the matrix showing the low amounts of intermetallic with no presence aluminum carbide.

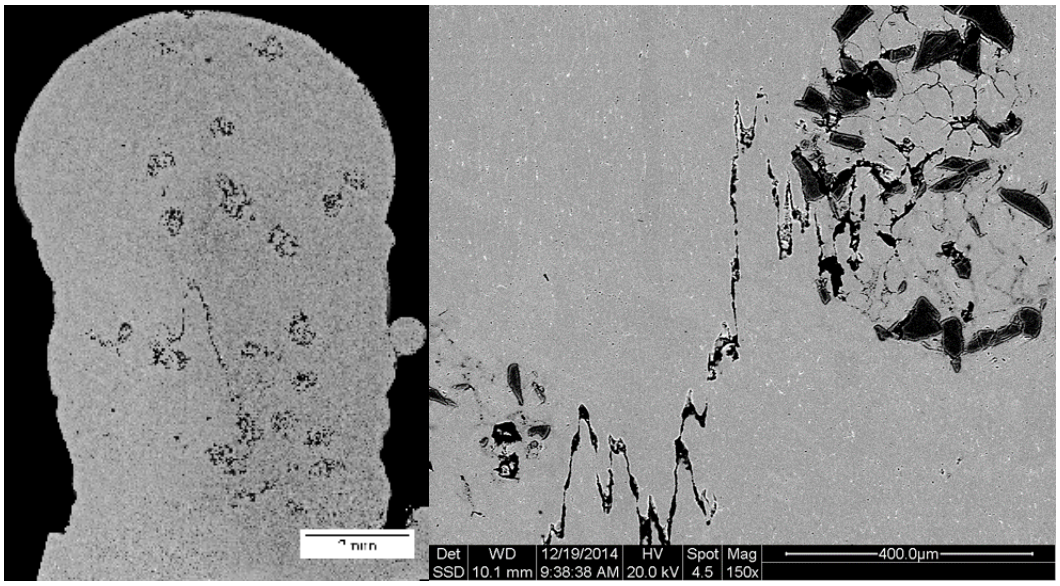

Figure B.11 A) Macroscopic cross-section of a multiple layer deposit containing uncoated silicon carbide using a defocused electron beam. B) High magnification of a silicon carbide cluster showing particle separation and aluminum carbide formation.

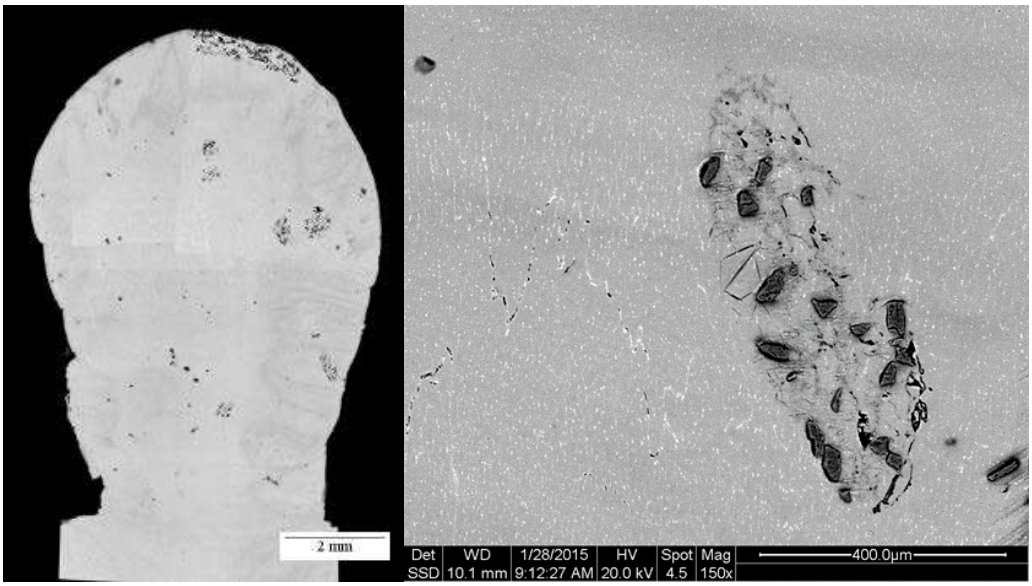

Figure B.12 A) Macroscopic image of a deposit with high copper content made using a defocused beam. B) High magnification image of a cluster in the matrix showing the high amounts of intermetallic as well as the presence of aluminum carbide.

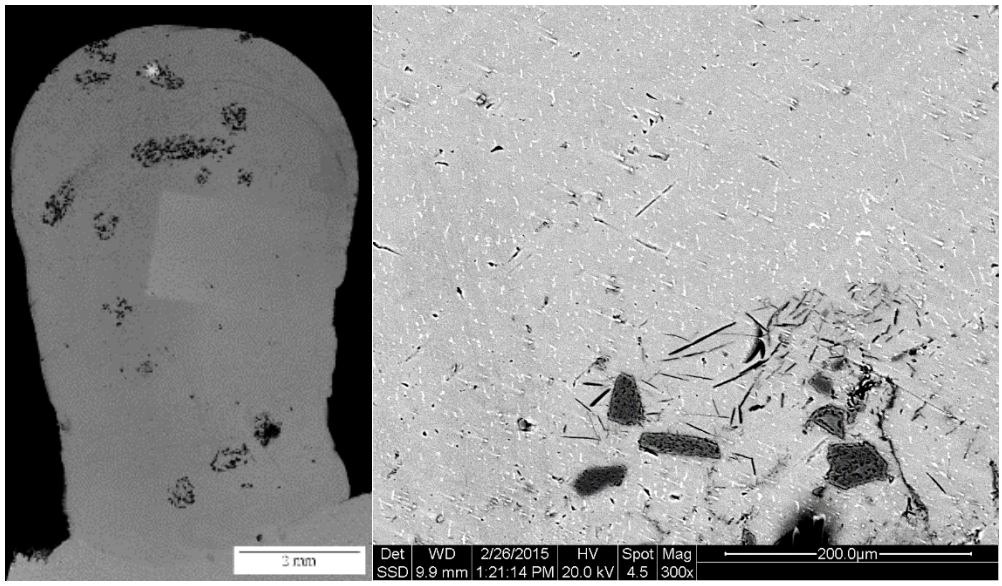

Figure B.13 A) Macroscopic image of a deposit with low copper content made using a defocused beam. B) High magnification image of clusters in the matrix showing the low amounts of intermetallic as well as the presence of aluminum carbide.

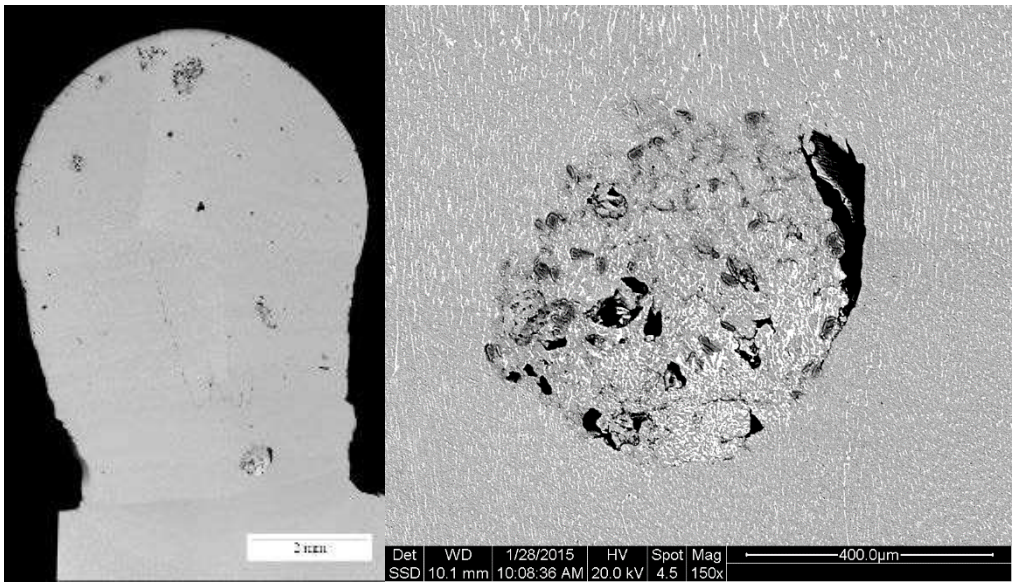

Figure B.14 A) Macroscopic image of a deposit with high nickel content made using a defocused beam. B) High magnification image of clusters in the matrix showing the high amounts of intermetallic with no presence aluminum carbide.

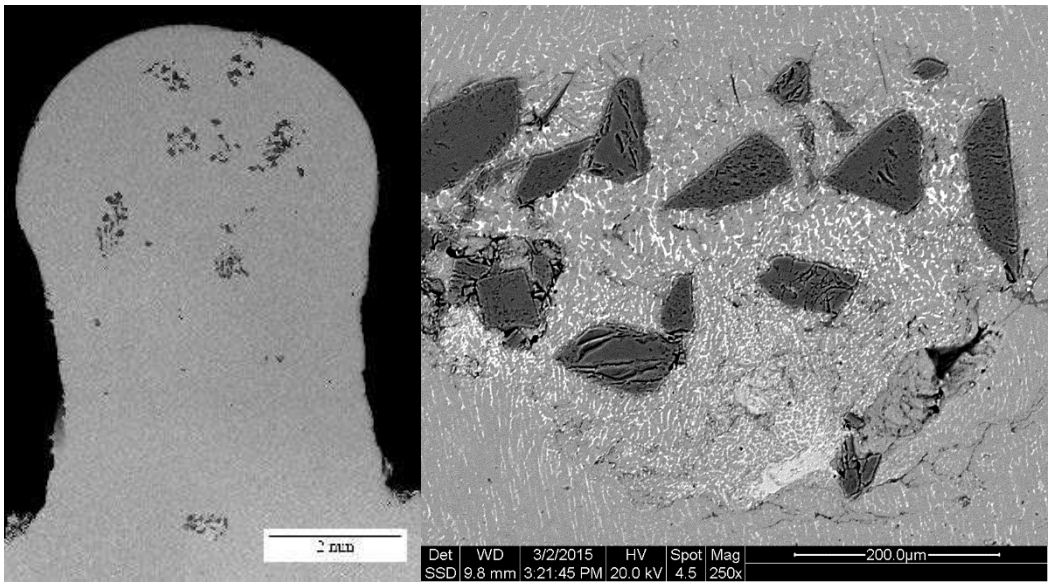

Figure B.15 A) Macroscopic image of a deposit with low nickel content made using a defocused beam. B) High magnification image of clusters in the matrix showing the low amounts of intermetallic with no presence aluminum carbide.

Table B.1: Multiple layer build comparison of different measurements taken for each coating and beam condition. Defocused pulsed beam condition trials included.

Sample	Spot	Beam Motion	Normalized Pulse (Hz)	% Particle	% Clusters Containing Al_4C_3	Cracks	Average Cluster Size (mm^2)	Average Mean Free Path (mm)
7_UC	Focused	Rastered	0	1.43	35.7	Yes	0.08	3.42
6_HCC	Focused	Rastered	0	0.42	60	Yes	0.31	2.58
6_LCC	Focused	Rastered	0	1.11	20	No	0.09	4.53
6_HNC	Focused	Rastered	0	0.87	0	No	0.08	7.42
6_LNC	Focused	Rastered	0	1.87	0	No	0.06	3.58
14_UC	Focused	Rastered	0.25f	2.35	10	Yes	0.04	4.99
4_HCC	Focused	Rastered	0.25f	0.60	30	Yes	0.12	3.48
4_LCC	Focused	Rastered	0.25f	1.85	6	No	0.07	3.35
4_HNC	Focused	Rastered	0.25f	1.03	0	No	0.07	5.06
4_LNC	Focused	Rastered	0.25f	1.09	0	No	0.11	2.14
12_UC	Focused	Rastered	f	1.36	12.5	No	0.07	3.62
8_HCC	Focused	Rastered	f	0.37	12.5	No	0.26	1.89
8_LCC	Focused	Rastered	f	1.45	26.7	No	0.06	4.34
8_HNC	Focused	Rastered	f	0.25	0	No	0.22	4.46
8_LNC	Focused	Rastered	f	1.51	11.1	No	0.07	6.10
10_UC	Defocused	None	0	2.69	12.5	Yes	0.07	2.36
2_HCC	Defocused	None	0	1.19	18.0	Yes	0.15	3.78
2_LCC	Defocused	None	0	2.35	6.7	No	0.09	3.13
2_HNC	Defocused	None	0	1.09	0	Yes	0.14	4.84
2_LNC	Defocused	None	0	1.71	12.5	No	0.07	3.56
9_HCC	Focused	Rastered	0	1.39	0.00	Yes	0.08	2.97
13_LNC	Defocused	None	0	2.25	0.25	No	0.05	3.75
12_LCC	Defocused	None	0.25f	2.15	0.27	No	0.07	4.48
10_HNC	Defocused	None	0.25f	1.01	0.00	No	0.07	5.69
10_LNC	Defocused	None	0.25f	1.18	0.29	Yes	0.13	4.50
10_LCC	Defocused	None	f	1.80	0.5	No	0.07	3.96
12_HNC	Defocused	None	f	0.86	0.00	No	0.15	3.78
12_LNC	Defocused	None	f	0.99	0.29	No	0.08	5.89

APPENDIX C: SINGLE LAYER DEPOSIT CHARACTERIZATION

Table C.1: Single layer build comparison of different measurements taken for each coating and beam condition. Defocused pulsed beam condition trials included.

Sample	Spot	Beam Motion	Pulse (Hz)	% Particle	% Clusters Containing Al_4C_3	Cracks	Width (mm)	Overfill Height (mm)	Depth of Penetration (mm)	Aspect Ratio
5_HCC	Focused	Rastered	0	0.00	0	Yes	4.91	1.26	1.18	2.01
5_LCC	Focused	Rastered	0	0.21	0	Yes	5.02	1.40	0.82	2.26
5_HNC	Focused	Rastered	0	0.00	0	Yes	5.47	1.24	1.56	1.95
5_LNC	Focused	Rastered	0	0.16	0	No	5.37	1.36	1.23	2.07
13_UC	Focused	Rastered	0.25f	0.35	0	Yes	4.86	1.35	1.13	1.96
3_HCC	Focused	Rastered	0.25f	0.16	0	Yes	4.58	0.98	1.00	2.31
3_LCC	Focused	Rastered	0.25f	0.82	50	No	4.82	1.41	0.77	2.21
3_HNC	Focused	Rastered	0.25f	0.00	0	Yes	5.10	1.16	1.15	2.21
3_LNC	Focused	Rastered	0.25f	0.18	100	Yes	5.06	1.17	1.09	2.24
11_UC	Focused	Rastered	f	0.83	50	Yes	5.03	1.01	0.94	2.58
7_HCC	Focused	Rastered	f	0.24	0	Yes	5.23	1.25	1.20	2.13
7_LCC	Focused	Rastered	f	0.22	100	Yes	5.13	1.29	0.87	2.38
7_HNC	Focused	Rastered	f	0.11	0	Yes	5.02	1.32	1.17	2.10
7_LNC	Focused	Rastered	f	0.17	0	Yes	5.40	1.34	0.90	2.41
1_HCC	Defocused	None	0	0.06	0	Yes	4.64	1.49	0.80	2.03
1_LCC	Defocused	None	0	0.78	0	Yes	3.71	1.43	0.69	1.75
1_HNC	Defocused	None	0	0.00	0	Yes	4.88	1.24	1.08	2.10
1_LNC	Defocused	None	0	0.86	100	Yes	4.70	1.49	1.01	1.88
9_LCC	Defocused	None	f	0.31	100	Yes	5.30	0.58	0.96	3.44
11_LCC	Defocused	None	0.25f	0.26	0	No	5.16	1.18	0.87	2.52
9_HNC	Defocused	None	0.25f	0.13	0	Yes	5.58	1.22	1.15	2.35
11_HNC	Defocused	None	f	0.00	0	Yes	5.67	1.15	1.12	2.50
9_LNC	Defocused	None	0.25f	0.25	100	No	5.69	1.65	1.17	2.02
11_LNC	Defocused	None	f	0.25	0	No	5.34	1.22	1.16	2.24

APPENDIX D: THERMOCALC MODELS

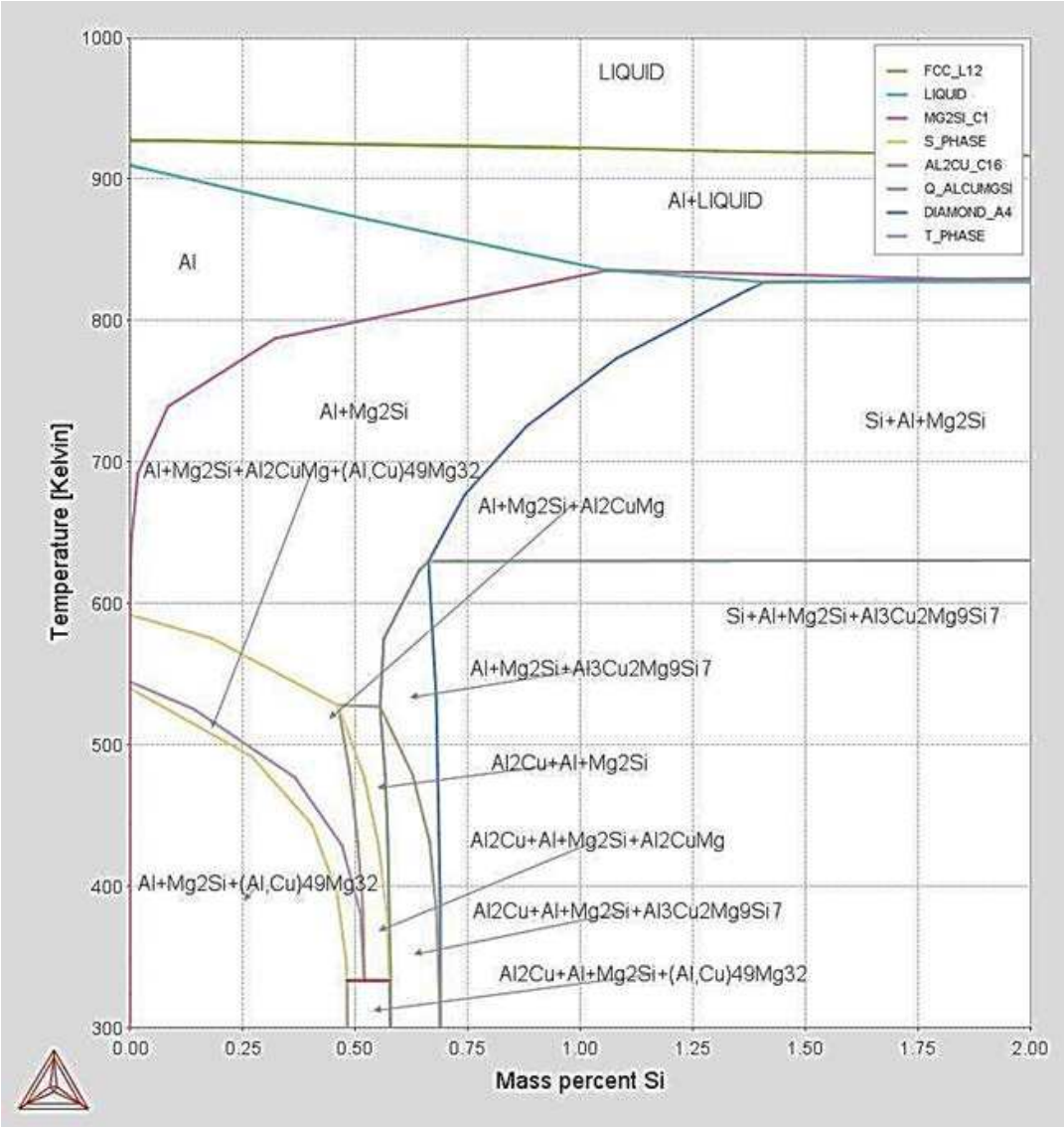

Figure D.1: Pseudo-binary phase diagram of the Al 6061 alloy. Composition set at Al – 1.0 wt. pct. Mg – 0.25 pct. wt. Cu with varying amounts of silicon.

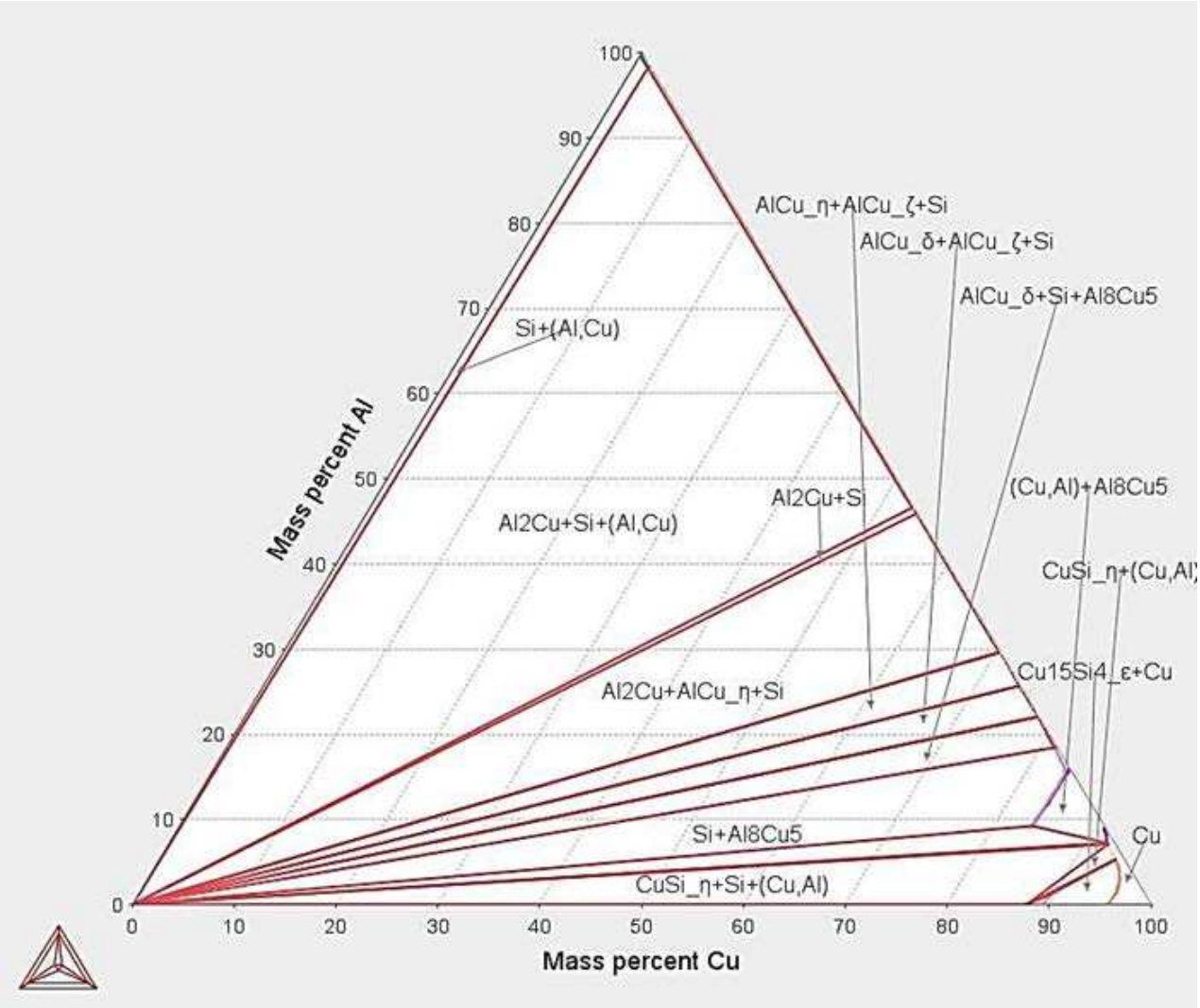

Figure D.2 Al-Cu-Si isothermal ternary phase diagram at 675 K.

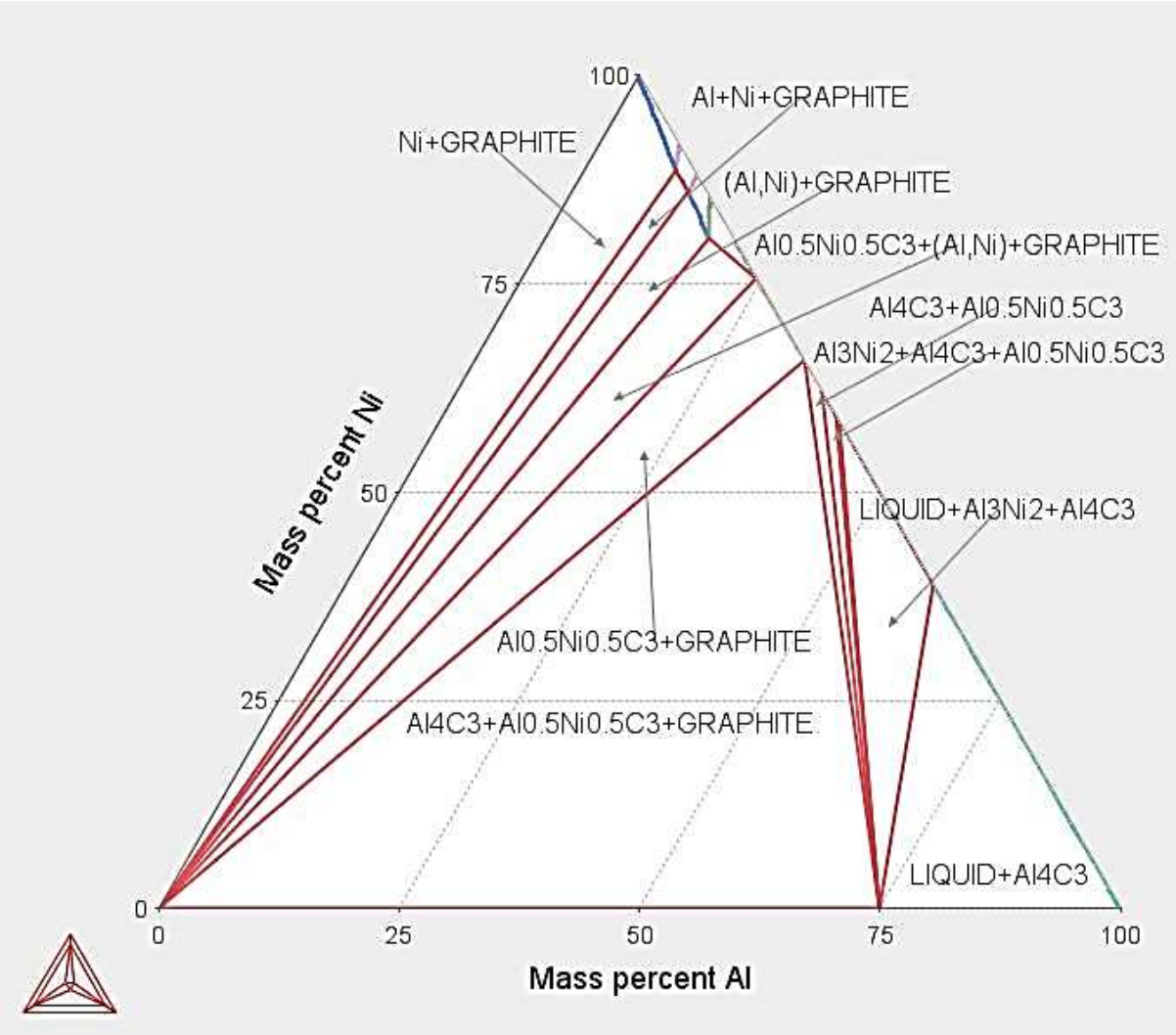

Figure D.3 Al-Ni-C isothermal ternary phase diagram at 1350 K.

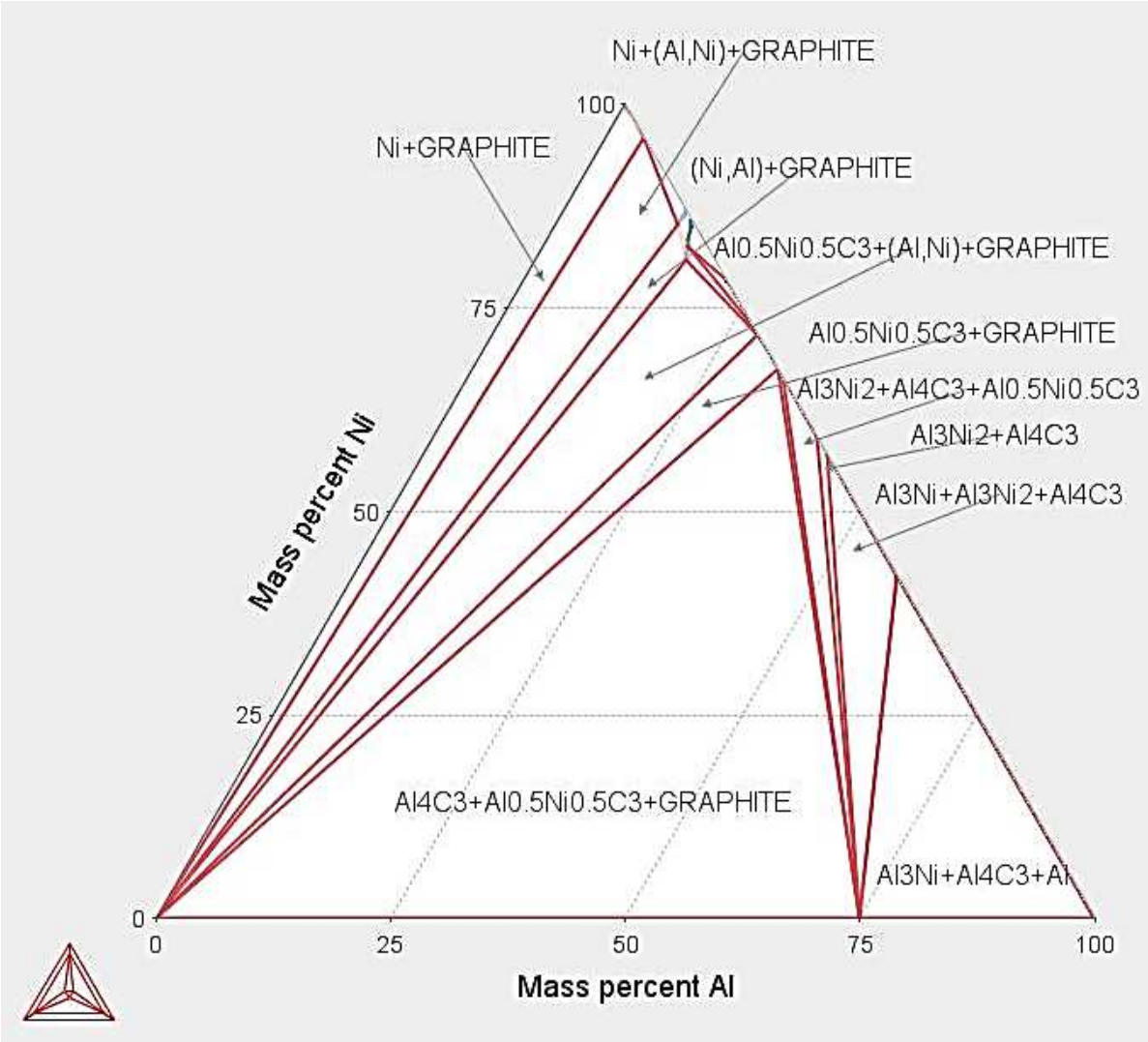

Figure D.4 Al-Ni-C isothermal ternary phase diagram at 675 K.

APPENDIX E: HSC EQUILIBRIUM REACTION TABLES

Table E.1: Equilibrium reaction data for the Al-Mg-SiC system predicting the favorability of maintaining silicon carbide stability in the presence of magnesium.

2Mg + Al + 4SiC = Al + Mg2Si + 3SiC + C					
T (K)	ΔH (kJ)	ΔS (J/K)	ΔG (kJ)	K	Log(K)
298	-7.385	-0.042	-7.372	1.96E+01	1.292
398	-7.459	-0.251	-7.359	9.25E+00	0.966
498	-7.562	-0.482	-7.322	5.86E+00	0.768
598	-7.653	-0.648	-7.265	4.31E+00	0.635
698	-7.767	-0.823	-7.192	3.45E+00	0.538
798	-7.958	-1.077	-7.098	2.92E+00	0.465
898	-8.28	-1.456	-6.973	2.55E+00	0.406
998	-25.928	-20.554	-5.415	1.92E+00	0.283
1098	-26.594	-21.19	-3.327	1.44E+00	0.158
1198	-27.144	-21.671	-1.182	1.13E+00	0.052
1298	-27.565	-22.009	1.003	9.11E-01	-0.04
1398	57.939	40.262	1.652	8.68E-01	-0.062
1498	57.76	40.139	-2.368	1.21E+00	0.083
1598	57.574	40.019	-6.376	1.62E+00	0.208
1698	57.386	39.904	-10.372	2.09E+00	0.319
1798	57.194	39.795	-14.357	2.61E+00	0.417
1898	57	39.69	-18.331	3.20E+00	0.505
1998	56.802	39.588	-22.295	3.83E+00	0.583
2098	56.598	39.488	-26.249	4.50E+00	0.654
2198	56.387	39.39	-30.193	5.22E+00	0.718
2298	56.167	39.292	-34.127	5.97E+00	0.776
2398	55.935	39.193	-38.051	6.74E+00	0.829
2498	55.688	39.092	-41.965	7.54E+00	0.878
2598	55.422	38.988	-45.869	8.36E+00	0.922
2698	55.136	38.88	-49.763	9.19E+00	0.964
Mg2Si		*Extrapolated from*		*2000 K*	
Formula	FM (g/mol)	Conc. (wt-%)	Amount (mol)	Amount (g)	Volume (ml)
Reactants					
Mg	24.305	20.599	2	48.61	27.937
Al	26.982	11.434	1	26.982	9.993
SiC	40.097	67.967	4	160.386	50.755
Products					
Al	26.982	11.434	1	26.982	9.993
Mg2Si	76.696	32.501	1	76.696	38.54
SiC	40.097	50.975	3	120.29	38.066
C	12.011	5.09	1	12.011	4.584

Table E.2: Equilibrium reaction data for the Al-Mg-SiC system predicting the favorability of stabilizing aluminum carbide formation in the presence of magnesium. It is more favorable than maintaining silicon carbide.

6Mg + 4Al + 3SiC = Al4C3 + 3Mg2Si					
T (K)	ΔH (kJ)	ΔS (J/K)	ΔG (kJ)	K	Log(K)
298	-229.053	-41.497	-216.687	9.66E+37	37.985
398	-229.508	-42.828	-212.462	7.70E+27	27.886
498	-229.85	-43.594	-208.14	6.81E+21	21.833
598	-230.348	-44.498	-203.738	6.28E+17	17.798
698	-231.281	-45.929	-199.223	8.13E+14	14.91
798	-232.932	-48.127	-194.527	5.42E+12	12.734
898	-235.588	-51.249	-189.566	1.07E+11	11.028
998	-333.054	-156.231	-177.135	1.87E+09	9.272
1098	-336.287	-159.323	-161.351	4.75E+07	7.677
1198	-338.959	-161.655	-145.296	2.17E+06	6.336
1298	-341.006	-163.3	-129.043	1.56E+05	5.193
1398	-85.03	23.116	-117.345	2.43E+04	4.385
1498	-85.846	22.551	-119.627	1.49E+04	4.172
1598	-86.415	22.183	-121.862	9.63E+03	3.984
1698	-86.723	21.994	-124.07	6.56E+03	3.817
1798	-86.764	21.97	-126.267	4.66E+03	3.669
1898	-86.533	22.095	-128.469	3.44E+03	3.536
1998	-86.029	22.353	-130.69	2.61E+03	3.417
2098	-85.254	22.731	-132.943	2.04E+03	3.31
2198	-84.212	23.216	-135.24	1.64E+03	3.214
2298	-82.908	23.795	-137.59	1.34E+03	3.128
2398	-81.348	24.459	-140.002	1.12E+03	3.05
2498	-79.539	25.198	-142.484	9.54E+02	2.98
2598	-77.49	26.002	-145.043	8.25E+02	2.916
2698	-75.207	26.864	-147.686	7.24E+02	2.86
	Al4C3	*Extrapolated from*		*2500 K*	
	Mg2Si	*Extrapolated from*		*2000 K*	
Formula	FM (g/mol)	Conc. (wt-%)	Amount (mol)	Amount (g)	Volume (ml)
Reactants					
Mg	24.305	38.987	6	145.83	83.81
Al	26.982	28.854	4	107.926	39.973
SiC	40.097	32.159	3	120.29	38.066
Products					
Al4C3	143.959	38.487	1	143.959	61
Mg2Si	76.696	61.513	3	230.087	115.621

Table E.3: Equilibrium reaction data for the Al-Mg-Cu-SiC system predicting the favorability of maintaining silicon carbide stability.

Cu + 5Al + 4SiC + 4Mg +Si = Mg2Si + 4SiC + 5Al +Mg2Cu					
T (K)	**ΔH (kJ)**	**ΔS (J/K)**	**ΔG (kJ)**	**K**	**Log(K)**
298	-108.787	-14.035	-104.605	2.17E+18	18.337
398	-109.378	-15.746	-103.111	3.42E+13	13.534
498	-109.912	-16.946	-101.473	4.41E+10	10.644
598	-110.389	-17.82	-99.733	5.16E+08	8.712
698	-110.865	-18.555	-97.914	2.13E+07	7.328
798	-111.416	-19.291	-96.022	1.93E+06	6.286
898	-75.56	23.425	-96.596	4.16E+05	5.619
998	-110.1	-13.97	-96.157	1.08E+05	5.033
1098	-110.898	-14.733	-94.721	3.21E+04	4.507
1198	-111.673	-15.408	-93.214	1.16E+04	4.065
1298	-112.45	-16.031	-91.641	4.88E+03	3.688
1398	-40.662	36.136	-91.18	2.55E+03	3.407
1498	-41.267	35.718	-94.773	2.02E+03	3.305
1598	-41.913	35.301	-98.324	1.64E+03	3.214
1698	-92.781	5.102	-101.443	1.32E+03	3.121
1798	-93.281	4.815	-101.939	9.16E+02	2.962
1898	-93.782	4.544	-102.407	6.59E+02	2.819
1998	-94.282	4.287	-102.848	4.89E+02	2.689
2098	-94.783	4.043	-103.265	3.73E+02	2.571
2198	-95.283	3.81	-103.657	2.91E+02	2.464
2298	-95.784	3.587	-104.027	2.32E+02	2.365
2398	-96.285	3.374	-104.375	1.88E+02	2.274
2498	-96.785	3.169	-104.702	1.55E+02	2.19
2598	-97.286	2.973	-105.009	1.29E+02	2.111
2698	-97.786	2.784	-105.297	1.09E+02	2.039
Mg2Si		***Extrapolated from***	***2000 K***		
Mg2Cu		***Extrapolated from***	***840 K***		
Formula	**FM (g/mol)**	**Conc. (wt-%)**	**Amount (mol)**	**Amount (g)**	**Volume (ml)**
Reactants					
Cu	63.546	13.125	1	63.546	7.092
Al	26.982	27.865	5	134.908	49.966
SiC	40.097	33.128	4	160.386	50.755
Mg	24.305	20.081	4	97.22	55.874
Si	28.086	5.801	1	28.086	12.059
Products					
Mg2Si	76.696	15.841	1	76.696	38.54
SiC	40.097	33.128	4	160.386	50.755
Al	26.982	27.865	5	134.908	49.966
Mg2Cu	112.156	23.166	1	112.156	0

APPENDIX F: FLUID MECHANICS CALCULATIONS

Boundary conditions for calculating steady state velocity with respect to viscosity are as follows:

- ρ_1 = 2385 kg/m^3
- ρ_p = 1250 kg/m^3
- *r_p = 22.75 x 10^{-6} m

*r_p is the average particle radius based on measurements from static laser light scattering analysis of the particles. Temperature values were measured using the infrared pyrometer and given in Table A6.1. Those measurements were used to determine viscosity and steady state velocity for various compositions at temperatures equivalent the melt pool shown in Table A6.2.Values in red are data points calculated below the melting temperature

Table F.1 Temperatures of the melt pool measured by the infrared pyrometer.

Time (s)	Temperature (°C)
0.30	1305.2
0.80	1455.3
1.30	1506.5
1.80	1368.5
2.30	1503.2
2.80	1693.5 *max
3.30	1417.2
3.80	1607.6
4.30	1379.1
4.80	1380.7
5.20	1489.9
5.80	1387.3
6.30	1471
6.70	1375.5
7.20	1307.5
7.70	1153.4
8.20	1050.3
8.70	967.4
9.20	895.5
9.70	831.8
10.20	772.8
10.80	749.9 *min

Table F.2: Viscosity and steady state velocity data for various compositions and temperatures seen in the melt pool.

Al viscosity (cP)	Al vss x 10-3 (m/s)	Ni viscosity (cP)	Ni vss x 10-3 (m/s)	NiAl3 viscosity (cP)	NiAl3 vss x 10-3 (m/s)	NiAl viscosity (cP)	NiAl vss x 10-3 (m/s)	Ni3Al viscosity (cP)	Ni3Al vss x 10-3 (m/s)	Cu viscosity (cP)	Cu vss x 10-3 (m/s)	Al2Cu viscosity (cP)	Al2Cu vss x 10-3 (m/s)	Al0.1Cu0.9 viscosity (cP)	Al0.1Cu0.9 vss x 10-3 (m/s)
0.52	1.75	7.63	0.84	2.30	0.37	4.08	0.73	5.85	0.64	3.07	2.10	1.37	0.12	2.82	1.75
0.47	1.96	5.47	1.18	1.72	0.50	2.97	1.01	4.22	0.88	2.51	2.57	1.14	0.14	2.31	2.14
0.46	2.02	4.95	1.30	1.58	0.54	2.70	1.11	3.82	0.97	2.36	2.74	1.09	0.15	2.17	2.27
0.50	1.84	6.58	0.98	2.02	0.42	3.54	0.84	5.06	0.74	2.81	2.30	1.26	0.13	2.58	1.92
0.46	2.02	4.98	1.29	1.59	0.54	2.72	1.10	3.85	0.97	2.37	2.73	1.09	0.15	2.18	2.27
0.41	2.25	3.58	1.79	1.20	0.71	2.00	1.50	2.79	1.33	1.94	3.33	0.92	0.17	1.79	2.76
0.48	1.91	5.92	1.09	1.84	0.47	3.20	0.93	4.56	0.82	2.64	2.45	1.19	0.13	2.42	2.04
0.43	2.15	4.12	1.56	1.35	0.63	2.28	1.31	3.20	1.16	2.12	3.06	0.99	0.16	1.95	2.54
0.50	1.85	6.43	1.00	1.98	0.43	3.46	0.86	4.94	0.75	2.77	2.33	1.25	0.13	2.54	1.94
0.50	1.86	6.40	1.00	1.97	0.43	3.45	0.87	4.93	0.76	2.77	2.34	1.24	0.13	2.54	1.95
0.46	2.00	5.11	1.26	1.62	0.53	2.78	1.07	3.95	0.94	2.41	2.68	1.10	0.14	2.22	2.23
0.49	1.87	6.31	1.02	1.95	0.44	3.40	0.88	4.86	0.77	2.74	2.36	1.23	0.13	2.52	1.96
0.47	1.98	5.30	1.21	1.67	0.51	2.88	1.04	4.09	0.91	2.47	2.62	1.13	0.14	2.27	2.18
0.50	1.85	6.48	0.99	1.99	0.43	3.49	0.86	4.98	0.75	2.78	2.32	1.25	0.13	2.56	1.93
0.52	1.76	7.58	0.85	2.29	0.37	4.05	0.74	5.82	0.64	3.06	2.11	1.36	0.12	2.81	1.76
0.60	1.53	11.46	0.56	3.31	0.26	6.03	0.50	8.74	0.43	3.94	1.64	1.70	0.09	3.60	1.37
0.67	1.38	15.93	0.40	4.48	0.19	8.30	0.36	12.12	0.31	4.81	1.34	2.04	0.08	4.40	1.12
0.74	1.24	21.61	0.30	5.96	0.14	11.18	0.27	16.39	0.23	5.79	1.12	2.41	0.07	5.29	0.94
0.81	1.13	29.03	0.22	7.87	0.11	14.92	0.20	21.97	0.17	6.93	0.93	2.83	0.06	6.32	0.78
0.90	1.02	39.27	0.16	10.49	0.08	20.09	0.15	29.68	0.13	8.32	0.78	3.35	0.05	7.58	0.65
0.99	0.92	53.45	0.12	14.11	0.06	27.22	0.11	40.34	0.09	10.04	0.64	3.98	0.04	9.13	0.54
1.04	0.89	60.82	0.11	15.98	0.05	30.93	0.10	45.88	0.08	10.86	0.60	4.28	0.04	9.88	0.50
1.25	0.73	107.40	0.06	27.79	0.03	54.33	0.06	80.87	0.05	15.34	0.42	5.90	0.03	13.93	0.35